Università degli Studi di Cagliari

PHD DEGREE

in Physics

Cycle XXXI

TITLE OF THE PHD THESIS

Preparation and characterization of layered two-dimensional germanium halide perovskite

FIS/01

PhD Student:	Xueqing Chang
Coordinator of the PhD Programme	Prof. Paolo Ruggerone
Supervisors	Prof. Michele Saba,

Final exam. Academic Year 2017 – 2018

Thesis defense: January 2019 Session

Contents

Chapter 1 Introduction 4

1.1 Development process of organometal perovskite solar cells 5

1.2 Basic structure, constitution and properties of organometal perovskites 8

1.3 Organometal halide perovskite solar cells 11

1.3.1 Dye-sensitized solar cells (DSSCs) 12

1.3.2 Meso-superstructured perovskite solar cells (MSSCs) 13

1.3.3 Planar heterojunction solar cells (PHJSCs) 14

1.4 Two-dimensional layered perovskite 15

1.4.1 $(PEA)_2A_{n-1}M_nX_{3n+1}$ 18

1.4.2 $(BA)_2A_{n-1}M_nX_{3n+1}$ 19

1.5 Lead-free perovskite materials 22

1.5.1 Copper-based perovskites 22

1.5.2 Bismuth-based perovskite 24

1.5.3 Tin-based perovskites 25

1.5.4 Germanium-based perovskites 29

1.6 Intention and organization of this work 32

Chapter 2 Synthetic techniques and characterization 34

2.1 Synthetic methods 34

2.1.1 Perovskite films processing 34

2.1.2 Perovskite single crystals processing 38

2.2 Characterization techniques 41

2.2.1 X-ray diffraction 41
2.2.2 Reflectance spectroscopy 43
2.2.3 Photoluminescence spectroscopy 46
Chapter3 Fabrication and characterization of organo-germanium bromide perovskite 50
3.1 Experimental section 51
3.1.1 Starting materials 51
3.1.2 Synthesis 51
3.1.3 Characterization 53
3.2 Results and discussion 58
3.2.1 Synthesis 58
3.2.2 Crystal structure description 60
3.2.3 X-ray diffraction analysis 66
3.2.4 Reflectance and photoluminescence 70
3.3 Conclusion 74
Chapter4 Fabrication and characterization of two-dimensional $(CH_3(CH_2)_3NH_3)_2GeI_4$ perovskite 75
4.1 Experimental section 76
4.1.1 Starting materials 76
4.1.2 Synthesis 76
4.1.3 Characterization 76
4.2 Results and discussion 77
4.2.1 Synthesis 77

4.2.2 X-ray diffraction analysis and crystal structure description 78

4.2.3 Reflectance and photoluminescence 81

4.3 Conclusion 83

Chapter 5 Summary and Outlook 85

Reference 88

Chapter 1 Introduction

In recent years, energy shortage, as the primary problem which hinders the development of economy and the global peace, has become the focus of concern around the world. The traditional fossil fuels, in addition to their limited amounts and non-renewability, will also bring severe contamination to the environment while in use. As one kind of clean and renewable energy, solar cells, which are attracting more and more attention, really means a lot to solving energy crisis. Under this circumstance, researchers from different countries are showing growingly great interest in developing new solar cells with high efficiency and low cost. Organometal halide perovskites is a kind of solar cell which is based on all-solid-state perovskites as the light-absorbing materials. Due to its excellent photoelectric properties, this kind of material has become the hot spot in the solar cells research field all over the world[1], and continuous breakthroughs have been made on the power conversion efficiency.

1.1 Development process of organometal perovskite solar cells

In fact, research on perovskite compounds has lasted for decades. PSCs was picked as a runner-up by the editors of Science for Top 10 Breakthroughs of 2013.[2][3] In the beginning, the excellent conductivity of perovskites was applied to organic light-emitting diodes (OLEDs) and thin-film transistors (TFTs).[4][5] In 2009, Miyasaka and co-workers became the first researchers who successfully employed $CH_3NH_3PbBr_3$and $CH_3NH_3PbI_3$ as photosensitizers to make liquid-electrolyte-based dye-sensitized solar cells, reaching a power conversion efficiency (PCE)of 3.81%.[6]

In 2011, using $CH_3NH_3PbI_3$as sensitizer, Park and co-workers [7][8] achieved a PCE of 6.54%by optimizing precursor concentration and sintering temperature of organic lead halide and processing the TiO_2 surface with $Pb(NO_3)_2$ solution, further improving the structure and properties of perovskite solar cells.

In 2012, instead of liquid electrolytes, Grätzel and Park et al. [9] introduced solid hole-transport material---spiro-OMeTAD, not only making the PCE get to 9.7%, but also prolonging the stability. Snaith et al. [10] adopted an extremely thin absorber (ETA) approach and replaced the mesoporous n-type $TiO_2$with insulting Al_2O_3 and got a PCE of 10.9%. Then more and more researchers entered this field, working out many inspiring experimental results, and leading perovskite solar cells to a high-speed development period.

In 2013, Grätzel et al. [11] described a sequential deposition method for the fabrication of solid-state mesoscopic solar cells in their paper, allowing for a power conversion efficiency of approximately 15%and a greatly increased reproducibility. In addition, by means of dual-source vapour deposition, Snaith et al. [12] raised the power conversion efficiency of planar heterojunction perovskite solar cell to 15.4%.

Usually, for both planar heterojunction and meso-superstructured solar cells, a compact TiO_2layer is needed as a selective contact for electron collection at the anode, whose sintering temperature, however, is above 400℃. And in 2014, Snaith et al. [13] realized a low temperature route (< 150℃) to a compact TiO_2 layer with highly crystallized nanoparticles, delivering a power conversion efficiency up tp 15.9%. Also, Han and co-workers [14] fabricated a perovskite solar cell using a double layer of mesoporous ZrO_2 and TiO_2which is covered by a porous carbon film, reaching a power conversion efficiency of 12.8%. Yang and co-workers[14], for the first time, by an inkjet printing technique, demonstrated a planar perovskite solar cell that incorporates a nanocarbon hole-extraction layer and got a power conversion efficiency of 11.6% as the result. Kelly et al. [15] used ZnO nanoparticles as an electron-transport layer to prepare flexible solar cells with power conversion efficiency over 10%.

Recently in the year of 2018, HJ Snaith et al. introduced a means based on a simple solution-processed secondary growth (SSG) technique and produced a wider bandgap top layer and a more n-type perovskite film, leading to an increase in open circuit voltage by up to 100 millivolts and a power conversion efficiency of 20.90%. [17]Via treating a mixed organic cation $MA_xFA_{1-x}PbI_3$ perovskite film with methylamine (MA) gas, MK Nazeeruddin et al. succeeded in new $MAPbI_3$/δ-$FAPbI_3$ structure and applied it in solar cells, boosting the device efficiency to 21%. [18]

At present, according to the statistics from NREL (National Renewable Energy Laboratory), latest power conversion efficiency has got to 23.3%, which is achieved by ISCAS (Institute of Chemistry–Chinese Academy of Sciences)[19]. All of these progresses are gradually leading the fabrication technique of perovskite solar cells to commercialization.

However, with further research on mechanism of perovskite solar cells, unusual characteristics have arisen, among which toxicity of lead and device stability and have led to a bottle neck for further development. As the final product of the decomposition of perovskites, PbI_2, i.e. lead bivalent cation, represents a higher toxic level than the conventional toxic Cd^{2+} in CdTe in their corresponding solar cell materials, which could be characterized by solubility (K_{sp}). The lead bivalent cation in PbI2 has a solubility order of 1×10^{-8}, much larger than the K_{sp} of Cd^{2+} in CdTe (on the order of about 1×10^{-22}). [18, 19] Thus, lead halide perovskites pose great threats to the ecosystem and even to our health, which should not be neglected.[20][21]

On the other hand, degradation is another issue hindering the large-scale deployment of perovskite solar cells. Due to the inherent instability of three-dimensional structures in perovskite compounds, they could be sensitive to moisture, heat and oxygen which restricts the outdoor photovoltaic applications.[22]

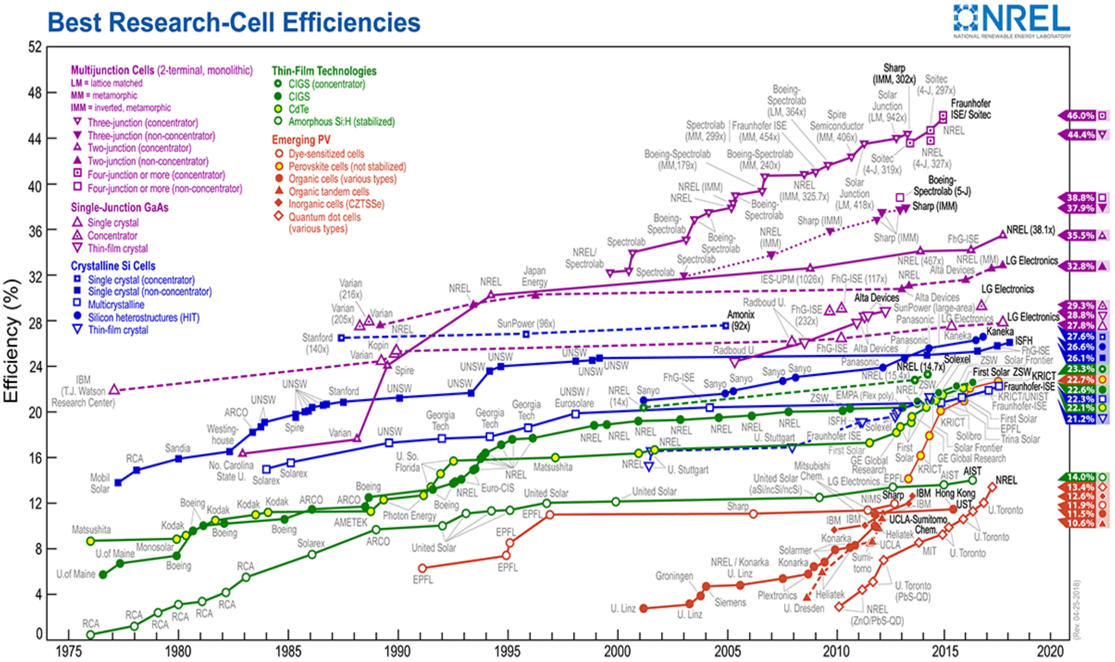

Fig. 1.1 Compiled values of the highest confirmed photo-conversion efficiencies for research solar cells to date [19]

1.2 Basic structure, constitution and properties of organometal perovskites

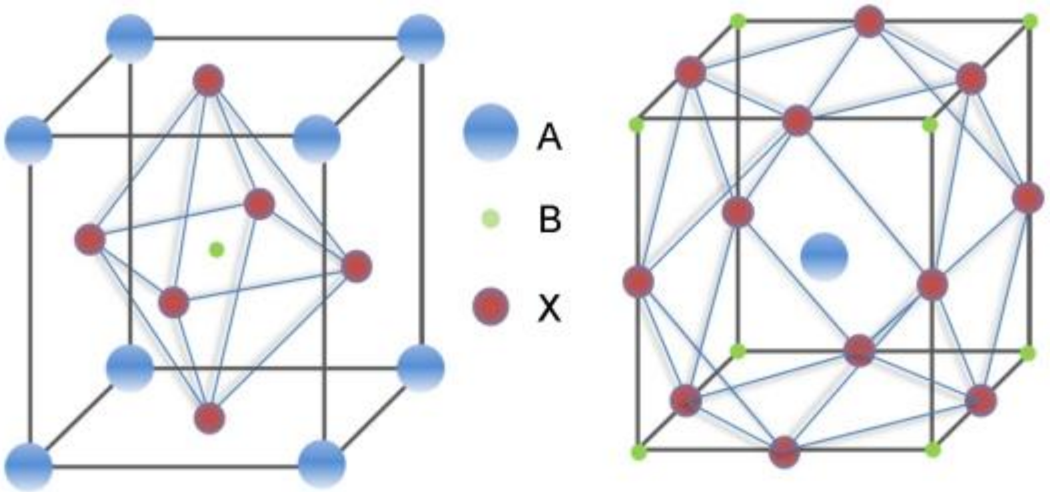

Fig. 1.2 Structure diagram of perovskites. A is monovalent cation, B is divalent cation, X is halide anion [21] [24]

Perovskites was named after a Russian scientist--- Lev Perovski. ABX_3 is the general formula, among which A and B are respectively monovalent and divalent cations with dramatically different volumes, and X is monovalent halogen anion. Under ideally symmetric conditions, located in the centre of cubic structure, cation A is surrounded by twelve anions X, and cation B is surrounded by six. And in the $[BX6]^{4-}$ octahedra, it shares corners in all three orthogonal directions to generate infinite three-dimensional (3D) $[BX_3]^-$ frameworks (Figure 1.2)[23].

To maintain the stability of the cubic structure, the ionic radii of A, B and X are supposed to satisfy a rule: the Goldshmidt tolerance factor t should be close to 1 $(0.9 \le t \le 1)$.

$$t = \frac{R_A + R_X}{\sqrt{2}(R_B + R_X)} \tag{1}$$

Here, R_A, R_B, R_X are the ionic radii of respective ions.

Generally, smaller t $(0.71 \le t \le 0.9)$ could lead to lower-symmetry structures, such as tetragonal phase (β phase) and orthorhombic phase (γ phase), while in contrast, larger t (t>1) could decrease the stability of the three-dimensional (3D) $[BX3]^-$ frameworks, even resulting in a two-dimensional (2D) layer structure (Figure 1.3).[24][25][26] Two-dimensional (2D) structure owns higher band gap than the three-dimensional (3D) one owing to the enhanced exciton binding energies as the excitons are confined in the inorganic layers. [25] Except the metal cation Cs^+, to date, only $CH_3NH_3^+$ (MA) and $HC(NH_2)_2^+$ (FA) can be used as the organic A cations. Cation A functions as structural template and its shape, size, and charge distribution are crucial factors for the stabilization of the perovskite structure[28]. The ionic radius of A could change the band gap. When its radius increases, the lattice expands, leading to smaller band gap and red shift of absorption edge, consequently resulting in larger short-circuit current and higher power conversion efficiency[29]. And the B metal cation can only be selected from a narrow set of elements including the bivalent rare earths [30], the alkaline earths[31] and the heavier group 14 elements (Ge^{2+}, Sn^{2+}, Pb^{2+})[23], in which Pb^{2+} is the most commonly used. Halide anions X usually are Cl^- ($R_X = 0.181$nm), Br^- ($R_X = 0.196$nm) or I^- ($R_X = 0.220$nm). Among them, the mechanical properties of bromide compounds are better than the iodide ones [32]. And with the increase of the ionic radii, a systematic shift of the absorption band edge to shorter wavelengths will show up [33]. This is because the electronegativity of halide ions decreases as their atom weights increase, then covalent interaction in X-B-X increases[34]. Above all, as organometal halide perovskites, there can only be specific combinations of cations A and B with halide anions X.

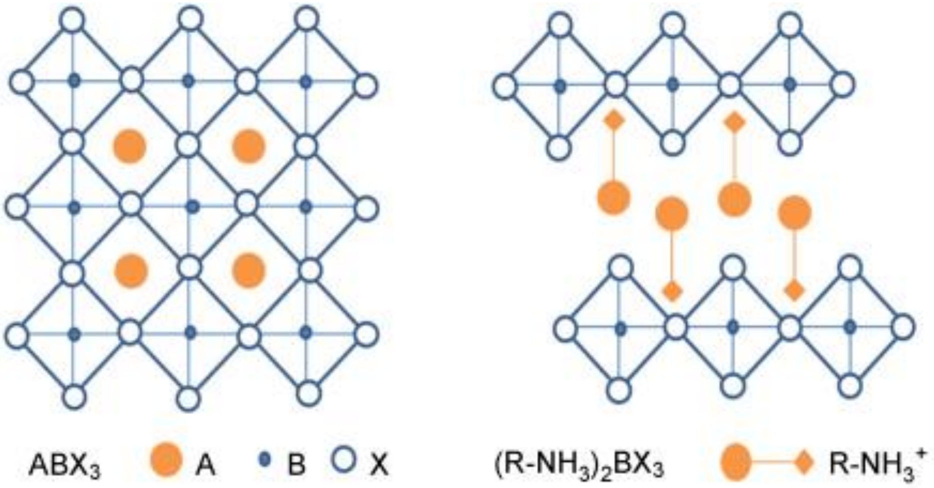

Fig. 1.3 The 2D structure and 3D structure of perovskite. A is aromatic or aliphatic monovalent cation, B is divalent cation, X is halide anion [28]

Analysis of X-ray diffraction (XRD) has identified cubic ($Pm\overline{3}m$), tetragonal (I4/mcm), and orthorhombic (Pnam) phases from organometal halide perovskite crystals, and transmission electron microscopy (TEM) has suggested a pseudocubic structure resulting from octahedral titling and/or rotations [35]. At room temperature, $CH_3NH_3PbI_3$ forms a tetragonal structure while $CH_3NH_3PbBr_3$ and $CH_3NH_3PbCl_3$ forms a cubic structure [36]. Generally speaking, their crystal structures undergo reversible, temperature-dependent phase transitions and symmetry increases with temperature [36][37]. Kanatzidis et al. [37]reported a common trend among halide perovskites that there are two phase transitions leading to three distinct structural modifications as temperature changes. These are classified as the high temperature α-phase, the intermediate temperature β-phase, and the low temperature γ- phase (summarized in Table 1[37][38][39])

Table 1 Structural phase transformations for commonly used hybrid perovskites[37][38][39]

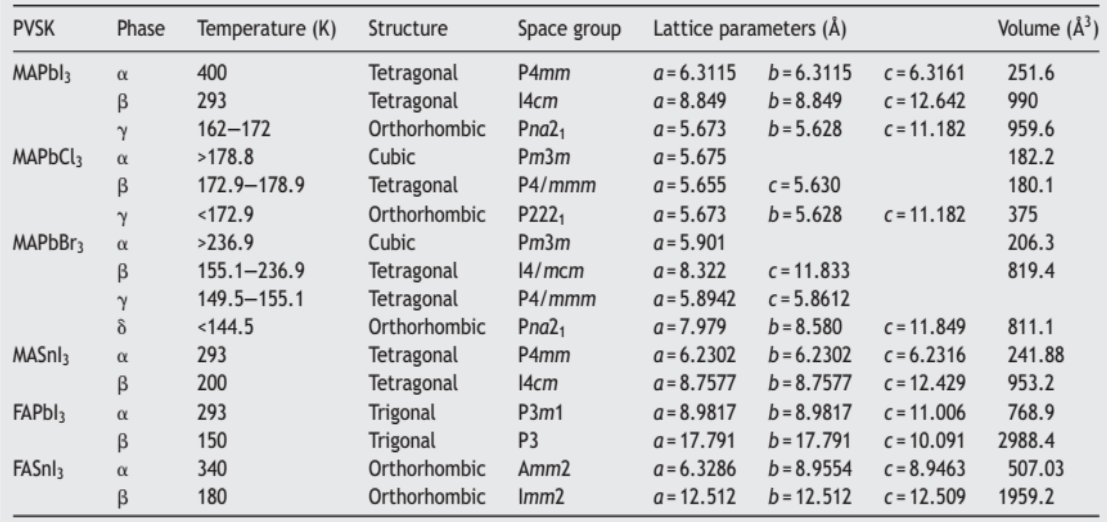

PVSK	Phase	Temperature (K)	Structure	Space group	Lattice parameters (Å)			Volume (Å^3)
$MAPbI_3$	α	400	Tetragonal	$P4mm$	$a = 6.3115$	$b = 6.3115$	$c = 6.3161$	251.6
	β	293	Tetragonal	$I4cm$	$a = 8.849$	$b = 8.849$	$c = 12.642$	990
	γ	162–172	Orthorhombic	$Pna2_1$	$a = 5.673$	$b = 5.628$	$c = 11.182$	959.6
$MAPbCl_3$	α	>178.8	Cubic	$Pm3m$	$a = 5.675$			182.2
	β	172.9–178.9	Tetragonal	$P4/mmm$	$a = 5.655$	$c = 5.630$		180.1
	γ	<172.9	Orthorhombic	$P222_1$	$a = 5.673$	$b = 5.628$	$c = 11.182$	375
$MAPbBr_3$	α	>236.9	Cubic	$Pm3m$	$a = 5.901$			206.3
	β	155.1–236.9	Tetragonal	$I4/mcm$	$a = 8.322$	$c = 11.833$		819.4
	γ	149.5–155.1	Tetragonal	$P4/mmm$	$a = 5.8942$	$c = 5.8612$		
	δ	<144.5	Orthorhombic	$Pna2_1$	$a = 7.979$	$b = 8.580$	$c = 11.849$	811.1
$MASnI_3$	α	293	Tetragonal	$P4mm$	$a = 6.2302$	$b = 6.2302$	$c = 6.2316$	241.88
	β	200	Tetragonal	$I4cm$	$a = 8.7577$	$b = 8.7577$	$c = 12.429$	953.2
$FAPbI_3$	α	293	Trigonal	$P3m1$	$a = 8.9817$	$b = 8.9817$	$c = 11.006$	768.9
	β	150	Trigonal	$P3$	$a = 17.791$	$b = 17.791$	$c = 10.091$	2988.4
$FASnI_3$	α	340	Orthorhombic	$Amm2$	$a = 6.3286$	$b = 8.9554$	$c = 8.9463$	507.03
	β	180	Orthorhombic	$Imm2$	$a = 12.512$	$b = 12.512$	$c = 12.509$	1959.2

1.3 Organometal halide perovskite solar cells

Power conversion efficiency is one of the most important parameters to evaluate solar cells. So the primary target on organometal halide perovskite solar cells is to obtain high efficiency. The power conversion efficiency of a solar cell is defined by the short-circuit current density (J_{SC}), open-circuit voltage (V_{OC}) and fill factor (FF). Short-circuit current density (J_{SC}) is the current density when the voltage across a device is zero, and open-circuit voltage (V_{OC}) is the voltage when the current density in the device is zero. The fill factor is the ratio between the maximum power ($P_{max} = J_{mp}V_{mp}$) generated by a solar cell and the product of V_{OC} with J_{SC}. These three parameters tightly interact with the quality of the perovskite film and perovskite composition[39][40][42][43], the interfacial contact [44][45][46][47], as well as the device architecture[35][48][49][50]. Basically, J_{SC} depends on the optical properties of the solar cell, such as absorption in the absorber layer and reflection. The V_{OC} correlates to the quasi-Fermi level of photo-excited perovskite and the electrode work function [35]. The fill factor (FF) is directly affected by the values of the cell's series resistance (R_S), shunt resistances (R_{sh}) and diodes losses. Increasing the shunt resistance (R_{sh}) and decreasing the series resistance

(R_S) lead to a higher fill factor, thus resulting in greater efficiency. In this section, various device architectures of perovskite solar cells and their recent advances will be introduced.

1.3.1 Dye-sensitized solar cells (DSSCs)

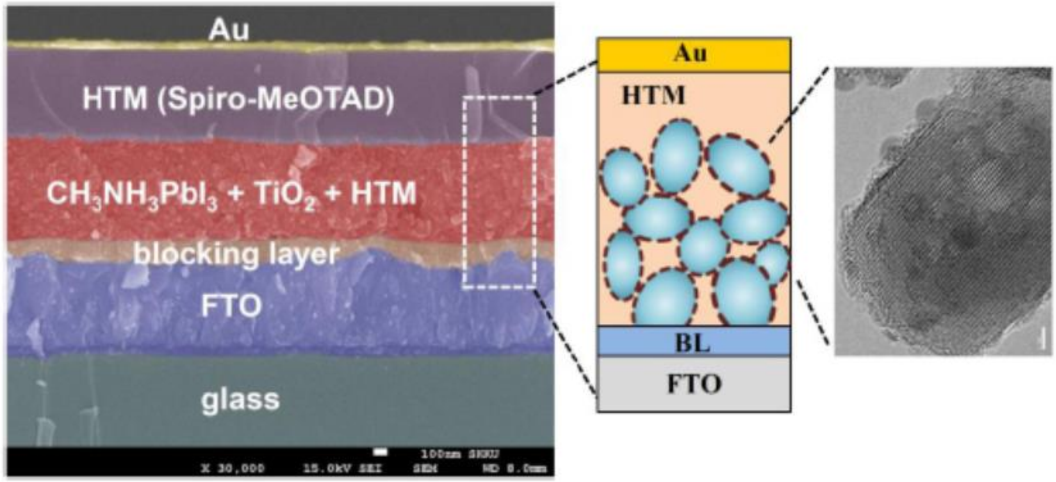

Fig. 1.4 Device architecture (Left) and cross-sectional SEM image (Right) of perovskite-sensitized solid-state solar cell [52]

In 2009, Kojima et al. [51] initially attempted to use spin-coated three-dimensional perovskites of $CH_3NH_3PbX_3$ (X = Br or I) as light absorbers in dye-sensitized solar cells (DSSCs). Power conversion efficiencies (PCE) of 3.13% and 3.81% were achieved from tribromide and triiodide perovskites respectively, among which, the comparatively higher PCE of triiodide perovskite resulted from its narrower bandgap energy. DSSCs is a kind of electrochemical solar cells which includes sensitized mesoscopic titanium oxide (TiO_2), attached by a catalyst layer and a liquid electrolyte in a sandwich-like architecture. In 2011, by using GBL (gamma-butyrolactone) as the solvent during the fabrication of $CH_3NH_3PbI_3$ film, Park et al. [8] succeeded in substantially boosting the power conversion efficiency (PCE) into 6.5%, which was almost double of the previous one and became the record among reported quantum dot (QD) solar cells. Nevertheless, the solar cell was rather unstable and $CH_3NH_3PbI_3$

tended to dissolve in polar liquid electrolytes.

To solve this problem which held back the development of perovskite solar cells, in 2012, the first version of long-term durable perovskite solar cell was developed [9]. In the solid-state sensitized solar cell, instead of the liquid electrolyte, spiro-MeOTAD, a hole transport material (HTM), was infiltrated in the mesoporous TiO_2 film (Figure 1.4). Forming on the TiO_2 surface, $CH_3NH_3PbI_3$ functions as a light-harvesting active layer. As light is absorbed in the perovskite, electrons will be transported to the TiO_2, while holes will be transported to the HTM. Under this circumstance, a PCE of 9.7% was achieved.

Afterwards, the solid-state perovskite solar cell boomed, and the PCE has been further enhanced. A two-step spin-coating method, using CH_3NH_3I intercalation following layered PbI_2 deposition was introduced by Grätzel's group[53] to replace the one-step method. As a result, the quality of perovskite was improved and the PCE was raised up to 15%. Then, another solid-state perovskite solar cell, with an average efficiency exceeding 16% was enabled by the growth of $CH_3NH_3PbI_3$ cuboids with a controlled size via a two-step spin-coating [53].

1.3.2 Meso-superstructured perovskite solar cells (MSSCs)

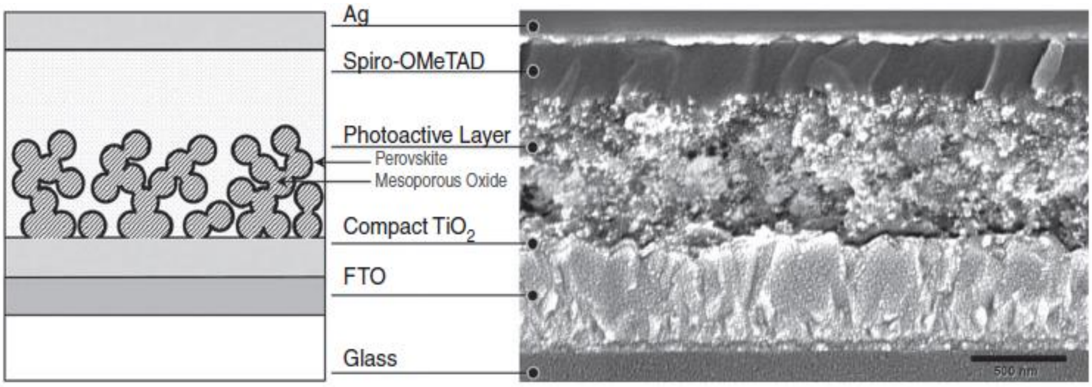

Fig. 1.5 Left: Device architecture of meso-superstructured perovskite solar cell, where the mesoporous oxide is Al_2O_3. Right: Cross-sectional SEM image of a full device incorporating mesoporous Al_2O_3.[55]

In the meso-superstructured perovskite solar cell (MSSC), Snaith et al. [55] replaced the mesoporous n-type TiO_2 with insulating Al_2O_3 and got a power conversion efficiency of 10.9%. The device architecture is illustrated in Fig.1.5. The Al_2O_3 is an insulator with a wide band gap (7 to 9 eV) and purely acts as a “scaffold” upon which the perovskite is coated. Electron transport through the perovskite layer is observed much faster than through the n-type TiO_2, and an increased open-circuit voltage (V_{OC}) is found as well. The higher V_{OC} was attributed to a higher quasi-Fermi level of the electrons on the perovskite compared to TiO_2.

Inspired by the new meso-superstructure, other oxides have also been applied in the similar way. Mei et al. [56]fabricated a perovskite solar cell that uses a double layer of mesoporous TiO_2 and ZrO_2 as a scaffold infiltrated with perovskite, giving a PCE of 12.8%. In addition, Hwang et al. [57] substituted TiO_2 with size-controlled SiO_2 nanoparticles (NPs) as the scaffold layer and achieved a PCE of 11.45%.

1.3.3 Planar heterojunction solar cells (PHJSCs)

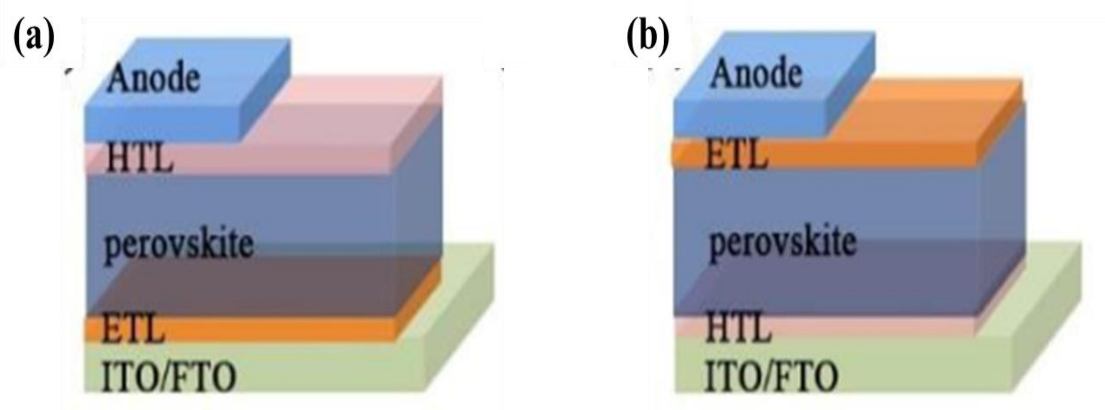

Fig. 1.6 Device architectures of planar heterojunction solar cells: (a) regular (n-i-p). (b) inverted (p-i-n) [58]

Benefited from the high ambipolar mobilities of perovskite, perovskite solar cells can also afford a simple planar heterojunction between perovskite and HTM instead, avoiding the harsh processing of mesoporous TiO_2 [58]. As can be seen from Figure

1.6, the planar devices include regular (n-i-p) [59] and inverted (p-i-n) [60] devices, depending on which selective contact is used atop of transparent electrode. Due to the simplicity of planar heterojunction solar cells, efforts have been made on (a) material selection for the appropriate HTL/ETL and interface engineering, and (b) deposition techniques to produce high quality films [39].

Liu et al. [59] realized this planar structure by introducing mixed halide perovskite ($CH_3NH_3PbI_{3-x}Cl_x$) via dual source vapour-deposition, yielding a maximum PCE of 15.4%. And the device structure consisted of FTO/compact TiO_2/$CH_3NH_3PbI_{3-x}Cl_x$/spiro-MeOTAD/Au. In 2014, Zhou et al. [23] obtained an extremely high PCE of 19.4%. In their work, ITO, instead of FTO was used as the electrode, which was further modified with poly-ethyleneimine ethoxylated (PEIE) to reduce the work function of ITO. By doping the TiO_2 electron transport layer with Yttrium (Y), the carrier concentration was enhanced. Recently, by using a solution-processed secondary growth (SSG) technique, Luo et al. [61] introduced a means to deliver a wider bandgap region and a more n-type perovskite film ($(FA_{0.95}PbI_{2.95})_{0.85}(MAPbBr_3)_{0.15}$). The SSG procedure includes two steps: (a) thepreparation of perovskite films by solution processing and (b) the secondary growth with the assistance of guanidinium bromide (which we abbreviate SSG-G). This improvement enabled the planar heterojunction solar cell with a PCE approaching 21%.

1.4 Two-dimensional layered perovskite

While conventional three-dimensional organometal halide perovskites are still undergoing strikingly rapid development, the low-dimensional perovskite crystals have recently attracted increasing interest because of their unique structures and properties. In contrast with the sensitivity of three-dimensional perovskites to oxygen, humidity, light and heat, the low-dimensional ones with naturally sharp quantum wells exhibit superior environmental stability.

For halide perovskites, the structure could be 3D, 2D, 1D, or even 0D, depending on how the metal halide octahedra are connected to each other. By choosing appropriate inorganic and organic components, the crystallographic structures can be finely controlled with the inorganic units, e.g., metal halide octahedra (MX_6), forming zero- (0D), one- (1D), two- (2D), and three-dimensional (3D) structures in the hybrids. In the 3D structure, small-sized cations, such as Cs^+ and $CH_3NH_3^+$, fit into the corner-sharing metal halide octahedra to form a framework with the MX_6 network. In the 2D structure, the MX_6 octahedra are connected in layered or corrugated sheets at the corners; in the 1D structure, the MX_6 octahedra are connected in a chain (at the corners, edges, or faces); and in the 0D structure, the MX_6 octahedra are isolated and surrounded by organic cations. Thus, there are actually two kinds of 2D halide perovskites. One kind is the perovskite crystals and nanostructures with 2D nanostructured morphology that are grown from 3D perovskite materials; these are more like traditional 2D materials such as graphene and TMDs. The other type is the intrinsic 2D layered crystal structure. They are basically electronically “2D” even in the bulk because of the quantum confinement in each of the MX_6 layers that are separated by organic cation dielectric layers.[62] Considering the large exciton binding energy of traditional two-dimensional perovskites, the latter quasi-two-dimensional materials, i.e., the Ruddlesden–Popper layered perovskites, combining merits of three-dimensional and two-dimensional ones, seem even more promising and attractive.

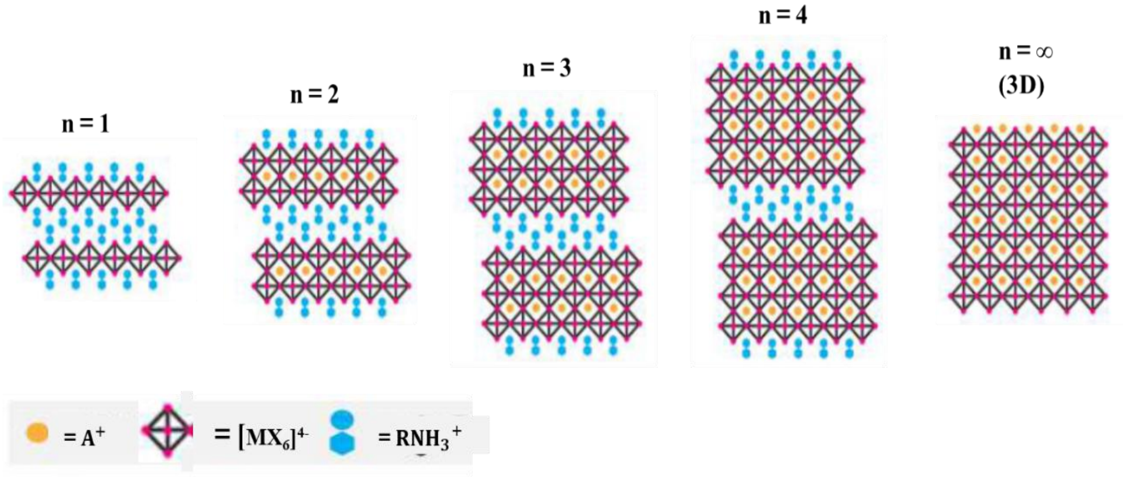

Fig. 1.7 Schematic crystal structures of quasi-2D layered (n = 1, 2, 3) and 3D perovskites [63]

The quasi-two-dimensional perovskites take the general formula of $(RNH_3)_2A_{n-1}M_nX_{3n+1}$ (n = 1, 2, 3, 4……), where RNH_3 is a large aliphatic or aromatic alkylammonium cation acting as a spacer between the perovskite layers (Fig. 1.7)—for example, 2-phenylethylammonium (PEA) and n-butylammonium (n-BA), A is monovalent organic cation, such as $CH_3NH_3^+$ (MA^+) and $HC(NH_2)_2^+$ (FA^+), M is a divalent metal cation, X is a halide anion, and n is the layer number of three-dimensional perovskite. Among them, the A and M cations, together with the X anions constitute the perovskite framework. In the quasi-two-dimensional structures, the n layers of corner-sharing $[MX_6]^{4-}$ octahedral are sandwiched between two layers of long chain organic cations and they are held together by a combination of Coulombic and hydrophobic forces which offer them air stability. This crystal structure could be regarded as natural quantum wells with the inorganic and organic layers respectively acting as the “wells” and “barriers”, giving rise to the exciton binding energy [64][65]. Then the excitons would be confined within the inorganic layers. And the stability of excitons in the n = 1 two-dimensional perovskites would result in an intense photoluminescence (PL) which makes this kind of material applicable to light-emitting diodes (LEDs) [66][67].

With various options in the organic spacer cations, the structures of two-dimensional perovskites seem to be more flexible than that of three-dimensional ones. And the properties of the 2D materials, in turn, are greatly influenced by the spacers. Table 2 lists the molecular structures of organic spacer cations that apply to two-dimensional perovskites [68]. Among them, PEA^+ ($C_6H_5(CH_2)_2NH_3^+$) and BA^+ ($CH_3(CH_2)_3NH_3^+$) cations are the most commonly used.

Table 2 Chemical structures of organic spacer cations in 2D perovskites [68]

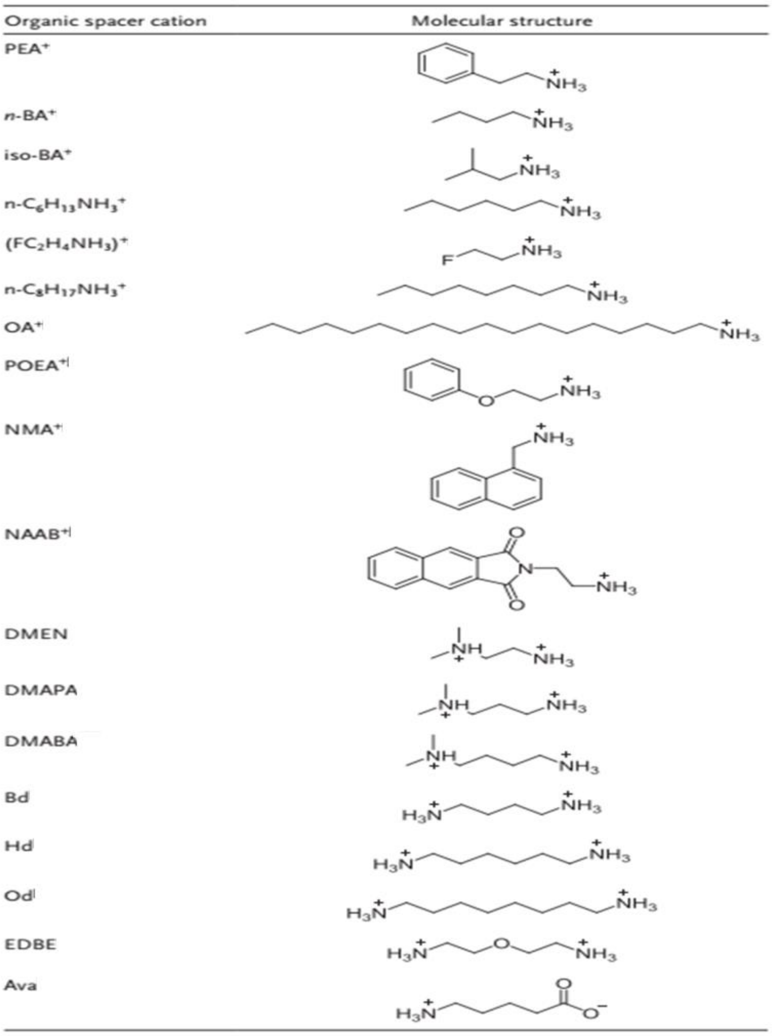

Organic spacer cation	Molecular structure
PEA^+	
n-BA^+	
iso-BA^+	
n-$C_6H_{13}NH_3^+$	
$(FC_2H_4NH_3)^+$	
n-$C_8H_{17}NH_3^+$	
OA^+	
$POEA^+$	
NMA^+	
$NAAB^+$	
DMEN	
DMAPA	
DMABA	
Bd	
Hd	
Od	
EDBE	
Ava	

1.4.1 $(PEA)_2A_{n-1}M_nX_{3n+1}$

In 2014, Smith et al. [69] reported the first attempt to use layered $(PEA)_2(MA)_2Pb_3I_{10}$ (n = 3) as the absorber in planar solar cell, showing an open-circuit voltage of 1.18 V and a power conversion efficiency of 4.73%. Although the power conversion efficiency (PCE) was much lower than that of three-dimensional $MAPbI_3$, their excellent stability was rather impressive and inspiring considering the additional reflections appeared in the PXRD pattern and the significant changes showed in the absorption spectra after 46 days of humidity exposure,.

Later on, by synthesizing micrometer-sized $(PEA)_2PbBr_4$ nanoplates using solvent vapor annealing, Liang et al. [70] successfully integrated this layered perovskite material into LEDs and achieved efficient room-temperature violet electroluminescence at 410 nm. In this way, the performance of optoelectronic devices based on two-dimensional perovskite material was enhanced significantly.

1.4.2 $(BA)_2A_{n-1}M_nX_{3n+1}$

As to the two-dimensional layered $(CH_3(CH_2)_3NH_3)_2(CH_3NH_3)_{n-1}Pb_nI_{3n+1}$, i.e., $(BA)_2(MA)_{n-1}Pb_nI_{3n+1}$, Constantinos C. Stoumpos' group[71] firstly and successfully implemented them in solid-state solar cells, achieving a power conversion efficiency of 4.02%, an open-circuit voltage (V_{OC}) of 929mV and a short-circuit current density (J_{SC}) of 9.42 mA/cm^2 from the n = 3 compound.

The crystal structures and corresponding XRDs of $(BA)_2(MA)_{n-1}Pb_nI_{3n+1}$ (n = 1, 2, 3, 4) and the three-dimensional $MAPbI_3$ are illustrated in Fig. 1.8. Considering the orientation of the structure on the substrate, there is an obvious tendency. In the case of $(BA)_2(MA)_{n-1}Pb_nI_{3n+1}$, except the n = 1 compound, whose layers grew parallel to the substrate, the others, as the inorganic layers become thicker, exhibit a developing trend towards vertical growth.

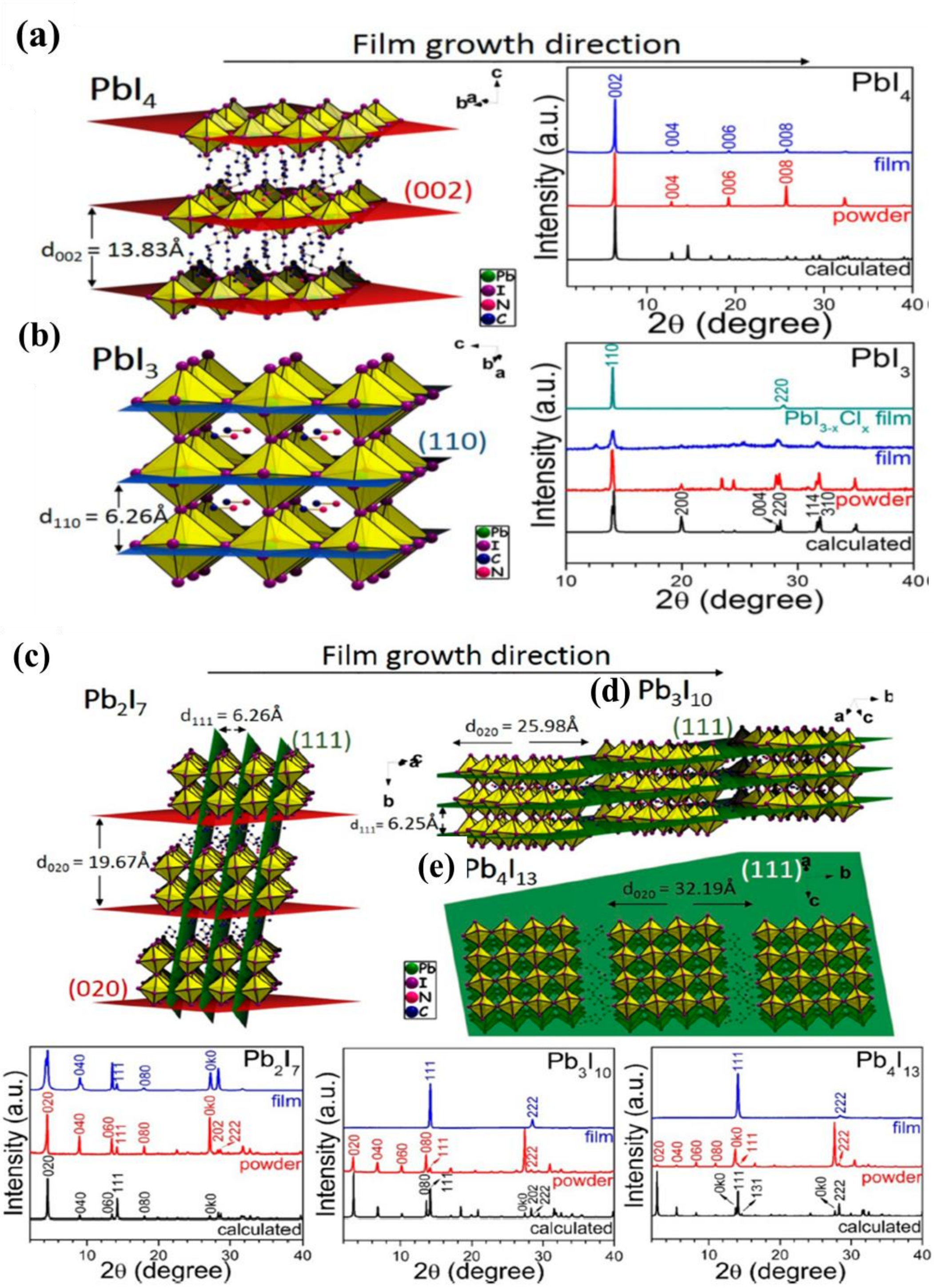

Fig. 1.8 Crystal structures and XRDs of (a) (BA)$_2$PbI$_4$, (b) MAPbI$_3$, (c) (BA)$_2$(MA)Pb$_2$I$_7$, (d) (BA)$_2$(MA)$_2$Pb$_3$I$_{10}$, and (e) (BA)$_2$(MA)$_3$Pb$_4$I$_{13}$ perovskites, with the illustration of their respective diffraction planes. [71]

In regard to optical properties, which could be concluded from Fig. 1.9, the optical band gaps (E_g) in these homologous perovskites increase with the thickness decrease of inorganic slabs from 1.52 eV (n = ∞) to 2.24 eV (n = 1). This phenomenon is caused by quantum confinement effects from the dimensional reduction of the perovskite.[71][72][73][74]

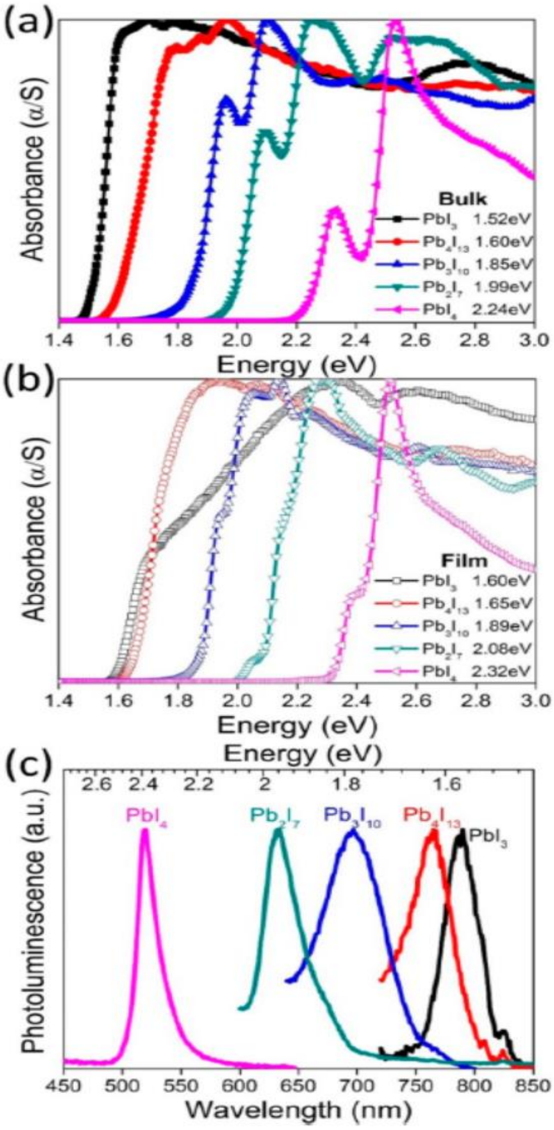

Fig. 1.9 Optical band gaps of (a) bulk, (b) spin-coated TiO2− perovskite thin films, and (c) PL spectra of spin-coated glass−perovskite thin films of the $MAPbI_3$ and $(BA)_2(MA)_{n-1}Pb_nI_{3n+1}$ compounds.

In spite of rapid development and improvement on two-dimensional Ruddlesden-Popper perovskites, some of the defects and puzzles due to their unique and complicated crystal structure cannot be neglected either as they could even impede the further development. The sandwich-like structure lowers the carrier mobility and further become the obstacle of high power conversion efficiency. More importantly, the relationship among molecular structure, crystal orientation, transport dynamics and device performance has yet to be established on 2D perovskites, which is detrimental for their further developments of optoelectronics. [68]

1.5 Lead-free perovskite materials

Although lead halide perovskites have been developing rapidly and shows great potential for even higher power conversion efficiency and broad application perspective, their drawbacks, which is known that the soluble lead salts are toxic upon the exposure to human, and the release in environment causes pollution [75][76][77][78], still cannot be ignored. Therefore, it is desirable to replace lead with environment-friendly elements and enormous efforts have been devoted to low-toxic lead-free metal halide perovskite materials. Theoretical studies [75][79][80] suggest that the Pb^{2+} cation plays a very important role in determining the electronic structure of Pb-based perovskites and participates in forming the conduction band minimum (CBM) and valence band maximum (VBM) of perovskites, especially the lone pair electrons $6s^2$ in the Pb^{2+} ion. And as is discussed above, the organic cation A plays the key role in stabilizing the perovskite structure.

Hence, it is not easy to substitute Pb^{2+} cation without reducing the performance of perovskite materials. For the moment, copper (Cu), bismuth (Bi), tin (Sn) and germanium (Ge) have been applied to replace lead.

1.5.1 Copper-based perovskites

Because of the much smaller ionic radius of Cu^{2+} cation compared with Pb2+, unlike the usual three-dimensional structure, Cu-based perovskites tend to present a two-dimensional structure as shown in figure 1.10(c) [81]. They can be typically structured in the type of $(RNH_3)_2CuX_4$, where RNH_3^+ could be different aliphatic or aromatic ammonium cations and X represents halogen or mixed halogen anions. [82]Generally, Cu-based perovskites could be fabricated under ambient condition by a relatively simple solution process due to its stability in air. [83] Very recently, a series of $(CH3NH3)_2CuCl_x Br_{4-x}$ perovskites have been evaluated and it was interesting to find that Cl incorporation is essential to stabilize the Cu^{2+} cation to avoid any reduction reactions.[81][82][83][84] By tuning the Br/Cl ratio, Cortecchia et al. could adjust the light absorption range of the Cu-based perovskite light absorber. The optical band gap of $(CH_3NH_3)_2CuCl_x Br_{4-x}$ can change from 2.48 eV (500nm) for $(CH_3NH_3)_2CuCl_4$ to 1.80 eV (689nm) for $(CH_3NH_3)_2CuCl_{0.5}Br_{3.5}$. Unfortunately, the highest power conversion efficiency they got is only 0.017% ($(CH_3NH_3)_2CuCl_2 Br_2$).[81] In addition, Cui et al. reported Cu-based perovskite solar cells using $(CH_3CH_2CH_2CH_2NH_3)_2CuBr_4$ and $(F\text{-}C_8H_8NH_3)_2CuBr_4$ fabricated under ambient condition, achieving power conversion efficiencies of 0.63% and 0.51%, respectively. [82][83]

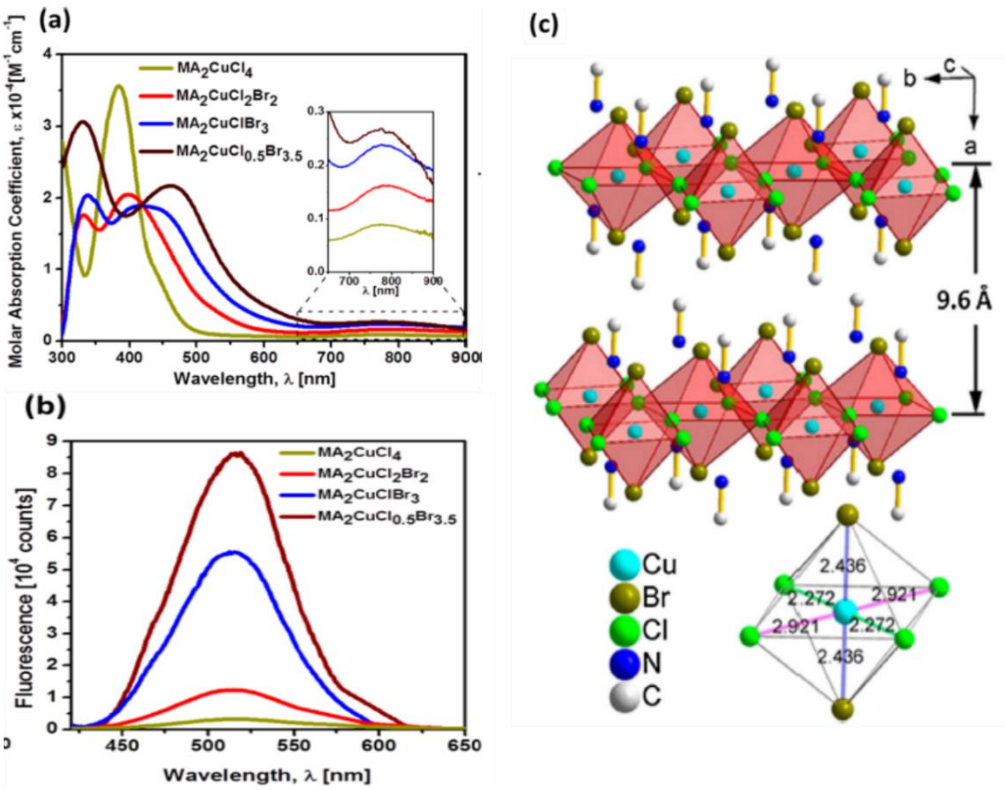

Fig. 1.10 (a) Absorption coefficient for perovskites of the series $(CH_3NH_3)_2CuCl_xBr_{4-x}$ and broad d−d transitions between 700 and 900 nm (inset). (b) Photoluminescence of the perovskites $(CH_3NH_3)_2CuCl_xBr_{4-x}$. (c) Crystal structure of $(CH_3NH_3)_2CuCl_2Br_2$ [81]

1.5.2 Bismuth-based perovskite

Bismuth is an interesting candidate for being used in lead-free halide perovskites with comparable ionic radius (103 pm) to lead (119 pm)[85]. Organic bismuth-based metal halide perovskites include a large group of materials due to the various possibility in the connections between the adjacent bismuth halide octahedra (corner-, edge- and face- sharing networks) and dimensionality ranging from zero-dimensional dimer units, to one-dimensional chain-like motifs or two-dimensional layered networks up to three-dimensional double perovskite frameworks [86][87][88]. Different from the conventional perovskite structure of ABX_3, Bi-based halide perovskites generally exist in the form of $A_3Bi_2X_9$,

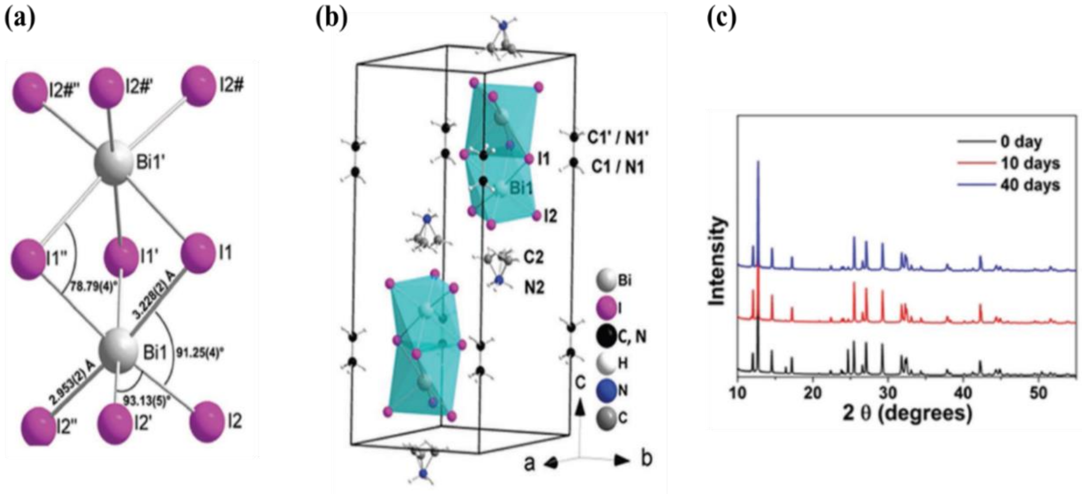

Fig. 1.11 (a) The unit cell of $(CH_3NH_3)_3Bi_2I_9$. (b) The crystal structure of $Bi_2I_9^{3-}$ anion. [89] (c) XRD patterns of the $(CH_3NH_3)_3Bi_2I_9$ film on the FTO substrate under different exposure time to the ambient air[90]

As can be seen from figure 1.11(a), unlike the traditional corner-sharing octahedra structure of three-dimensional $CH_3NH_3PbI_3$ perovskite, $(CH_3NH_3)_3Bi_2I_9$ exhibits a zero-dimensional perovskite structure with bioctahedral $(Bi_2I_9)^{3-}$ clusters and the surrounding cations such as $CH_3NH_3^+$.[89][90][91]Via the solution-processing followed by thermal annealing at proper temperature or via vapor-assisted methods [92], thin films can be obtained, while single crystals can be grown by a layer crystallization technique [89]. With the mesoscopic architecture on a TiO2/ITO substrate through one-step spin-coating, X Zhang et al. successfully synthesized a $(CH_3NH_3)_3Bi_2I_9$-based solar cell with improved power conversion efficiency of 0.42% and a relatively high Voc of 0.66 V. [93]But still, the performance of Bi-based perovskite solar cells is not good, especially compared with that of the Pb-based ones.

However, Bi-based perovskites present remarkably improved stability in ambient condition. It has been reported that solar cells based on $(CH_3NH_3)_3Bi_2I_9$ demonstrated excellent stability for more than 40 days upon continuous exposure to the humidity and ambient air at room temperature (Fig. 1.11 (c)). [90] And the device showed very limited performance degradation even after storage in air for 21 days. So the bismuth-based halide perovskites/derivatives are still promising for further research in both photovoltaics and other semiconductor based technologies. [84]

1.5.3 Tin-based perovskites

Sn^{2+} metal cations are the most likely substitute for Pb^{2+} in the perovskite structure since they both belong to group 14 in the periodic table which leads to similar chemical properties. Also, they have similar ionic radius (Pb^{2+}: 119 pm, Sn^{2+}: 110 pm [94]). So it is possible to form a perovskite with a basic formula $ASnX_3$ (X = halide) in analogy to lead compounds. And similar to lead halide perovskites, the structure of tin-based perovskites can be strongly influenced by cation A. While small A cations, such as $CH_3NH_3^+$ and $CH(NH_2)_2^+$ lead to three-dimensional perovskites, larger ones like $C_4H_7NH_3^+$ could cause the formation of low-dimensional structures. [95][96]

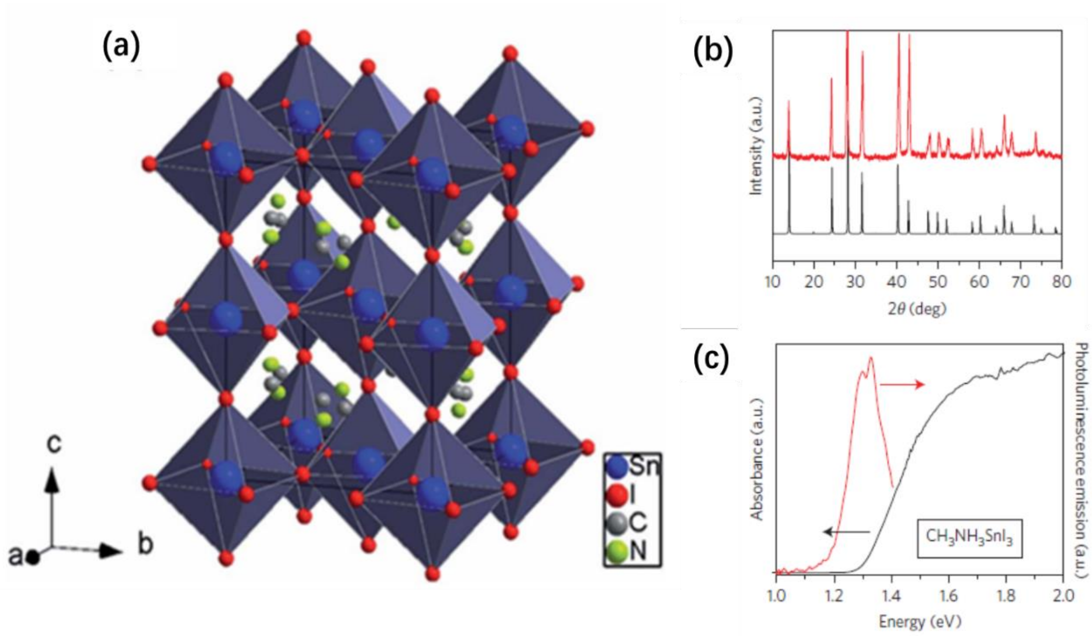

Fig. 1.12 (a) Perovskite crystal structure of $CH_3NH_3SnI_3$. (b) Experimental (red) and simulated (black) X-ray diffraction pattern for $CH_3NH_3SnI_3$. (c) Optical absorption and photoluminescence spectra of $CH_3NH_3SnI_3$ [97]

$CH_3NH_3SnI_3$ is one of the most deeply studied tin halide perovskites, which, normally crystallizes in the pseudocubic P4mm space group with corner-sharing $[SnI_6]^{4-}$ octahedra spreading into a three-dimensional perovskite structure (Figure 1.12a).[84][97] Compared to $CH_3NH_3PbI_3$, which has a lower symmetry (β-phase) at room temperature, $CH_3NH_3SnI_3$ exists with a more symmetric phase (α-phase), even at room temperature. And the Sn analogue has a broader absorption onset of 950 nm, corresponding to a lower direct bandgap ($CH_3NH_3SnI_3$:1.30 eV, $CH_3NH_3PbI_3$: 1.55 eV).[97] A detailed summary of structural and optical data of typical organo-tin halide perovskites and their power conversion efficiencies applied in solar cells is presented in Table 3[98].

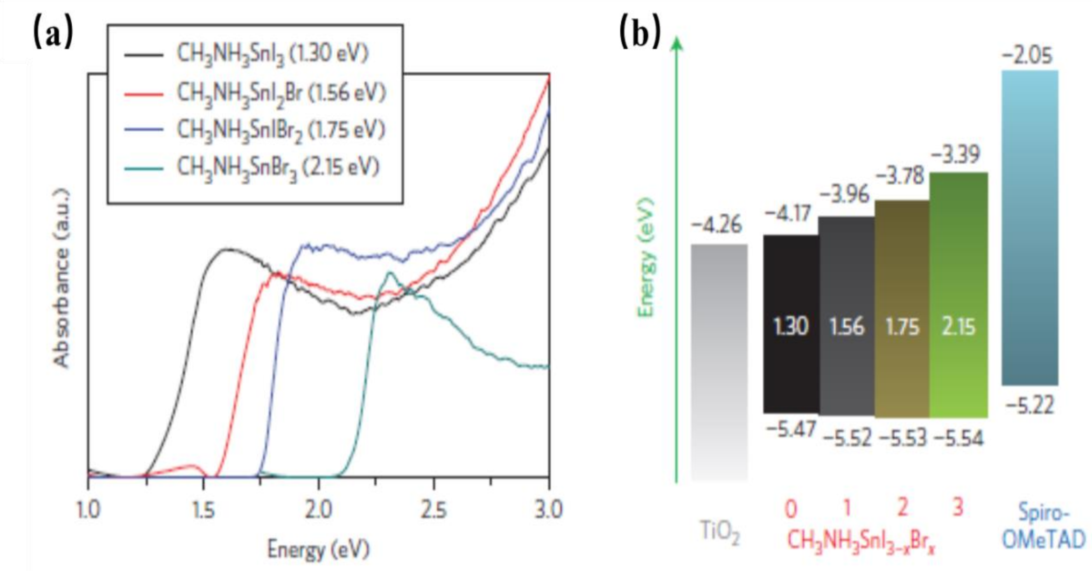

Fig. 1.13 (a) Absorption spectra of the $CH_3NH_3SnI_{3-x}Br_x$ (x = 0, 1, 2, 3) perovskites. (b) Schematic energy-level diagram of $CH_3NH_3SnI_{3-x}Br_x$ [97]

Noel et al. [98] firstly reported the lead-free tin halide perovskite----$CH_3NH_3SnI_3$ used as absorber material in solar cells and achieved a power conversion efficiency of 6.4% with a high open-circuit voltage (V_{oc}) of 0.88V, which is the highest efficiency obtained so far. Meanwhile, F. Hao et al. [97] demonstrated a power conversion efficiency of 5.23%. However, considering the decreased stability of Sn^{2+} in ambient conditions resulting from being oxidized into Sn^{4+}, the organo-tin halide perovskites usually degrade quickly and thus show poor reproducibility. Therefore, complete device assembly process being performed in a glove box with low oxygen and humidity levels has been a prerequisite for tin-based halide perovskite solar cells. [84][97][98][99][100]. To improve the stability of tin-based perovskites, partially replacing Sn with Pb would be advisable. Zuo et al. [101] studied the mixed $MASn_{1-x}Pb_xI_3$ perovskites and by optimizing Sn concentration, they achieved a very promising power conversion efficiency of 10.1% when the content of Sn is 15%. The TD-DFT (Time-dependent density functional theory) calculation indicates that the bandgap of $CH_3NH_3Sn_{1-x}Pb_xI_3$ would decrease as x (x < 0.5) increases because of the stronger spin-orbit coupling of Pb, while the bandgap of $CH_3NH_3Sn_{1-x}Pb_xI_3$ would increase as x (x > 0.5) increases owing to the phase transition from P4mm to I4cm at x > 0.5. [75][102]

Table 3 Structural and optical data of organo-tin halide perovskites and the highest obtained PCEs (if applied in photovoltaic devices) [98]

Perovskite	Sim./exp.	Crystal system (space group)	Dimensionality	Band gap/eV	PCE/%	References
$CH_3NH_3SnBr_3$	Exp.	Pseudocubic (P4mm)	3D	2.15-2.2	4.27	[97] [104]
$CH_3NH_3SnIBr_2$	Exp.	Pseudocubic (P4mm)	3D	1.75	5.73	[97]
$CH_3NH_3SnI_2Br$	Exp.	Pseudocubic (P4mm)	3D	1.56	5.48	[97], [103]
$CH_3NH_3SnI_3$	Exp.	Pseudocubic (P4mm) Tetragonal (P4mm)	3D	1.27-1.35 1.21-1.35	5.23 6.4	[97],[105], [106] [95], [98]
$CH(NH_2)_2SnI_2Br$	Exp.	Orthorhombic (–)	3D	1.68	1.72	[100]
$CH(NH_2)_2SnI_3$	Exp.	Orthorhombic (Amm2)	3D	1.4-1.41	6.22	[95],[107],[108], [109]

By adjusting the composition of halide anion, a variety of tin halide perovskites including mixed halide ones is available with calculated band gaps ranging from 1.7 eV to 3.0 eV.[98][103] With $CH_3NH_3SnBr_3$ being used in planar solar cells, Jung et al. [104]reported power conversion efficiencies of 0.35% (co-evaporation) and 1.12% (sequential deposition). Hao et al.[97] reported a mixed iodide–bromide tin perovskite semiconductor ($CH_3NH_3SnIBr_2$) with an optical band gap of 1.75 eV yielding a power conversion efficiency of 5.73% in meso-structured perovskite solar cells. Figure 1.13a shows the absorption properties of the mixed halide tin perovskites and Fig. 1.13b the corresponding energy levels of the compounds. With increasing Br/I ratio in the mixed halide, the absorption onset of $MASnI_{3-x}Br_x$ perovskites exhibit blue shift, corresponding to enlarged band gaps, thus resulting in significant colour tunability for perovskite photovoltaic devices. [97]

1.5.4 Germanium-based perovskites

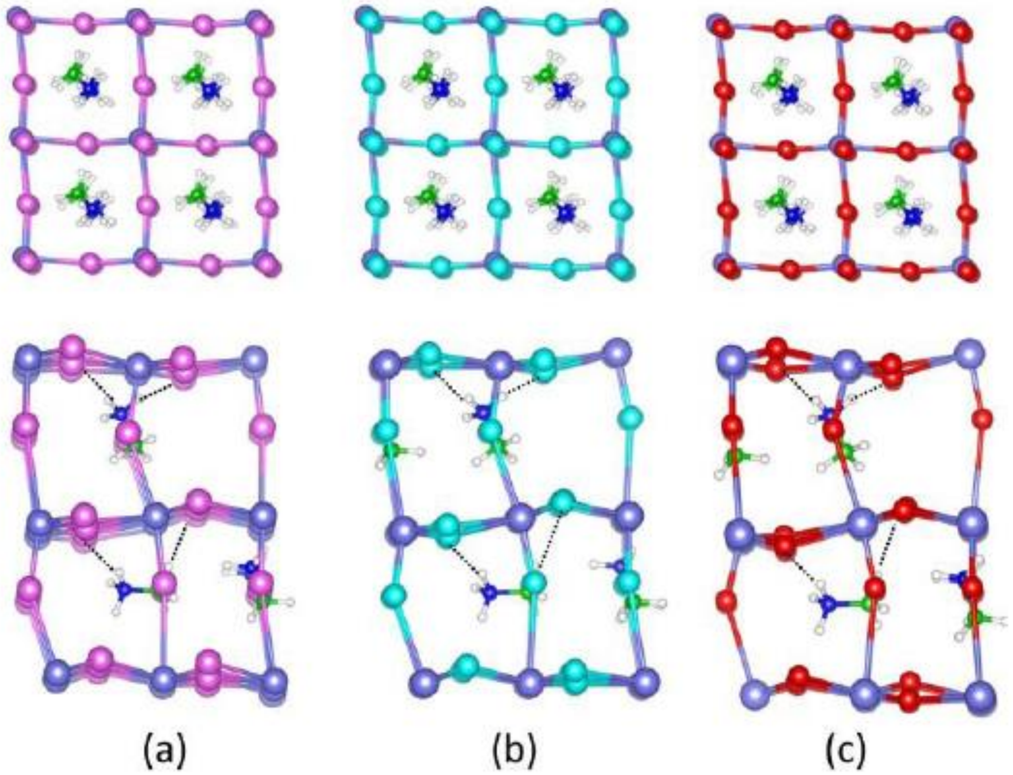

Fig. 1.14 Optimized stable geometries of (a) $CH_3NH_3GeI_3$, (b) $CH_3NH_3GeBr_3$, (c) $CH_3NH_3GeCl_3$. The upper panel is top view, the under panel is side view. (purple: Ge; pink: I; cyan: Br; red: Cl; green: C; blue: N; white: H) The dash lines are the hydrogen bonds[110]

Besides tin (Sn), germanium (Ge) is another possible candidate in the group 14 for the substitution of lead in the perovskite structure. Despite the same oxidation state to Pb^{2+}, Ge^{2+} demonstrates a more covalent character with a lower electronegativity and a smaller ionic radius (Ge^{2+}: 73 pm, Pb^{2+}: 119 pm) [85][94]. Given by the calculation [110], the Goldschmidt tolerance factor for $CH_3NH_3GeI_3$, $CH_3NH_3GeBr_3$, $CH_3NH_3GeCl_3$ crystal structures are 0.965, 0.988, 1.005, respectively, which indicating the empirically ideal three-dimensional perovskite structure.

Fig. 1.14 shows the optimized stable geometries of methylammonium germanium halide perovskites ($CH_3NH_3GeX_3$, X = Cl^-, Br^-, I^-). As depicted in Fig. 1.14, the optimized frameworks of $CH_3NH_3GeX_3$ perovskites all exhibit distorted structures, i.e., Ge – X···Ge and Ge···X – Ge. And from chlorine to iodine, the distortion degree tends to decrease, which may be caused by their high ionic conductivity. [110]

By first-principle calculations, Lu et al. [111] reported that $CH_3NH_3GeX_3$ (X = Cl^-, Br^-, I^-) are direct-bandgap semiconductors, with a decline tendency of calculated bandgap as the halide ionic radius increases (Table 4). However, the monoclinic Ge-based perovskites of $MOGeI_3$ and $GAGeI_3$ are indirect-bandgap semiconductors.

Table 4 Structural and optical data of organo-germanium halide perovskites and the highest obtained PCEs (if applied in photovoltaic devices) [88]

Perovskite	Sim./exp	Crystal system (space group)	Dimensionality	Band gap/eV	PCE/%	References
$CH_3NH_3GeCl_3$	Sim.	Trigonal	3D	3.74–3.76	-	[110][111]
$CH_3NH_3GeBr_3$	Sim.	Trigonal	3D	2.76–2.81	-	[110][111]
$CH_3NH_3GeI_3$	Exp.	Trigonal (R3m)	3D	1.9–2.0	0.20	[111][112][113]
$CH(NH_2)_2GeI_3$	Exp.	Trigonal (R3m)	3D	2.2–2.35	-	[111][112][113]
$MOGeI_3$	Exp.	Monoclinic ($P2_1$)	3D	2.5	-	[111][112]
$GAGeI_3$	Exp.	Monoclinic ($P2_1/c$)	3D	2.7	-	[111][112]
$TAGeI_3$	Exp.	Hexagonal ($P6_3$)	3D	2.8	-	[112]
$PAGeI_3$	Exp.	Tetragonal ($I\bar{4}2d$)	3D	2.7	-	[112]

MO acetamidinium, GA guanidinium, TA trimethylammonium, PA isopropylammonium

Although various simulation and calculation results on germanium halide perovskites have been obtained, rarely experimental data have been reported. This is partly due to the chemical instability of divalent Ge^{2+} cation, which can be even more easily oxidized into tetravalent cation than Sn^{2+} cation. As a result, the solar cells using Ge-based perovskites usually suffer from very poor open circuit voltages (V_{OC}) [113]. Stoumpos et al. [112] used $CsGeI_3$ as the prototype compound and respectively prepared $CH_3NH_3GeI_3$ (1), $HC(NH_2)_2GeI_3$ (2), $CH_3C(NH_2)_2GeI_3$ (3), $C(NH_2)_3GeI_3$ (4), $(CH_3)_3NHGeI_3$ (5), $(CH_3)_2C(H)NH_3GeI_3$ (6) and analogues via a direct and reproducible approach which is based on precipitation of crystals from acid solution. As a result, compounds (1)-(3) precipitated with three-dimensional structures whereas compounds (4)-(6) formed one-dimensional infinite chains. The incorporation of the small polar organic molecule in place of Cs ions has a dramatic effect in the electronic structure of the semiconductors introducing a large opening of the band gap as the cation size increases even within the same structure type.

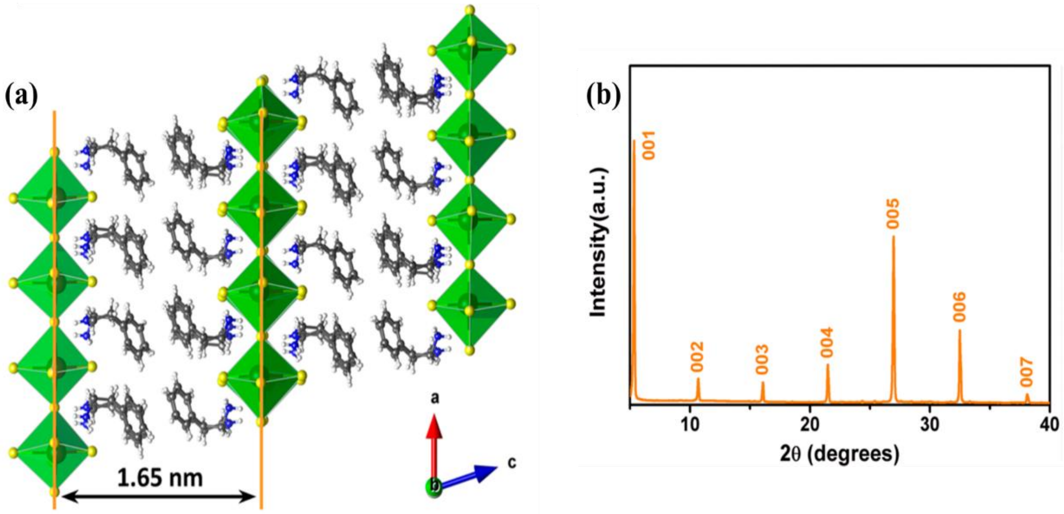

Fig. 1.15 (a) Crystal structure of the layered two-dimensional perovskite $(PEA)_2GeI_4$, viewed along the b axis. Violet, yellow, gray, blue, and white spheres represent Ge, I, C, N, and H atoms, respectively. (b) PXRD patterns[114].

Cheng et al. [114], via the similar fabrication method to that of Stoumpos mentioned above, obtained a layered two-dimensional germanium perovskite (Fig. 1.15), $(PEA)_2GeI_4$ (PEA $=C_6H_5(CH_2)_2NH_3^+$), with a direct band gap of 2.12 eV. Structural characterization demonstrated that, in this two-dimensional perovskite, the inorganic germanium iodide planes are separated by organic PEAI layers, which improved the stability of this Ge-based perovskite (Fig. 1.16). After exposed to 60% relative humidity for two days, the diffraction pattern of $(PEA)_2GeI_4$ almost stayed the same, while $CH_3NH_3GeI_3$ showed obvious CH_3NH_3I and GeI_4 peaks, indicating decomposition and oxidation of $CH_3NH_3GeI_3$. So this work provides a direction for the development of germanium halide perovskites.

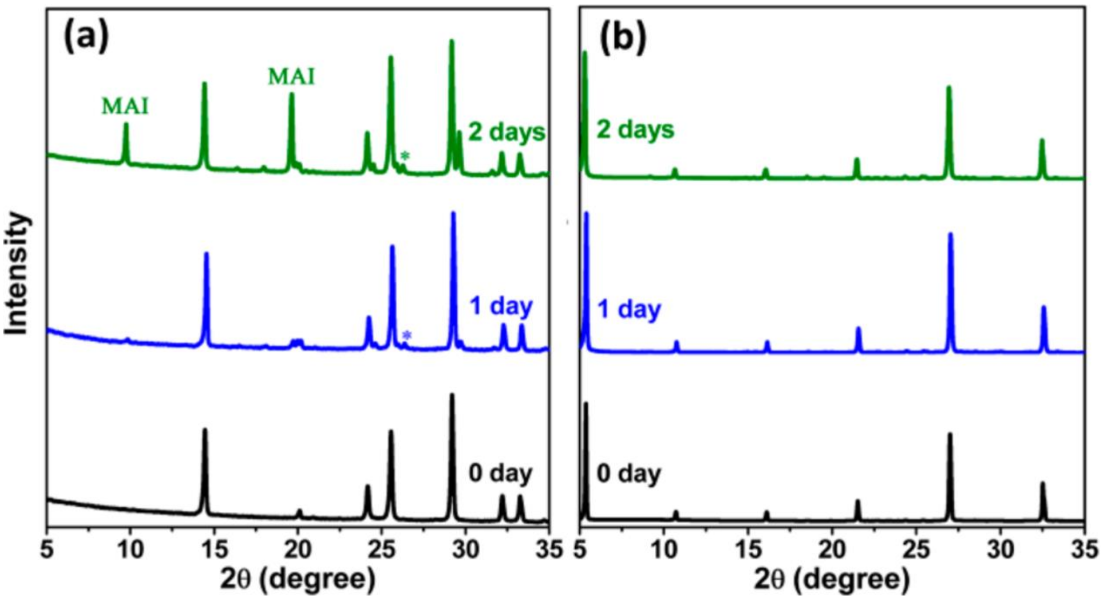

Fig. 1.16 PXRD of $MAGeI_3$ (a) and $(PEA)_2GeI_4$ (b), which are exposed to 60% relative humidity at 25 °C.

Although far from the theoretically possible power conversion efficiency of 27.9% predicted by Qian et al. [115], the experimental data is only about 3% [116], there is still broad space for the development of Ge-based perovskites. If the efficiency and stability can be improved pronouncedly, germanium halide perovskites could be ideal candidate for photovoltaic applications.

1.6 Intention and organization of this work

As discussed above, although organo-lead halide perovskites display outstanding photoelectric properties and even higher power conversion efficiency, still, the toxicity of lead is an inevitable problem which has to be resolved. Indeed, several environmental-friendly elements, such as tin (Sn) and germanium (Ge), have been put forward as promising substitutes. However, they are even more sensitive to ambient condition. Enhancing the stability of the substitutes for lead will be a big challenge.

In this thesis, we shall substitute germanium (Ge) for lead (Pb) in organometal halide perovskites. Furthermore, starting with three-dimensional germanium halide bromide and iodide, we put more effort on the fabrication and optimization of layered quasi-two-dimensional germanium perovskites, as well as on the corresponding crystal structures and photophysical properties. In chapter 2, the synthesis methods and characterization will be introduced. The results of characterizations and related photophysical properties of both 2D and 3D organo-bromide halide perovskites are given and discussed in chapter 3. Similar discussion about organo-iodide halide perovskite are listed in chapter 4.

Chapter 2 Synthetic techniques and characterization

2.1 Synthetic methods

2.1.1 Perovskite films processing

To achieve good performance of perovskite solar cells, film quality is one of the key factors. High power conversion efficiency (PCE) calls for high-quality perovskite films with appropriate morphology, crystallinity, uniformity, phase purity and corresponding photoelectronic properties. And all of these requirements further depend on synthetic method, precursor composition, solvent selection, fabrication environment, etc. Speaking of the synthetic methods, several common ways can be summarized as follows: a) spin-coating; b) vapour deposition; and c) in-situ impregnation. Regardless of the differences among these methods, for organometal halide perovskites, they are all based on this reaction:

$$\mathrm{R}-\mathrm{N}H_3X+MX_2\rightarrow R-NH_3MX_3 \qquad (2.1)$$

Here, $\mathrm{R}-$ represents organic group, M^{2+} means bivalent metal cation, and X^- is monovalent halide anion. $CH_3NH_3PbI_3$ will be taken as the example to illustrate the fabrication processes in detail

2.1.1.1 Spin-coating

Spin-coating technique has been the most popular for preparation of perovskite films as it is time-saving, simple to operate and able to offer advisable films. And there are two routes included: one-step spin-coating and two-step spin-coating (Fig. 2.1 [117]). For the one-step spin-coating technique, organic halide CH_3NH_3I and lead halide PbI_2 are dissolved in an appropriate solvent such as a polar aprotic solvent like N, N-dimethylformamide (DMF), gamma-butyrolactone (GBL), or dimethyl sulfoxide

(DMSO) to obtain a precursor solution. Being kept at about 70℃ before deposition, a small amount of precursor is dropped onto the substrate which is fixed on the spin-coater, spreading and then forming a thin film by centrifugal force during the high-speed rotation. The following step is to anneal the $CH_3NH_3PbI_3$ film on the hotplate at 100℃ for 70 minutes or so.

Before the two-step spin-coating, PbI_2 and CH_3NH_3I are dissolved in N, N-dimethylformamide (DMF) and anhydrous isopropanol, respectively. With 70℃ solution temperature, a PbI_2 layer is first spin-coated on the substrate and dried on the hotplate at 70℃ for 10 minutes. Then the CH_3NH_3I solution is spun on PbI_2 layer, followed by a 100℃-annealing procedure for one hour to get perovskite crystals.

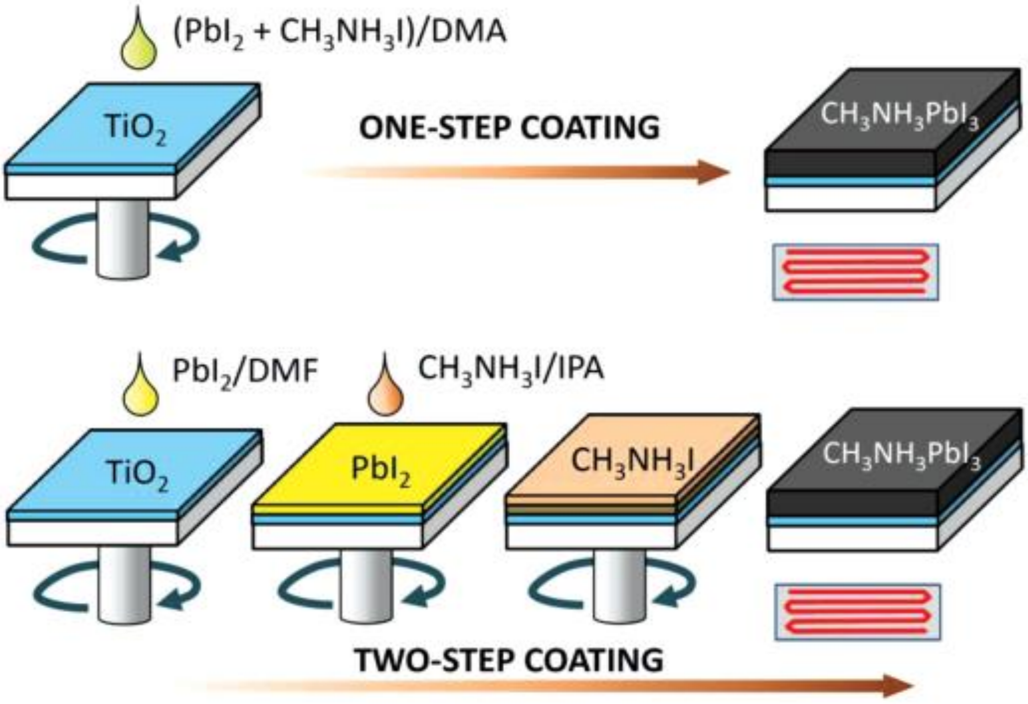

Fig. 2.1 One-step and two-step spin-coating process to obtain $CH_3NH_3PbI_3$ perovskite films. DMA, DMF, and IPA represent dimethyl acetamide, dimethyl formamide, and isopropyl alcohol, respectively. [117]

Since organo-metal halide perovskites exhibit a large degree of tolerance in composition variation and can form high-quality films within a wide range of precursor ratios [118], CH_3NH_3I and PbI_2 do not have to be added with strict 1: 1 stoichiometry.

Nevertheless, it is of great importance to control other parameters during experiment such as processing temperature, spinning rate and time, etc. [118][119][120]

Comparing these two methods, single-step precursors can hardly form a continuous film for planar configurations due to surface energy and nucleation [121], while two-step spin-coating could exhibit better photovoltaic performance due to better morphology and interfaces [117][122].

2.1.1.2 Vapor deposition

The dual-source thermal evaporation was first used on fabrication of organometal halide perovskites by Snaith et al. in 2013 [123]. As illustrated in Fig. 2.2 (a), the substrate is fixed in the upper part of the deposition system, while the solid precursor salts, CH_3NH_3I and PbI_2 are at the bottom, being evaporated separately and simultaneously to form planar perovskite film on the substrate, after which heat treatment will help with the crystallization.

Compared to the spin-coating process, thermal evaporation seems to be better for thickness control and produce better uniformity of the perovskite films, subsequently resulting in good performance.

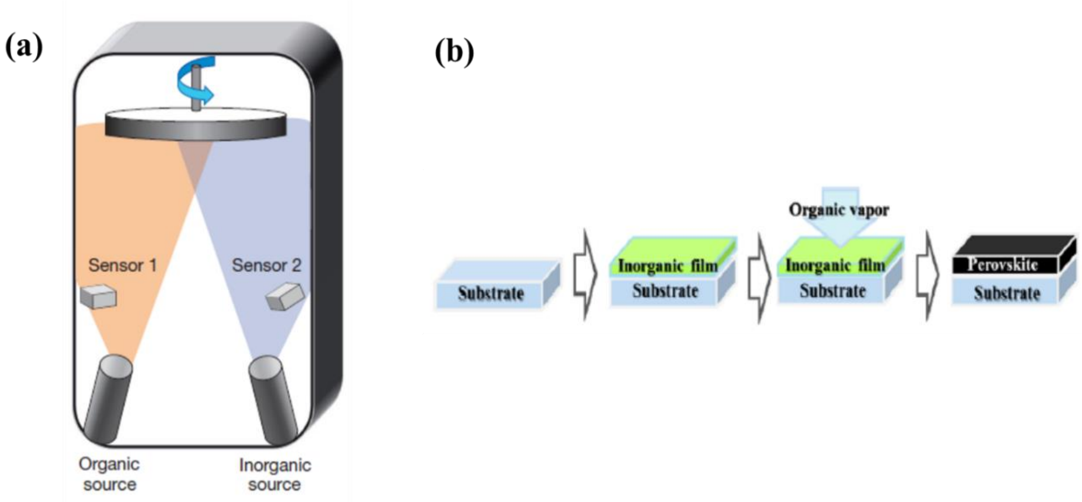

Fig. 2.2 The preparation of $CH_3NH_3PbI_3$ films using vapor deposition methods: (a) dual-source thermal evaporation using $PbCl_2$ and CH_3NH_3I sources [123]; (b)

vapor-assisted deposition using CH_3NH_3I organic vapors to react with pre-deposited PbI_2 films [124]

Given the requirement of thermal deposition for high vacuum, the vapor-assisted solution process (VASP) (Fig. 2.1 (b)) via in situ reaction could be the alternative. Similar to the spin-coating method, PbI_2 film is deposited on the substrate in the beginning. In the following step, the substrate will be annealed in vapor at 150°C in nitrogen atmosphere for 2 hours to form perovskite film. [124]

This hybrid deposition provides films with full surface coverage and uniform grain structure with microscale grain size, suitable for PV applications.

2.1.1.3 Sequential deposition

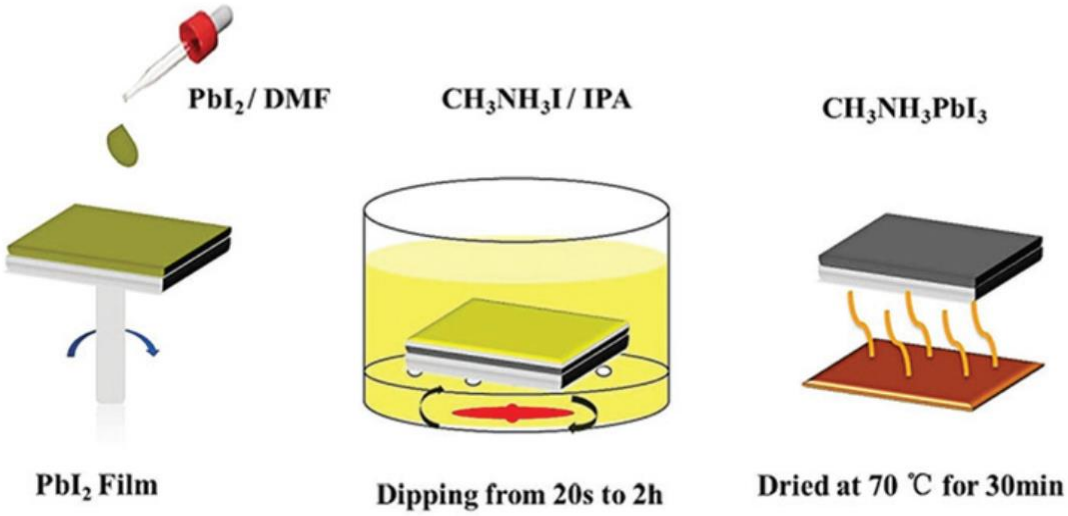

Fig. 2.3 Schematic illustration of the sequential deposition of a $CH_3NH_3PbI_3$ film [125]

It is clear from Fig. 2.3 that sequential deposition is a hybrid process consisting of spin-coating and dipping steps. The formation of PbI_2 framework is manipulated in the same way as above. Subsequently, the film is dipped into a solution of CH_3NH_3I in 2-propanol for some time, rinsed with 2-propanol and dried at 70°C for 30 minutes. [125]

The sequential deposition method for the fabrication of perovskite films introduce a means to achieve excellent photovoltaic performance with high reproducibility. And through varying the dipping time, perovskite grain size and surface roughness could be controlled. But due to the large formation energy of $CH_3NH_3PbI_3$, once dipped into CH_3NH_3I solution, PbI_2 will be converted into $CH_3NH_3PbI_3$ rapidly, which could lead to incomplete perovskite conversion. [126]

2.1.2 Perovskite single crystals processing

Charge carrier lifetime, mobility, and diffusion length are the three key parameters related to the power conversion efficiency (PCE) of perovskites. The demand for further improvements in these three figures of merit has aroused interest and research in synthesizing single-crystal perovskites due to their low trap-state densities. [127]

2.1.2.1 Inverse temperature crystallization (ITC)

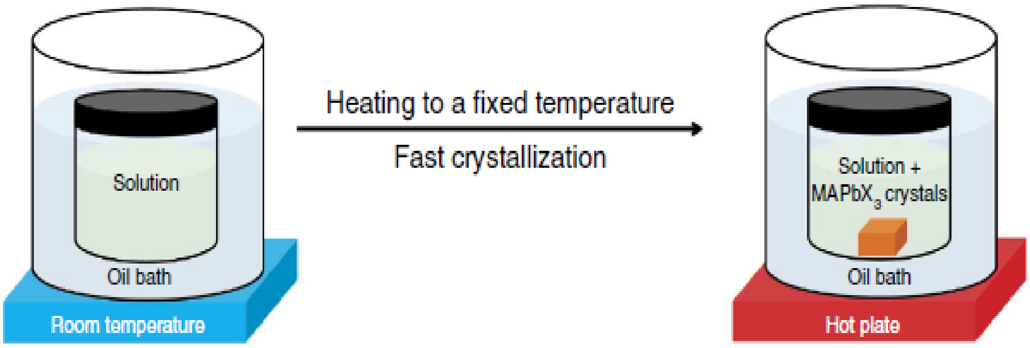

Fig. 2.4 Schematic illustration of the ITC method. The crystallization vial with the solution inside is immersed in an oil bath, being heated from room temperature and kept at an elevated temperature (80°C for $MAPbBr_3$ and 110°C for $MAPbI_3$) to initiate the crystallization. [128]

It has been reported before that the solubility of perovskite compounds would vary with solvents, and $CH_3NH_3PbI_3$ shows better crystallinity in gamma-butyrolactone (GBL), while $CH_3NH_3PbBr_3$ crystallizes more in N, N-dimethylformamide (DMF). [127] However, for both $CH_3NH_3PbI_3$/GBL and $CH_3NH_3PbBr_3$/DMF solution, there exists an inverse solubility phenomenon, i.e., their solubilities decline sharply as temperature respectively increases from 60°C to 110°C for $CH_3NH_3PbI_3$ and from 25°C to 80°C for $CH_3NH_3PbBr_3$. [128] Therefore, if being kept at the elevated temperature for a long time, $CH_3NH_3PbX_3$ (X = I, Br) crystal will precipitate and grow gradually. This is exactly inverse temperature crystallization (ITC) method, which could be seen from Fig. 2.4.

Via this technique, qualified single crystals with both controlled size and shape could precipitate and grow rapidly, showing good transport properties. [128]

2.1.2.2 Antisolvent vapor-assisted crystallization (AVC)

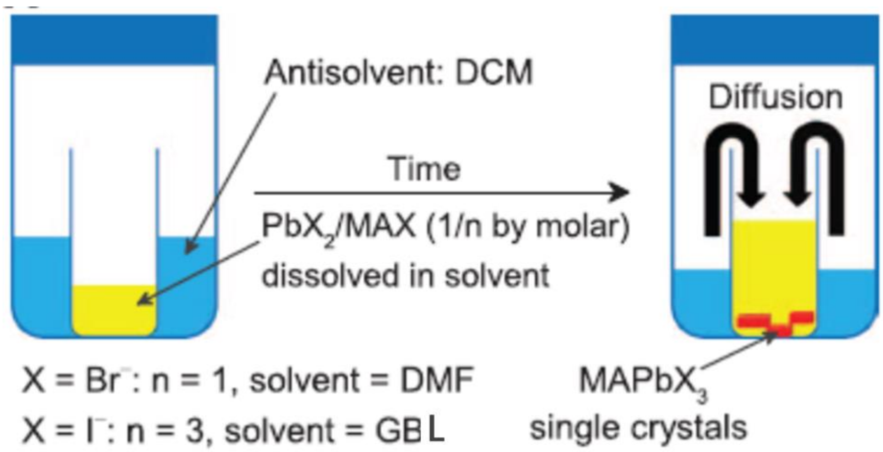

Fig. 2.5 Schematic diagram of the crystallization process. [127]

The antisolvent vapor-assisted crystallization (AVC) is easier to operate and control as heating is not necessary here. PbI_2 and CH_3NH_3I are dissolved in gamma-butyrolactone (GBL) to acquire $CH_3NH_3PbI_3$/GBL solution. Afterwards, the crystallization vial containing the precursor is put into antisolvent dichloromethane (DCM) without sealing. Dichloromethane (DCM) is used here not only because of its extremely poor dissolving capacity for both methylammonium halide salt and lead halide salt, but because of the disability to form hydrogen bonds which would minimize asymmetric interactions with the ions. Gradually, with the vapor of antisolvent slowly diffusing into the solution, red $CH_3NH_3PbI_3$ crystallizes and grows up. [127]

Despite time-consuming, the antisolvent method could afford regular and even millimeter-sized single crystals, further prolonging the carrier diffusion lengths.

2.1.2.3 Cooling crystallization

The cooling crystallization is a traditional method that has been developing for a long time. Generally, it is defined as the formation of solid with desirable and consistent properties from a solution, where the solubility of the target compound is limited at a certain temperature and its solubility line is rather sensitive to decrease of temperature. [129] Upon cooling, the solution will finally be supersaturated and then crystals start to nucleate and grow. But before that, there exists a meta-stable zone, where existing crystals grow, but no new crystals are formed (Fig. 2.6). [130]

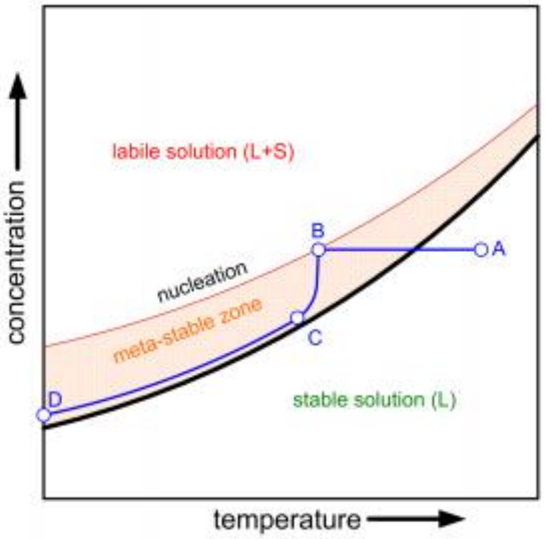

Fig. 2.6 Solubility curve and metastable zone [130]

In this work, cooling crystallization method is adopted to prepare germanium bromide and germanium iodide perovskite single crystals. Considering the poor stability of germanium divalent cation, we mainly concentrate on the two-dimensional compounds, with the three-dimensional ones fabricated as the control. The synthesis is based on crystallization of germanium perovskites from haloid acid solutions containing hypophosphorus acid (H_3PO_2) functioning as the reducing agent to reduce germanium dioxide (GeO_2) and to restrain Ge^{2+} from being oxidized into Ge^{4+} again. Besides, the whole process is implemented under a nitrogen atmosphere to further protect Ge^{2+}. GeO_2 is first added into the mixture of hypophosphorus acid solution and haloid acid solution and dissolved upon heating. Then corresponding organic halide salts CH_3NH_3X and $CH_3(CH_2)_3NH_3X$ ($X = Br^-$, I^-) are put into the solution in order. About 30 minutes after all the chemicals dissolve, the solution is left to cool down and crystals would precipitate slowly.

2.2 Characterization techniques

2.2.1 X-ray diffraction

X-ray diffraction is a technique used for determining the atomic and molecular structure of a crystal, in which the crystalline structure cause a beam of incident X-rays to diffract into many specific directions. By measuring the angles and intensities of these diffracted beams, a crystallographer can produce a three-dimensional picture of the density of electrons within the crystal. From this electron density, the mean positions of the atoms in the crystal can be determined, as well as their chemical bonds, their crystallographic disorder, and various other information.

A beam of radiation will only be diffracted when it impinges upon a set of planes in crystal, defined by the Miller indices (hkl), if the geometry of the situation fulfils quite specific conditions, defined by Bragg's law:

$$n\lambda = 2d_{hkl}\sin\theta \qquad (2.2)$$

where n is an integer, λ is the wavelength of the radiation, d_{hkl} is the interplanar spacing (the perpendicular separation) of the (hkl) planes and θ is the diffraction angle or Bragg angle (Fig. 2.7). The angle between the direction of the incident and diffracted beam is equal to 2θ. Bragg's law defines the conditions under which diffraction occurs, and gives the position of a diffracted beam, without any reference to its intensity.

If a crystal in a beam of radiation is rotated, each set of planes will, in its turn, diffract the radiation when the value of $\sin\theta$ becomes appropriate. This is the principle by which diffraction data is collected for the whole of the crystal. The arrangement of the diffracted beams, when taken together, is the diffraction pattern of the crystal.

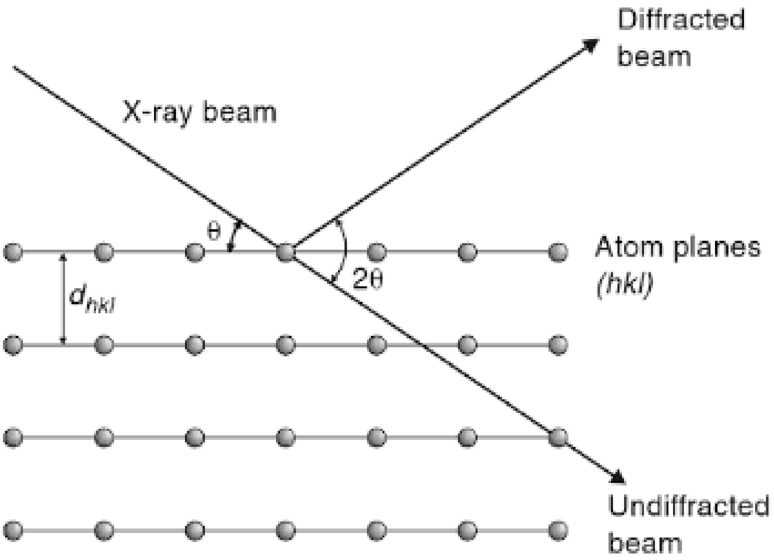

Fig. 2.7 The geometry of Bragg's law for the diffraction of X-rays from a set of crystal planes, (*hkl*), with interplanar spacing d_{hkl} [131]

The Bragg equation, applied to diffraction data, results in a list of d_{hkl} values for a compound. It is possible, by putting these to data sets together, to determine the size of the unit cell of the material producing the diffraction pattern. [131]

There are mainly two kinds of diffraction techniques: powder X-ray diffraction and single crystal X-ray diffraction, between which the powder one is the most widely used. Powder X-ray diffraction operates under the assumption that the sample is randomly arranged. Therefore, a statistically significant number of each plane of the crystal structure will be in the proper orientation to diffract the X-rays. Therefore, each plane will be represented in the signal.

The XRD pattern can be acquired with a diffractometer consisting of three basic elements: an X-ray tube, a sample holder, and an X-ray detector (Fig. 2.8). X-rays are generated in a cathode ray tube by heating a filament to produce electrons, accelerating the electrons toward a target by applying a voltage, and bombarding the target material with electrons. When electrons have sufficient energy to dislodge inner shell electrons of the target material, characteristic X-ray spectra are produced. These spectra consist of several components, the most common being K_α and K_β. Copper is the most common target material with CuKα radiation = 1.5418Å.

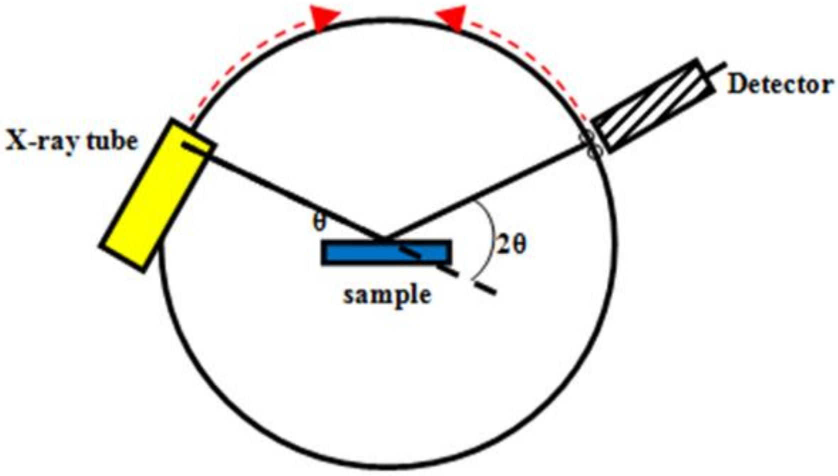

Fig. 2.8 The schematic diagram of X-ray diffractometers

When the X-rays are directed onto the sample, with the rotation of the sample and detector, the intensity of the reflected X-rays is recorded. When the geometry of the incident X-rays impinging the sample satisfies the Bragg Equation, constructive interference occurs and a peak in intensity occurs. A detector records and processes this X-ray signal and converts the signal to a count rate. The geometry of an X-ray diffractometer is such that the sample rotates in the path of the collimated X-ray beam at an angle θ while the X-ray detector is mounted on an arm to collect the diffracted X-rays and rotates at an angle of 2θ. For typical powder patterns, data is collected at 2θ from ~5° to 70°.

2.2.2 Reflectance spectroscopy

Different surface features reflect or absorb the sun's electromagnetic radiation in different ways. The reflectance properties of an object depend on the material and its physical and chemical state, the surface roughness as well as the geometric circumstances (e.g. incidence angle of the sunlight). The reflectance of a material also varies with the wavelength of the electromagnetic energy. These differences in reflectance make it possible to identify different earth surface features or materials by analyzing their spectral reflectance signatures. Spectral reflectance curves graph the spectral reflectance of objects as a function of wavelengths.

Reflectance spectroscopy takes advantages of the scattering of incident energy off a solid surface, so instead of measuring the light intensity before and after passing through a specimen, one measure the amount of light reflected off the sample surface with the aid of a suitably modified instrumental system.

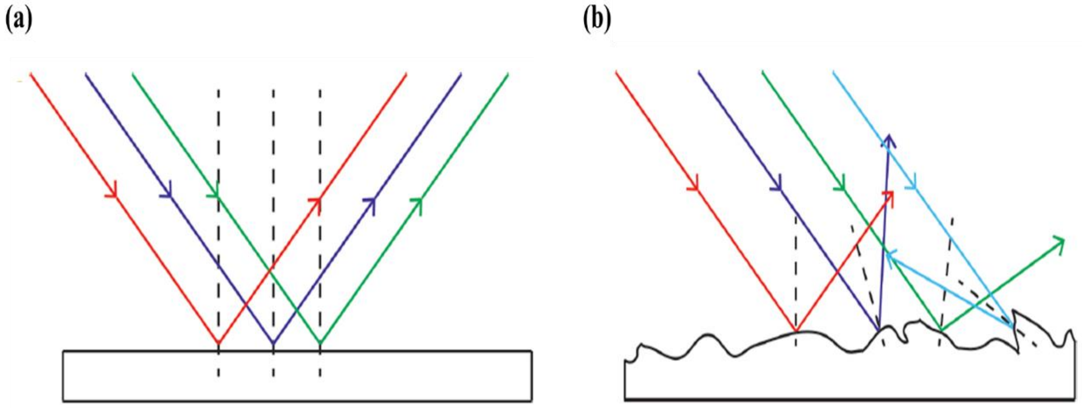

Fig. 2.9 (a) Specular reflection; (b) Diffuse reflection [132]

Generally, there are two different kinds of reflectance: specular reflectance and diffuse reflectance (Fig. 2.9). Diffuse reflectance is associated with the radiation, which penetrates into the particles to some extent and then emerges from the bulk solid. This light will exhibit spectral characteristics, which are modified from those of the incident beam by the wavelength-specific attenuation that took place as a result of induced electronic transitions caused by light absorption at the boundaries of the component particles. The attenuation of the diffuse part of the reflectance caused by absorption can be expressed by the Bouguer-Lambert law:

$$\mathrm{I} = I_0 e^{-\varepsilon d} \tag{2.3}$$

Where I is the intensity of diffusively reflected light, I_0 is the incident light intensity, ε is the molar extinction coefficient, and d is the mean thickness of penetration.

Equation 2.3 indicates that the distribution of wavelengths leaving the solid will be modified from that of the incident light by any wavelength-selective absorption within the sample. The electromagnetic radiation, which is diffusely reflected, must penetrate the sample before returning to the surface through multiple scattering.

The basic requirements for a diffuse reflectance spectrometer are a light source and a monochromator (to obtain monochromatic radiation), an integrating sphere, and a detection and recording system. The incident energy from the source does not need to be diffuse in itself, and good results are obtained using direct irradiation of the sample. The light is rendered monochromatic by either a monochromator or filter arrangement, split, and allowed to fall on both the standard and sample faces. The light diffusely reflected by the reference and the sample are collected by the internal reflections of the sphere, and the intensity is ultimately measured by the detector.

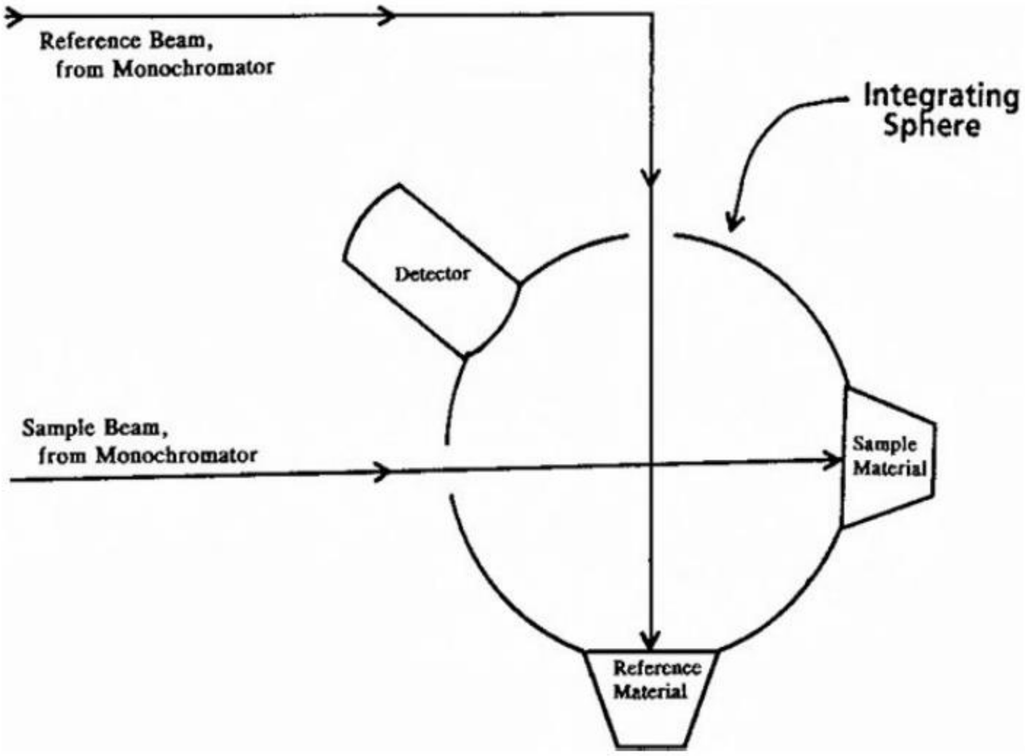

Fig. 2.10 Schematic diagram of the integrating sphere portion of a diffuse reflectance spectrometer, illustrating the key elements of the optical train. [133]

Fig. 2.10 illustrates the design of integrating sphere, which is the essential and unique part of a diffuse reflectance spectrometer. The inner surfaces of the sphere are coated with highly reflective materials to minimize absorption of the diffuse reflectance. [133]

2.2.3 Photoluminescence spectroscopy

Photoluminescence (abbreviated as PL) is light emission from any form of matter after the absorption of photons (electromagnetic radiation). It is initiated by photoexcitation (i.e. photons that excite electrons to a higher energy level in an atom). In essence, light is directed onto a sample, where it is absorbed and where the photo-excitation process can occur. The photo-excitation causes the material to jump to a higher electronic state, and will then release energy, (photons) as it relaxes and returns to back to a lower energy level. The emission of light, or luminescence through this process is photoluminescence, PL.

In this work, time-resolved photoluminescence technique is applied. Time Resolved Photoluminescence (TRPL) is an experimental technique that provides the spectral and temporal evolution of the emission of a sample following its illumination by a short pulse of light. More precisely, the short pulse of light generates electron-hole pairs that decay to lower energy levels of the sample. These electron-hole pairs can subsequently recombine and emit light. The emitted light is composed of a set of wavelengths corresponding to transition energies of the sample and, as a result, the measurement of the optical spectrum as a function of time provides a means to measure the transition energies and their lifetimes. Since these decay times are on the order of picoseconds or nanoseconds, and the intensity of light emitted can be very weak, a conventional spectrum analyser cannot provide the resolution required. Instead, it is necessary to use a device known as a streak camera.

The streak camera is an ultra-high-speed detector which captures light emission phenomena occurring in extremely short time periods. The operating principle is shown in Fig. 2.11. The light pulse to be measured is projected onto the slit and is focused by a lens into an optical image on the photocathode, able to cover a wavelength range between 300 nm and 1500 nm. Here, the photons are converted into a stream of electrons proportional to the intensity of the incident light. As the electron stream created from the light pulse passes between a pair of sweep electrodes, a time-varying voltage is applied to the electrodes, resulting in a high-speed sweep. This means that the early part of the pulse is deflected less than the later part of the pulse, so that different parts of the pulse strike the micro channel plate (MCP) at different positions. Thus the temporal structure of the pulse is converted into a spatial distribution, or ‘streak’, pattern. As the electrons pass the MCP, they are multiplied several thousands of times and are then bombarded against the phosphor screen, where they are converted back into light. The fluorescence image corresponding to the early part of the incident light pulse is positioned at the top of the phosphor screen, with later parts positioned in descending order; in other words, the axis in the perpendicular direction on the phosphor screen serves as the temporal axis. The brightness of the fluorescence image is proportional to the intensity of the corresponding incident light pulses and the position in the horizontal direction on the phosphor screen corresponds to the wavelength of the incident light. [134]

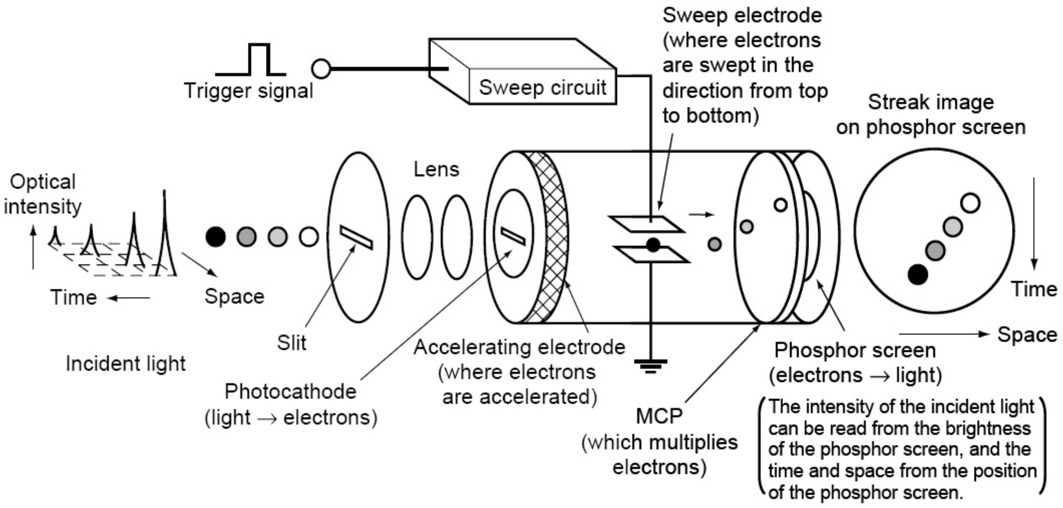

(The intensity of the incident light can be read from the brightness of the phosphor screen, and the time and space from the position of the phosphor screen.)

Fig. 2.11 Schematic diagram of a streak camera [134]

The PL intensity is proportional to the rate of radiative recombination. For direct bandgap recombination, the radiative recombination rate per unit volume, R_{rad}, is given by

$$R_{rad}(t) = B[p(r,t)n(r,t) - p_0(r)n_0(r)] \tag{2.4}$$

where B is the radiative recombination coefficient and p_0 and n_0 are the equilibrium hole and electron concentrations, respectively. For p-type material, $p_0 >> n_0$ and substitution of $p = p_0 + \Delta p$ and $n = n_0 + \Delta n$ into Eq. 2.5 gives

$$R_{rad}(t) = B[p_0(r) + \Delta p(r,t)]\Delta n(r,t) \tag{2.5}$$

where Δp and Δn are the excess hole and electron concentrations, respectively. In low-injection conditions, $\Delta p << p_o$, Eq. 2.5 indicates that the rate of radiative recombination is linearly proportional to the number of minority carriers. So, the PL decay tracks minority carrier recombination, even if this recombination is due primarily to nonradiative processes such as Shockley-Read-Hall (SRH) or Auger recombination. In high injection conditions, $\Delta p >> p_o$ and the PL intensity is proportional to p^2. Although more complicated in form, the PL intensity still tracks the decay of excess carriers.

Minority carriers can decay via midgap states created by surface states, grain boundaries, structural defects, point defects, and impurities, or by radiative recombination, Auger recombination, and other processes. By varying sample temperature, sample dimensions, and injection levels, and conducting ancillary experiments, we can use Time Resolved Photoluminescence (TRPL) to help determine which recombination processes are dominant. However, the technique can rarely pinpoint the source of SRH type recombination. [135]

Fig. 2.12 [136] represents a general set-up of time-resolved photoluminescence. The equipment will be discussed in detail in Chapter 3.

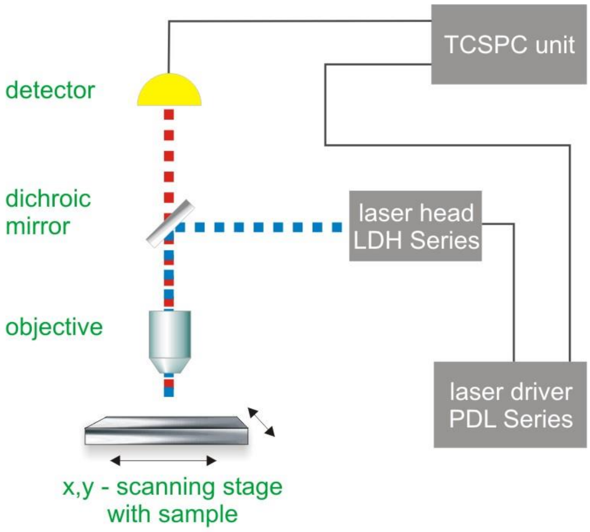

Fig. 2.12 General set-up for time-resolved photoluminescence [136]

Chapter3 Fabrication and characterization of organo-germanium bromide perovskite

In this chapter, we prepared 3D $CH_3NH_3GeBr_3$ and 2D germanium bromide perovskite $(CH_3(CH_2)_3NH_3)_2(CH_3NH_3)_{n-1}Ge_nBr_{3n+1}$ (n = 1, 2, 3) series. Then we did several measurements by powder x-ray diffraction (XRD), uv-vis-NIR spectroscopy and time-resolved photoluminescence spectroscopy, further investigating their crystal structures optoelectronic properties.

3.1 Experimental section

3.1.1 Starting materials

Methylammonium bromide (CH_3NH_3Br) was purchased from DyeSol. Hypophosphorous acid (H_3PO_2), hydrobromic acid (HBr), germanium dioxide (GeO_2) and n-butylamine ($CH_3(CH_2)_3NH_2$) were all purchased from Sigma-Aldrich.

3.1.2 Synthesis

All operations were carried out under high purity nitrogen.

$MAGeBr_3$ (n = ∞). A two-neck flask was charged with a mixture of 48% w/w aqueous HBr (3.0mL, 55.2mmol) and 50% w/w aqueous H_3PO_2 (2.0mL, 18.2mmol). GeO_2 powder (209mg, 2mmol) was dissolved in the mixture by heating the flask to 140°C in an oil bath, under constant magnetic stirring for about 20min, which formed a bright pale yellow solution. Subsequently, a stoichiometric amount of solid CH_3NH_3Br (224mg, 2mmol) was added to the hot solution and dissolved then. 20min later, the stirring was discontinued, and the solution was left to cool down to room temperature. Upon cooling, lemon yellow, granular crystals were precipitated. After being kept in the solution overnight, the crystals were collected by suction filtration and dried under reduced pressure.

$(BA)_2GeBr_4$ (n = 1). A two-neck flask was charged with a mixture of 48% w/w aqueous HBr (2.0mL, 36.8mmol) and 50% w/w aqueous H_3PO_2 (3.0mL, 27.3mmol). GeO_2 powder (209mg, 2mmol) was dissolved in the mixture by heating the flask to 140°C in an oil bath, under constant magnetic stirring for about 20min, which formed a bright pale yellow solution. In a separate flask, $n-CH_3(CH_2)_3NH_2$ (197μL, 2mmol) was neutralized with 48% w/w aqueous HBr (2mL, 36.8mmol) in an ice bath, resulting an transparent solution. The $n-CH_3(CH_2)_3NH_3Br$ solution was then added dropwise into the two-neck flask. After being gradually heated to about 160°C in 30min, the stirring was discontinued, and the solution was left to cool down to freezing temperature, resulting in the precipitation of white lamellar crystals. After being kept in the solution overnight, the crystals were collected by suction filtration and dried under reduced pressure.

$(BA)_2(MA)\mathrm{Ge}_2Br_7$ (n = 2) . A two-neck flask was charged with a mixture of 48% w/w aqueous HBr (2.0mL, 36.8mmol) and 50% w/w aqueous H_3PO_2 (3.0mL, 27.3mmol). GeO_2 powder (209mg, 2mmol) was dissolved in the mixture by heating the flask to 140°C in an oil bath, under constant magnetic stirring for about 20min, which formed a bright pale yellow solution. Subsequently, a stoichiometric amount of solid CH_3NH_3Br (112mg, 1mmol) was added to the hot solution and dissolved then. In a separate flask, $n-CH_3(CH_2)_3NH_2$ (246μL, 2.5mmol) was neutralized with 48% w/w aqueous HBr (2mL, 36.8mmol) in an ice bath, resulting an transparent solution. The $n-CH_3(CH_2)_3NH_3Br$ solution was then added dropwise into the two-neck flask. After being gradually heated to about 160°C in 30min, the stirring was discontinued, and the solution was left to cool down to freezing temperature, resulting in the precipitation of light yellow lamellar crystals on the surface and granular ones inside. After being kept in the solution overnight, the crystals were collected by suction filtration and dried under reduced pressure.

$(BA)_2(\mathrm{MA})_2\mathrm{Ge}_3Br_{10}$ (n = 3) . A two-neck flask was charged with a mixture of 48% w/w aqueous HBr (2.0mL, 36.8mmol) and 50% w/w aqueous H_3PO_2 (3.0mL, 27.3mmol). GeO_2 powder (314mg, 3mmol) was dissolved in the mixture by heating the flask to 140°C in an oil bath, under constant magnetic stirring for about 20min, which formed a bright pale yellow solution. Subsequently, a stoichiometric amount of solid CH_3NH_3Br (224mg, 2mmol) was added to the hot solution and dissolved then. In a separate flask, $n-CH_3(CH_2)_3NH_2$ (295μL, 3mmol) was neutralized with 48% w/w aqueous HBr (2mL, 36.8mmol) in an ice bath, resulting an transparent solution. The $n-CH_3(CH_2)_3NH_3Br$ solution was then added dropwise into the two-neck flask.

After being gradually heated to about 160°C in 30min, the stirring was discontinued, and the solution was left to cool down to freezing temperature, resulting in the precipitation of light yellow lamellar crystals on the surface and granular ones inside. After being kept in the solution overnight, the crystals were collected by suction filtration and dried under reduced pressure.

3.1.3 Characterization

3.1.3.1 Powder X-ray diffraction (XRD)

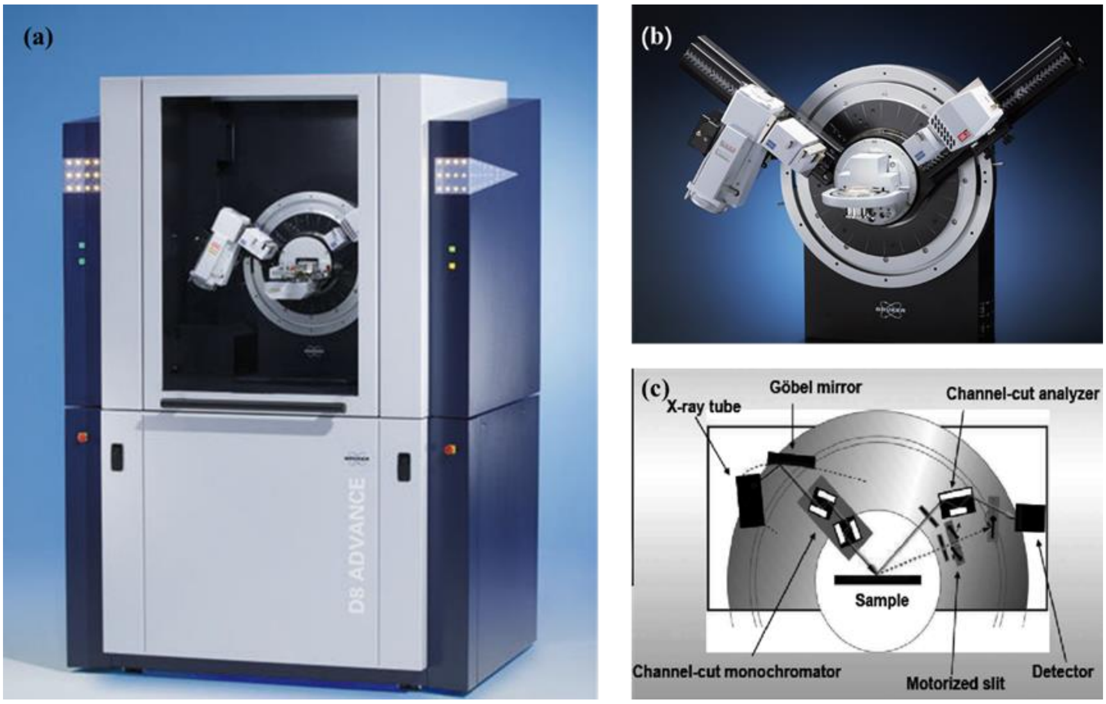

Fig.3.1 (a) Bruker D8-Discover diffractometer and its (b) main components; (c) schematic diagram of the main components

Powder X-ray diffraction measurements were performed at room temperature with a Bruker D8-Discover diffractometer (Bragg-Brentano geometry) for crystals with parallel beam geometry and Cu Ka wavelength (λ=1.5418Å) operated at 40 kV and 40 mA using a step size of 0.05° and a time per step of 1 s (Fig. 3.1). The powder samples were placed on a Bruker silicon sample holder. For 3D $CH_3NH_3GeBr_3$, the Bragg angle ranges from 10° to 50°, whereas for 2D $(CH_3(CH_2)_3NH_3)_2(CH_3NH_3)_{n-1}Ge_nBr_{3n+1}$, n = 1 compound was measured from 5° to 45° and n = 2 and 3 compounds were measured from 2° to 40°. Then the data were refined by TOPAS and the crystal structures were solved by VESTA.

3.1.3.2 Optical diffuse reflectance spectroscopy

The reflectance measurements were performed at room temperature using a Cary 5000 UV-Vis-NIR spectrophotometer (Fig. 3.2(a)) with superb photometric performance in the 175-3300 nm range. UV-Vis-NIR spectra were, in general, acquired in the region 250-2500 nm using appropriate baseline correction (Zero/baseline correction). Indicative instrumental parameters were as follows: 2 nm SBW, 0.1 s SAT, 1 nm data interval (UVVis) and Energy 3, 0.2 s SAT, 3 nm data interval (NIR); Here, using a PbSmart detector, the Cary 5000 extends its NIR range to 3300 nm.

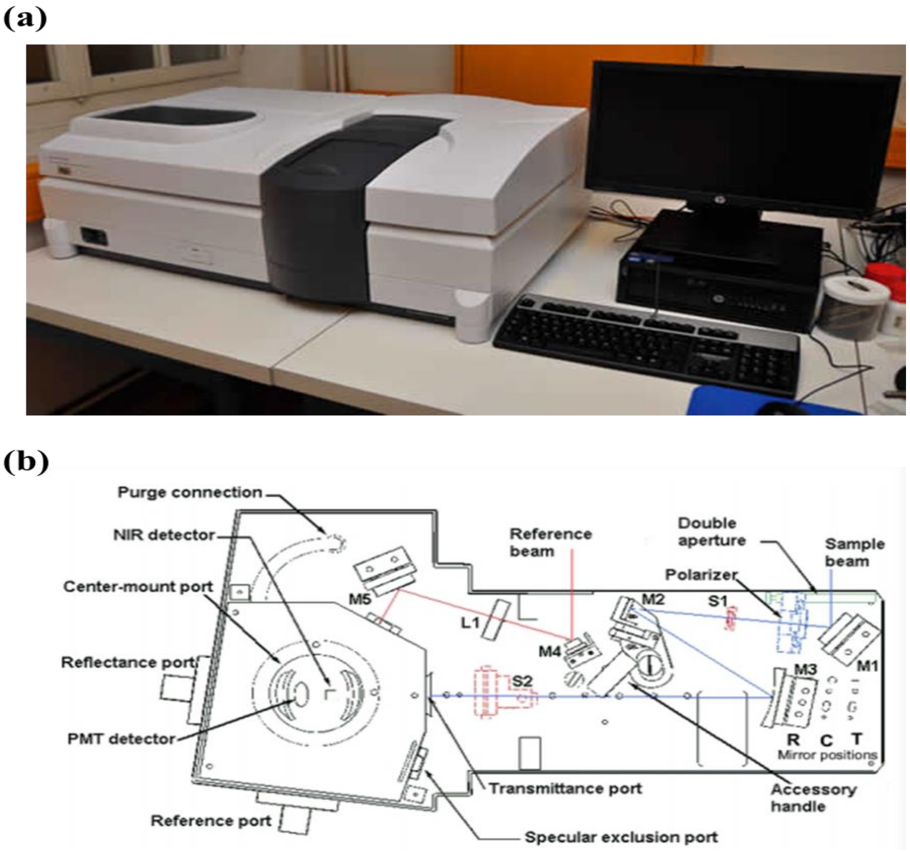

Fig. 3.2 (a) Cary 5000 UV-Vis-NIR spectrophotometer; (b) A schematic view of the Diffuse reflectance accessories (DRAs)

To perform these types of reflectance measurements a high-performance UV-Vis-NIR spectrophotometer equipped with diffuse reflectance accessories is required. Fig. 3.2(b) illustrates a schematic view of the diffuse reflectance accessories. The optics chamber contains the transfer optics that direct the spectrophotometer beams to their final destinations. The integrating sphere collects and measures the radiation transmitted or reflected from the sample surface. A removable cover fits over the DRA to provide a light-tight operating environment. The sample reflectance and reference ports each are fitted with a separate magnetic port cover. The purposes of the covers are to reduce the potential for stray light when the accessory is in use.

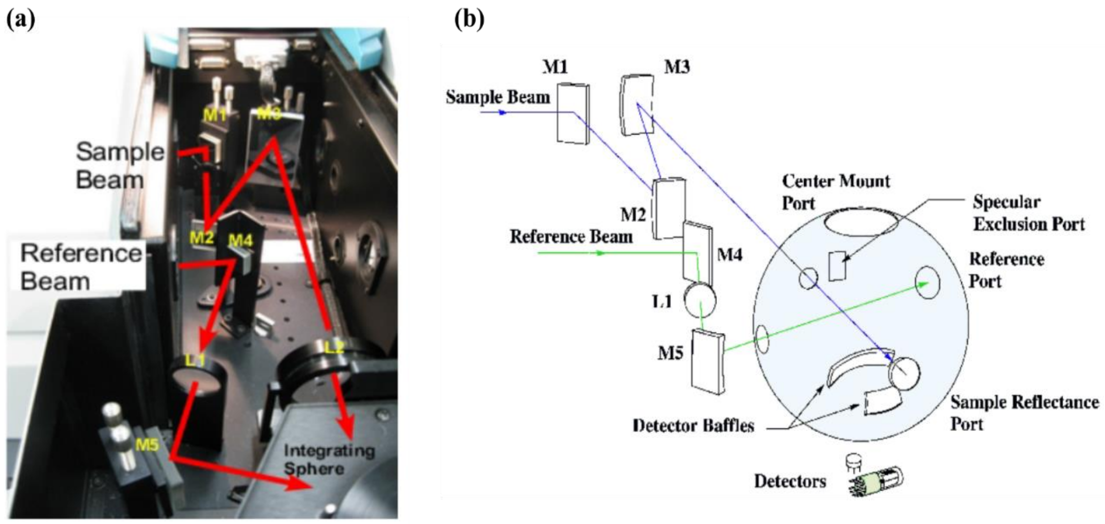

Fig. 3.3 (a) Photo of diffuse reflectance accessory with beam path; (b) A schematic diagram of the optical design of the diffuse reflectance accessory

Beam paths within the accessory are illustrated in Fig. 3.3. Light entering the accessory is directed to one of two entrance ports on the sphere: the reference beam and sample beam entrance ports.

For the measurement, the samples were directly placed in the sample holder, covering the transparent bottom evenly. The wavelength range was elected from 300nm to 900nm. Before starting the reflection measurement, a Zero/Baseline correction is necessary in order to correct the error caused by halo-effect, which is due to the strikes of small-angle scattering on the wall of the integrating sphere near the reflectance sample port.

3.1.3.3 Time-resolved photoluminescence spectroscopy

The samples were prepared on transparent glass substrates where the crystals were attached on. Then the substrates were inserted into a square sample holder which was vacuumized later. In time-resolved photoluminescence experiments, samples were excited with a regenerative amplified laser (Coherent Libra) delivering 130-fs-long pulses at a repetition rate of 1 KHz. Photoluminescence was dispersed with a grating spectrometer (Princeton Instruments Acton SpectraPro 2300i equipped with a 50 gr/mm grating blazed at 600 nm), dispersed and detected by a streak camera (Hamamatsu).

The laser source for the time-resolved photoluminescence setup is a Ti:sapphire passively mode-locked femtosecond laser, emitting at 780 nm in wavelength. Ti:sapphire lasers (also known as Ti:Al_2O_3 lasers, titanium-sapphire lasers, or Ti:sapphs), based on a crystal of sapphire (Al_2O_3) that is doped with titanium ions, are tunable lasers which emit red and near-infrared light in the range from 650 to 1100 nanometers.[137] The maximum gain is around 800 nm, which is the wavelength corresponding to the carrier frequency of Ti:Sapphire pulses.

Mode-locked oscillator, the type of Ti:sapphire laser we used in our measurement, generate ultrashort pulses with a typical duration between a few picoseconds and 10 femtoseconds, in special cases even around 5 femtoseconds. The pulse repetition frequency is in most cases around 70 to 90 MHz. Ti:sapphire oscillators are normally pumped with a continuous-wave laser beam from an argon or frequency-doubled Nd:YVO4 laser. Typically, such an oscillator has an average output power of 0.4 to 2.5 watts.

To obtain higher pulse energies, a technique called chirped pulse amplification is employed. The laser implementing this technique is called regenerative amplifier. The amplification sequence is illustrated in fig. 3.4. [138]

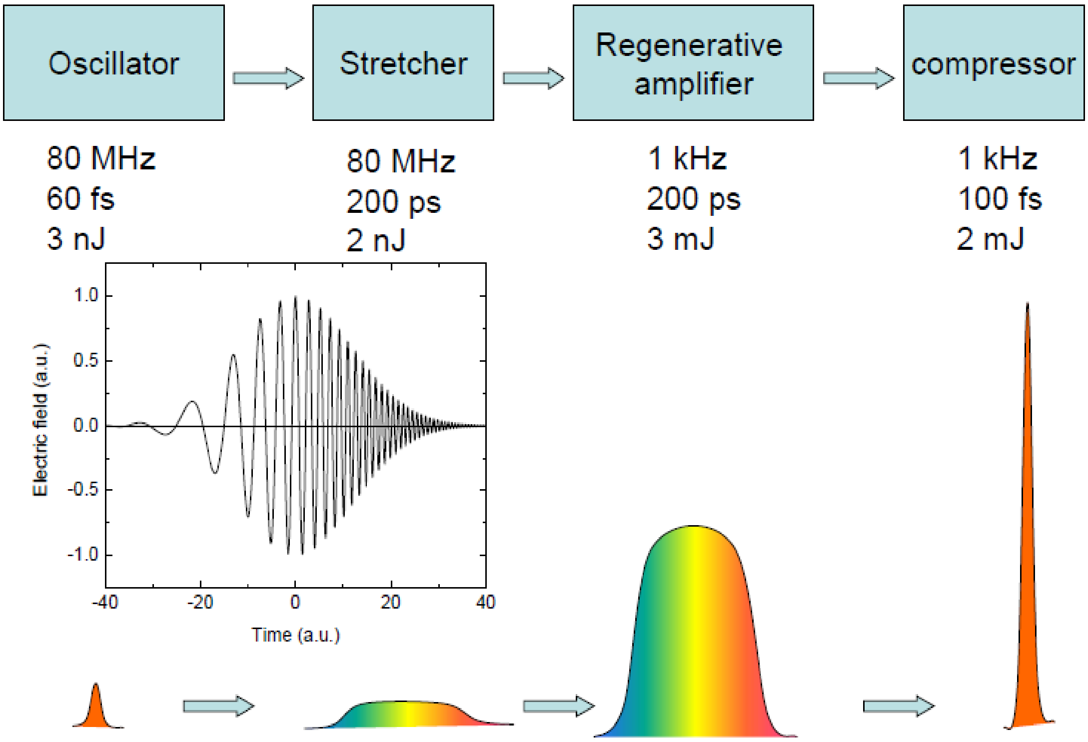

Fig. 3.4 Operation principle of chirped pulse regenerative amplifier. Weak pulses are stretched in time, one out ofb~80000 pulses is injected into the amplifier cavity, amplified and compressed in time again. [138]

The photoluminescence signal provides a lot of information on the electronic and optical properties of the perovskites. According to the spectral analysis, we can derive the band gap and life time, also we can investigate the different excitonic states and trap states which correspond to significant shifts in wavelength. In addition, as the decay time of the light signal is different for different excitonic states and trap states, we can investigate the dynamics of the charges

The experimental procedure is shown in Fig. 3.5 [139]. A train of laser pulses from the regenerative amplified laser is sent by means of an optic that allows an appropriate focusing on the sample. Each pulse is absorbed in a very short time and provides energy and creates an excited state in the sample. Photoluminescence emitted by the sample between one pulse and the next is collected by an appropriate optical configuration and acquired by the detection system. The detection system is composed of a spectrometer coupled with a streak camera, the spectrometer spectrally resolves the optical signal while the streak camera temporally resolves the optical signal. As a final result is obtained a spectrogram with the spectral and temporal properties of the sample. [140]

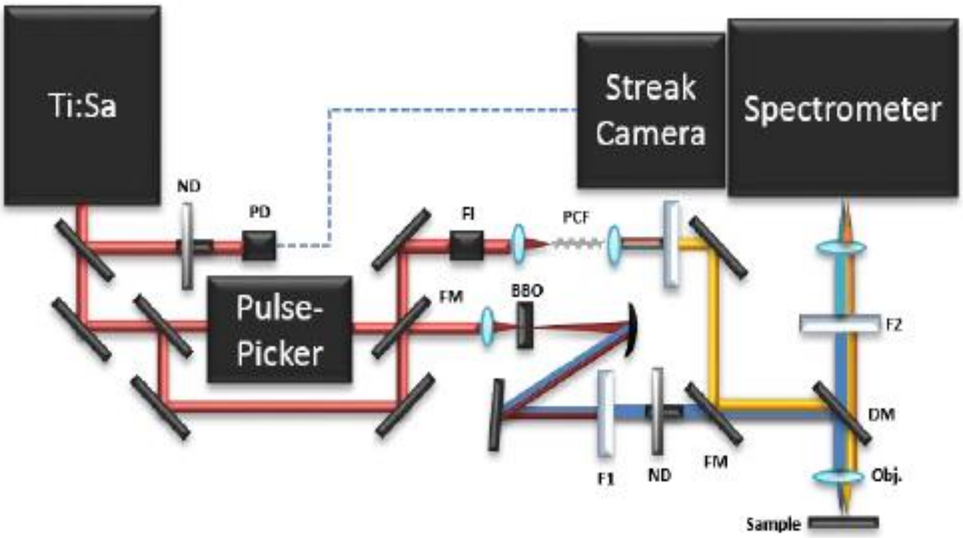

Fig. 3.5 Schematic diagram of the time-resolved photoluminescence setup[139]

3.2 Results and discussion

3.2.1 Synthesis

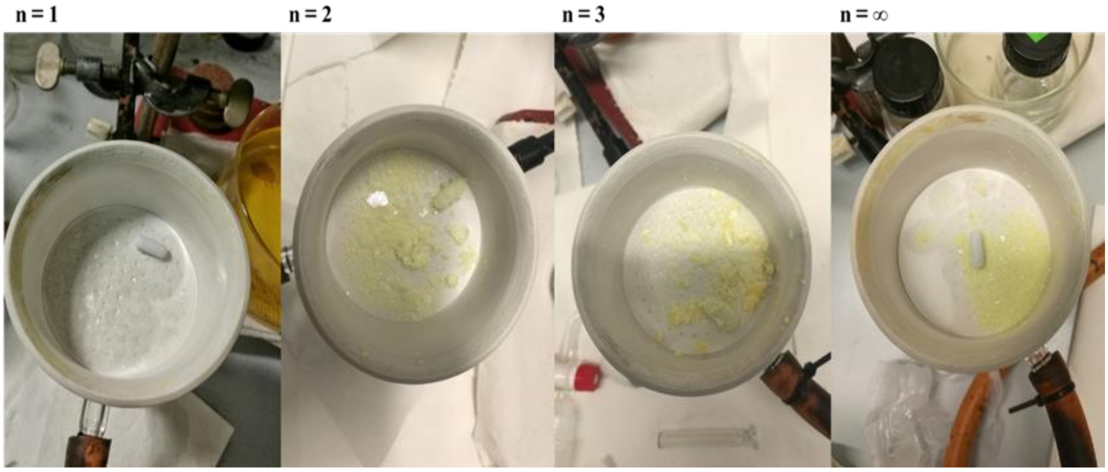

Fig. 3.6 Photographs of the $(CH_3(CH_2)_3NH_3)_2(CH_3NH_3)_{n-1}Ge_nBr_{3n+1}$ perovskite crystals, among which n = ∞ represents 3D $CH_3NH_3GeBr_3$

The three-dimensional $CH_3NH_3GeBr_3$ perovskite could be prepared from a solution containing stoichiometric amount of CH_3NH_3Br (MABr) and $GeBr_2$, while the 2D $(CH_3(CH_2)_3NH_3)_2(CH_3NH_3)_{n-1}Ge_nBr_{3n+1}$ series of perovskite compounds (n = 1, 2,), could react with $GeBr_2$, CH_3NH_3Br (MABr) and n-butylamine (BA) by stoichiometry, among which, though, only the first two was added with a n: (n-1) molar ratio and the amount of organic spacer cation, BA^+ was excessive. Here, hypophosphorous acid (H_3PO_2) played the role of reducing agent to generate and stabilize the Ge^{2+} anions, hidering them from being oxidized to Ge^{4+} anions again. All the straightforward and reproducible fabrications would lead to the formation of clear, pale yellow and homogeneous solutions after heating and stirring for some time and produce precipitation of crystals in different colors upon cooling down to room temperature (3D) or freezing point (2D) (Fig. 3.6). Fig. 3.6 shows the shapes and colors of the crystals during suction filtration. It is quite obvious that color deepened as the perovskite layers increased, from almost achromatic (n = 1) to yellow (n = ∞). It is noteworthy that after being completely dried, the colors of all the compounds further darkened, with 3D $CH_3NH_3GeBr_3$ crystals turning into light yellow. Additionally, from hydrobromic acid mother liquors, the 2D $(CH_3(CH_2)_3NH_3)_2(CH_3NH_3)_{n-1}Ge_nBr_{3n+1}$ perovskite compounds (n = 1, 2) originally crystallized in irregularly lamellar form, which was too fragile to be kept during suction filtration and mostly broke then.

Through a series of experiments, we discover that the amount of n-butylamine (BA) is one of the key factors that decide the purity of the reaction products. For n = 1 reaction, n-butylamine (BA) was used as the limiting reactant, which was about half of the amount of germanium, and the product was pure $(CH_3(CH_2)_3NH_3)_2GeBr_4$. However, for n = 2 reaction, neither limited nor stoichiometric amount of n-butylamine (BA) would contribute to the pure product of $(CH_3(CH_2)_3NH_3)_2(CH_3NH_3)Ge_2Br_7$. On the contrary, nearly pure n = 2 compound was obtained from solution containing excessive n-butylamine (BA). Unfortunately, the single product stops at the n = 3 reaction, from which only a mixture of 3D $CH_3NH_3GeBr_3$ and 2D $(CH_3(CH_2)_3NH_3)_2(CH_3NH_3)_2Ge_3Br_{10}$ (n = 3) was achieved. Thus, it is rather important to control the stoichiometry of n-butylamine (BA) to get single n-number products.

3.2.2 Crystal structure description

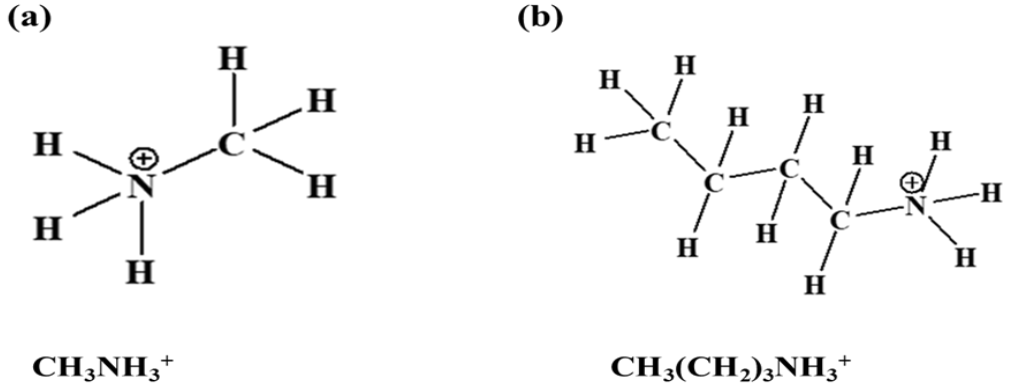

Fig. 3.7 Molecular formula of (a) A cation: Methylammonium (MA) and (b) R-NH_3 cation: n-butylammonium (BA)

Fig. 3.7 shows the molecular structural formula of the A cation— Methylammonium (MA) and the spacer R-NH_3 cation— n-butylammonium (BA). The crystal structures of the three-dimensional $CH_3NH_3GeBr_3$ and the two-dimensional $(CH_3(CH_2)_3NH_3)_2GeBr_4$ (n = 1) compounds are shown in Figure 3.8, and the comparison of selected crystallographic information between the two is presented in Table 5, 6 and 7. The three-dimensional $CH_3NH_3GeBr_3$ constructs its framework through single Ge-Br-Ge bridge, forming corner-sharing $[GeBr_6]^{4-}$ octahedra. $CH_3NH_3GeBr_3$ crystallizes in the polar R3m space group of a trigonal crystal system, with lattice parameters a = b = c = 5.8188Å and α=β=γ= 88.5319°, confirming a slight trigonal distortion. And the $CH_3NH_3^+$ cation, which owns an inherent C_{3v} symmetry and rotate itself to adjust the 4-fold symmetry axis, would further enhance the distortion. [141] According to the bond length, the six Ge-Br bonds could be divided into two even groups, one of which has a small parameter of about 2.68 Å, the other has a comparatively larger bond length of 3.14 Å. Compared with the three-dimensional $CH_3NH_3GeI_3$ that has been fabricated before [141], as the iodide monovalent ion has a larger diameter than the bromide anion, thus demonstrates lower non-metallicity and lower bond energy, leading to a larger unit cell volume, greater lattice distortion and longer bond distances of $CH_3NH_3GeI_3$.

Table 5 Crystal data for 2D $(CH_3(CH_2)_3NH_3)_2GeBr_4$ compared with the 3D $CH_3NH_3GeBr_3$

Formula	**$(CH_3(CH_2)_3NH_3)_2GeBr_4$**	**$CH_3NH_3GeBr_3$**
Formula weight	466.40	344.42
Crystal system	Monoclinic	Trigonal
Space group	P21/c	R3m
Color	Pale yellow	Bright yellow
Unit cell length (Å)	a = 8.4581	a = 5.8188
	b = 8.3703	b = 5.8188
	c = 28.5050	c = 5.8188
Unit cell angles	α = 90°	α = 88.5319°
	β = 98.9070°	β = 88.5319°
	γ = 90°	γ = 88.5319°
Volume ($Å^3$)	1993.7	196.8
Z	4	3
Density(calc), g/cm^3	2.628	2.963

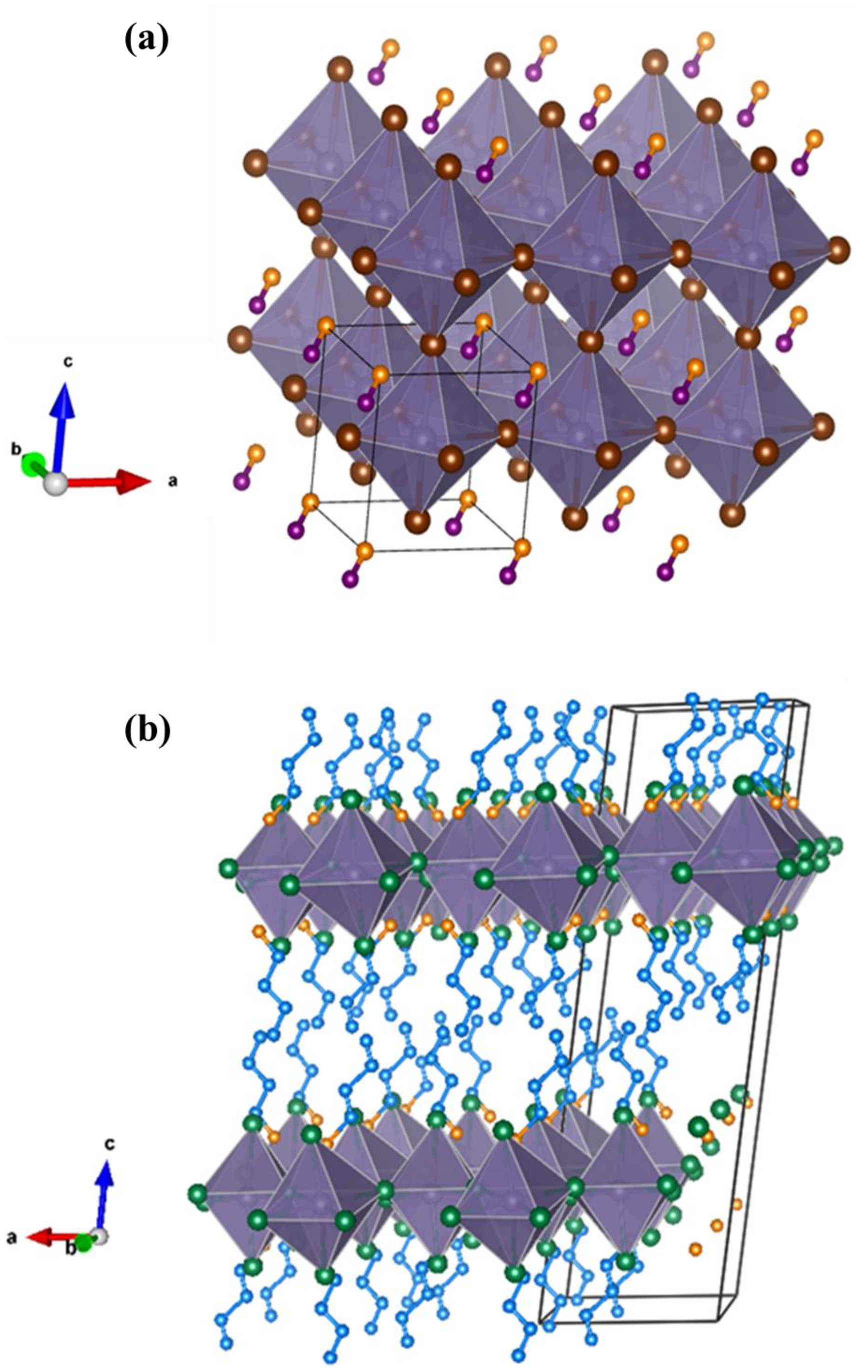

Fig. 3.8 Crystal structures of the $(CH_3(CH_2)_3NH_3)_2(CH_3NH_3)_{n-1}Ge_nBr_{3n+1}$ perovskite compounds. (a) The unit cell of $CH_3NH_3GeBr_3$ (n = ∞). Pale purple (in the center of the Octahedra), Brown, violet, and orange spheres represent germanium (Ge), bromide (Br), nitrogen (N) and carbon (C). (b) The unit cell of $(CH_3(CH_2)_3NH_3)_2GeBr_4$ (n = 1), respectively. Pale purple (in the center of the Octahedra), green, orange, and blue spheres represent germanium (Ge), bromide (Br), nitrogen (N) and carbon (C), respectively.

The layered two-dimensional $(CH_3(CH_2)_3NH_3)_2GeBr_4$ compound crystallizes in the P21/c space group of a monoclinic crystal system, which is regarded as a low symmetry crystal system due to the lack of higher-ordered axis. The corresponding unit cell length and angle are a = 8.4581 Å, b = 8.3703 Å, c = 28.5050 Å and $\alpha = 90°$, $\beta = 98.9070°$, $\gamma = 90°$, respectively.

Table 6 Positional parameters for 3D $CH_3NH_3GeBr_3$

atom	position	x	y	z
Ge	1a	0.48718	0.48718	0.48718
Br	3b	0.50718	0.50718	0.50718
N	1a	0.87900	0.87900	0.87900
C	1a	0.00200	0.00200	0.00200

The layered crystal structure is presented in Fig. 3.8 (b). The organic $CH_3(CH_2)_3NH_3^+$ cations, acting as a spacer between the perovskite layers, were inseted between the germanium bromide planes which were constituted of $[GeBr_6]^{4-}$ octahedral. And in the directions of a-axis and b-axis, the octahedral share corners to form $GeBr_4$ sheets. The layered structure of $(CH_3(CH_2)_3NH_3)_2GeBr_4$ can be considered to be a derivative of the three-dimensional $CH_3NH_3GeBr_3$ perovskite structure by slicing the three-dimensional frameworks into two-dimensional slabs containing a single layer of perovskite structure, and replacing all the methylammonium cations with butylammonium.[142][143][144][145][146] The layered structure could also be regarded as an analogue to that of La_2CuO_4, via replacing the CuO_2 sheets by the inorganic sheets of $GeBr_2$ and replacing the inorganic La_2O_2 layers by the organic $(CH_3(CH_2)_3NH_3)_2Br_2$ layers.[142][147] In $(CH_3(CH_2)_3NH_3)_2GeBr_4$ structure, being offered a lone pair of electrons by bromide, the germanium cation is in a negative divalent state. As a result, the coordination symmetry around is lowered and compound will demonstrate evident stereochemical activities [142].

Similar to three-dimensional $CH_3NH_3GeBr_3$, the six Ge-Br bonds in $[GeBr_6]^{4-}$ octahedra also split in three short ones and three long ones, ranging from 2.99Å to 3.27Å. The bond angles of Br-Ge-Br show a notable deviation from 90° both in 2D $(CH_3(CH_2)_3NH_3)_2GeBr_4$ and 3D $CH_3NH_3GeBr_3$ compounds, between which, the octahedra in layered perovskite tilt along the crystallographic ab planes with Ge-Br-Ge angle of 162.8°, proving a more severe distortion than that of the 3D germanium compound, whose bond angle is 173.4°. This tilt also produces a slight corrugation to the organic sheets. The organic long chains spread out of the ab planes, embedded into the space between perovskite layers, with the N (1) and N (2) nitrogen atoms located inside the plane along c-axis. In addition, being one of the $(CH_3(CH_2)_3NH_3)_2MBr_4$ (M=Cl, Br, I) analogues, $(CH_3(CH_2)_3NH_3)_2PbBr_4$ has a Pb-Br-Pb bond angle of about 154.8 ° [152], smaller than that of $(CH_3(CH_2)_3NH_3)_2GeBr_4$, representing larger electronegativity in lead bromide perovskite than in the germanium one and further leading to narrower bandgaps of $(CH_3(CH_2)_3NH_3)_2PbBr_4$. Note that no matter in the two-dimensional structure or in the three-dimensional one, the corner-connected octahedra is always supposed to tilt to some extent to keep the structural integrity.

While the tilted $[GeBr_6]^{4-}$ octahedra layers are arranged along the ab plane, the organic layers composed of spacer cations $CH_3(CH_2)_3NH_3^+$, interrupting the extension in the third dimension (the c-axis). As can be seen from table 5, the insertion of the organic sheets leads to a comparably larger lattice parameter (28.5050Å) in the c-axis direction than the 3D compound (5.8188Å), along with an increase of bandgap.

The $(CH_3(CH_2)_3NH_3)_2(CH_3NH_3)_{n-1}Ge_nBr_{3n+1}$ family joins a handful of other structurally characterized multilayer hybrid halide perovskites ($n > 1$) with a group 14 metal and iodide substitute in the octahedral site. This include more materials on lead iodide compounds, such as $(CH_3(CH_2)_3NH_3)_2(CH_3NH_3)_{n-1}Pb_nI_{3n+1}$ ($n = 1\text{-}4$) [141][143][144], which have done fully investigation on the synthesis of the perovskites and the characterization and calculation of crystal structures. With another alkylammonium cation, $C_6H_5CH_2CH_2NH_3^+$ (PEA) as the organic spacer, there have been tentative assignment and reports on $(C_6H_5CH_2CH_2NH_3)_2Ge_{1-x}Sn_xI_4$ (n = 1) [145] and $(C_6H_5CH_2CH_2NH_3)_2GeI_4$ [146]. For bromide series, the crystal structures of $(CH_3(CH_2)_3NH_3)_2(CH_3NH_3)_{n-1}Pb_nBr_{3n+1}$ (n = 1, 2) [147] have been investigated before.

Table 7 Positional parameters for 2D $(CH_3(CH_2)_3NH_3)_2GeBr_4$

atom	position	x	y	z
Ge	4e	-0.00880	0.49570	0.25220
Br (1)	4e	-0.20680	0.79230	0.23600
Br (2)	4e	0.07400	0.54320	0.35860
Br (3)	4e	0.26420	0.72000	0.23710
Br (4)	4e	-0.04860	-.39440	0.14000
N (1)	4e	0.44800	0.75000	0.16400
N (2)	4e	0.04300	0.25000	0.16500
C (1)	4e	0.56200	0.75000	0.12300
C (2)	4e	0.51400	0.75000	0.08200
C (3)	4e	0.64000	0.75000	0.04500
C (4)	4e	0.59600	0.75000	0.00700
C (5)	4e	0.92500	0.25000	0.12600
C (6)	4e	0.98200	0.25000	0.08200
C (7)	4e	0.85700	0.25000	0.04700
C (8)	4e	0.90400	0.25000	0.00600

3.2.3 X-ray diffraction analysis

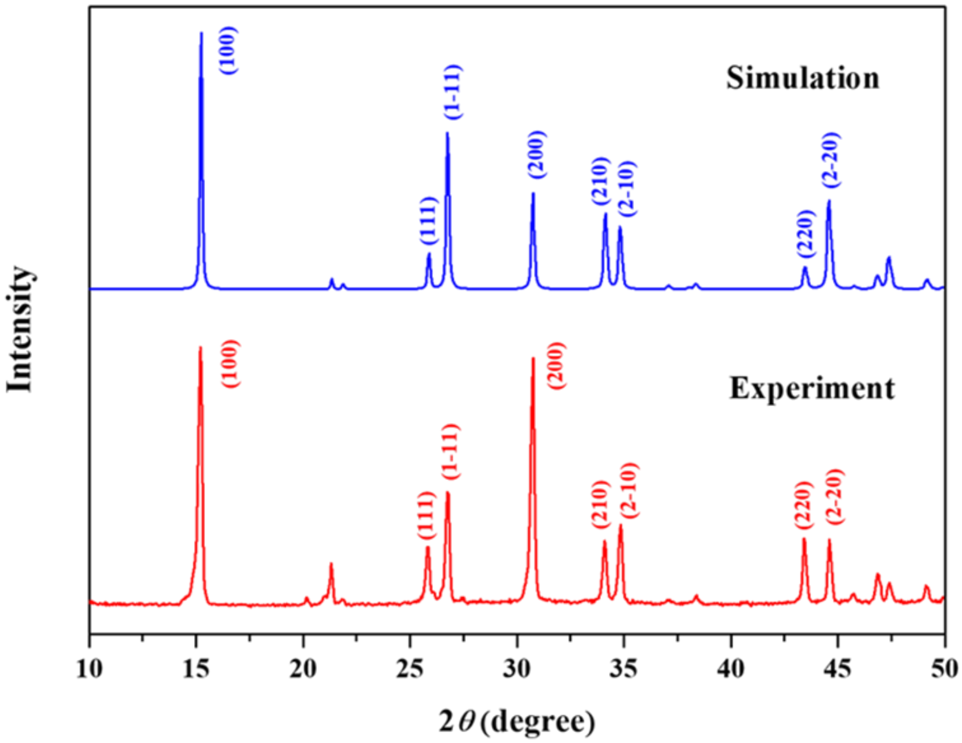

Fig. 3.9 Experimental and simulation X-ray diffraction patterns of the three-dimensional $CH_3NH_3GeBr_3$

Figure 3.9 shows both the experimental and calculation X-ray diffraction patterns of the three-dimensional $CH_3NH_3GeBr_3$. It could be observed that the experimental powder X-ray diffraction pattern has good correspondence with its simulation result, thereby confirming the pure phase of the product.

For $CH_3NH_3GeBr_3$ ($n = \infty$), the X-ray diffraction pattern shows that the main peaks are at $2\theta = 15.2°$ and 30.8°, both belonging to the (100) reflections which indicates a parallel relationship with bc planes. The other secondary peaks at $2\theta = 25.8°$, 26.7°, 34.1°, 34.85°, 43.4° and 44.6° corresponded to the (111), $(1\bar{1}1)$, (210), $(2\bar{1}0)$, (220), and $(2\bar{2}0)$ crystal planes, respectively.

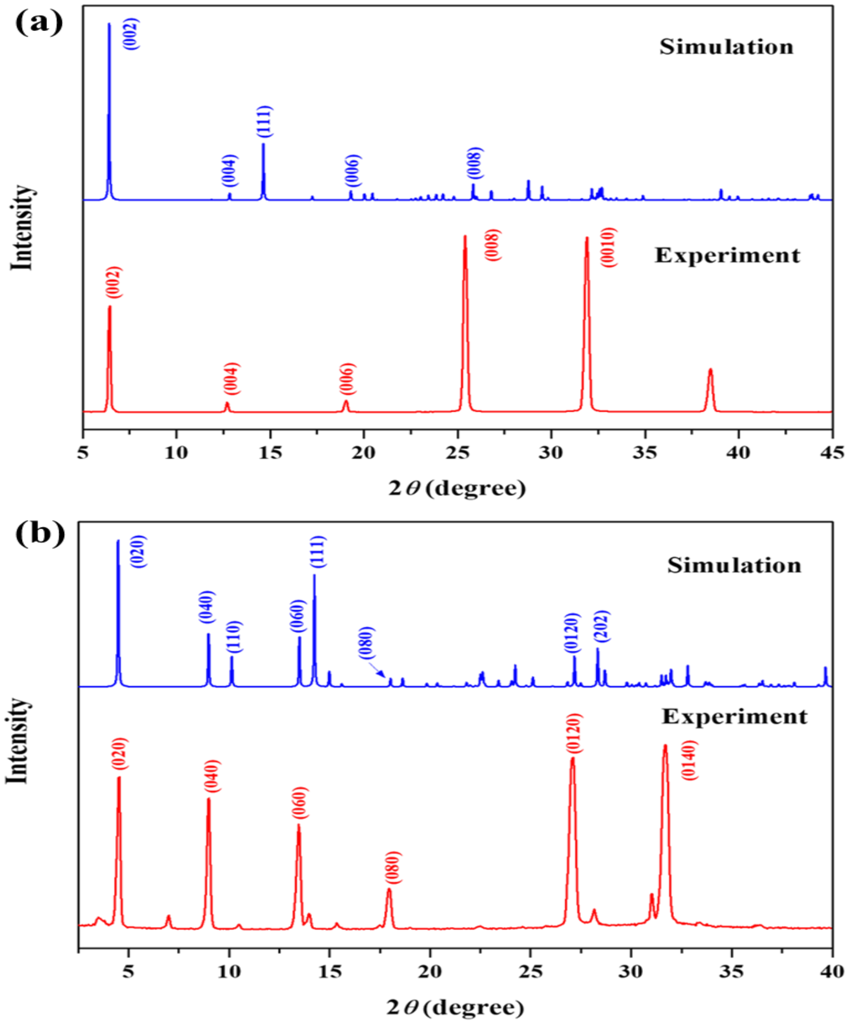

Fig. 3.10 Experimental and simulation X-ray diffraction patterns of the two-dimensional germanium bromide perovskites: (a) $(CH_3(CH_2)_3NH_3)_2GeBr_4$ (n = 1), (b) $(CH_3(CH_2)_3NH_3)_2(CH_3NH_3)Ge_2Br_7$ (n = 2)

Figure 3.10 shows experimental and calculation X-ray diffraction patterns of the two-dimensional $(CH_3(CH_2)_3NH_3)_2(CH_3NH_3)_{n-1}Ge_nBr_{3n+1}$ (n = 1, 2) perovskite family. By comparing the experimental and calculation patterns of the two as-grown crystals, the phase purity of the n = 1 compound was confirmed, while in the second product, a fraction of the second phase was mixed with the majority of n = 2 analogue, which was proved to be the n = 3 analogue by a comparison between the tiny peaks in Fig. 3.10 (b) and the simulation X-ray diffraction pattern of $(CH_3(CH_2)_3NH_3)_2(CH_3NH_3)_2Ge_3Br_{10}$.

The main peaks of $(CH_3(CH_2)_3NH_3)_2GeBr_4$ (n = 1) are at 2θ = 6.45°, 12.7°, 19.05°, 25.4° and 31.9°, respectively corresponding to the (002), (004), (006), (008) and (0010) crystal planes, which all belong to the (001) reflection. For $(CH_3(CH_2)_3NH_3)_2(CH_3NH_3)Ge_2Br_7$ (n = 2), if converting the measured main diffraction peak positions at 4.55°, 9°, 13.45°, 17.95°, 27.1° and 31.7° into interplanar spacings, they would have a one-to-one correspondence to (020), (040), (060), (080), (0120) and (0140) crystal planes. Besides, the miller indices in n=1 crystals demonstrate that the corresponding crystal planes are perpendicular to the c axis, whereas this spatial relation for the crystal planes in n=2 perovskite is with the b axis. It is obvious from Fig. 3.10 that both of the n=1 and n=2 analogues are finely crystallized and highly oriented which could be concluded from the sharp and evenly distributed diffraction peaks.

Different from the n=1 and n=2 compounds, the experimental X-ray diffraction pattern of the supposed n=3 experimental product is more complicated than the simulation result, as there are more diffraction peaks than the highly oriented group which belong to the n=3 simulation diffraction pattern, implying the impurity of the product, i.e., there exists the second phase.

The second phase turns out to be the three-dimensional $CH_3NH_3GeBr_3$ after comparison with its X-ray diffraction pattern. The corresponding Miller indices to the peaks are labeled on Fig. 3.11, among which the red ones stand for the n=3 layered $(CH_3(CH_2)_3NH_3)_2(CH_3NH_3)_2Ge_3Br_{10}$ and the other black ones stand for the three-dimensional $CH_3NH_3GeBr_3$ perovskite. We can see from the density of the diffraction peaks that, there is no content advantage for the two-dimensional perovskite over the three-dimensional one.

Like the n=1 and n=2 analogues, the diffraction peaks which belong to the n=3 compound correspond to Miller indices that could be classified to the same reflections. The diffraction peaks at 2θ=3.45°, 6.9°, 10.4°, 13.9° and 17.35° respectively represent the crystal planes of (020), (040), (060), (080) and (0100).

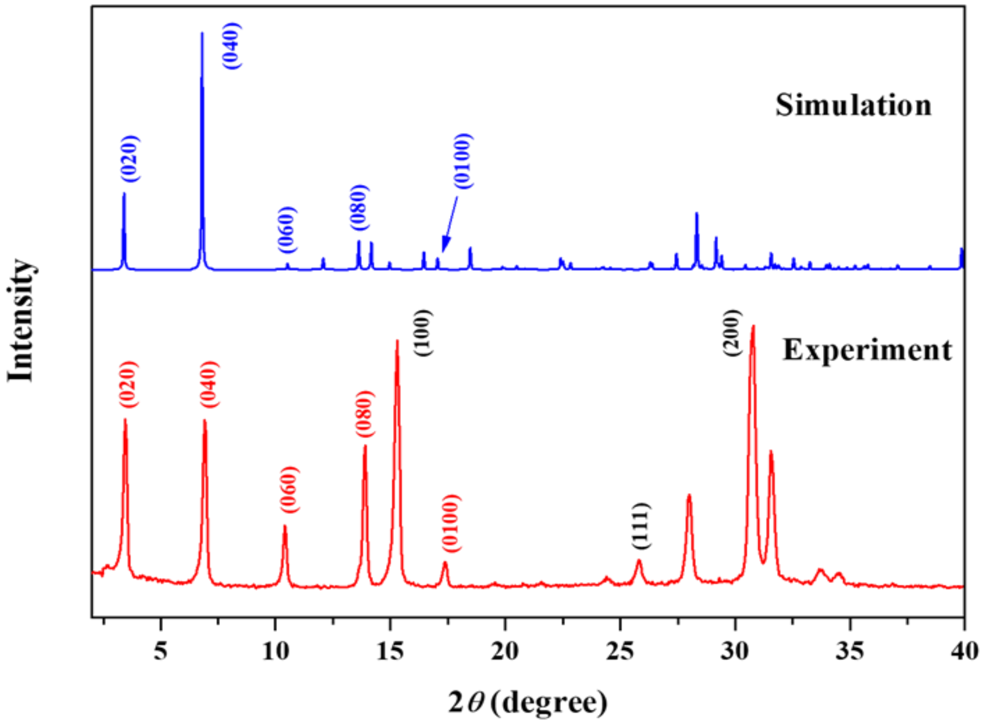

Fig. 3.11 Experimental and simulation X-ray diffraction patterns of the two-dimensional germanium bromide perovskite $(CH_3(CH_2)_3NH_3)_2(CH_3NH_3)_2Ge_3Br_{10}$ (n = 3)

If comparing the diffraction peaks of the n=1, n=2 and n=3 analogues, we can find a tendency of left shift to lower angles as the two-dimensional perovskite layers grow thicker by introducing new inorganic layers into the crystal structure. Considering the correspondence between diffraction positions and reflections, this phenomenon could be attributed to the expansion of unit cells by adding one single perovskite layer at one time as the value of n increases. [143]

3.2.4 Reflectance and photoluminescence

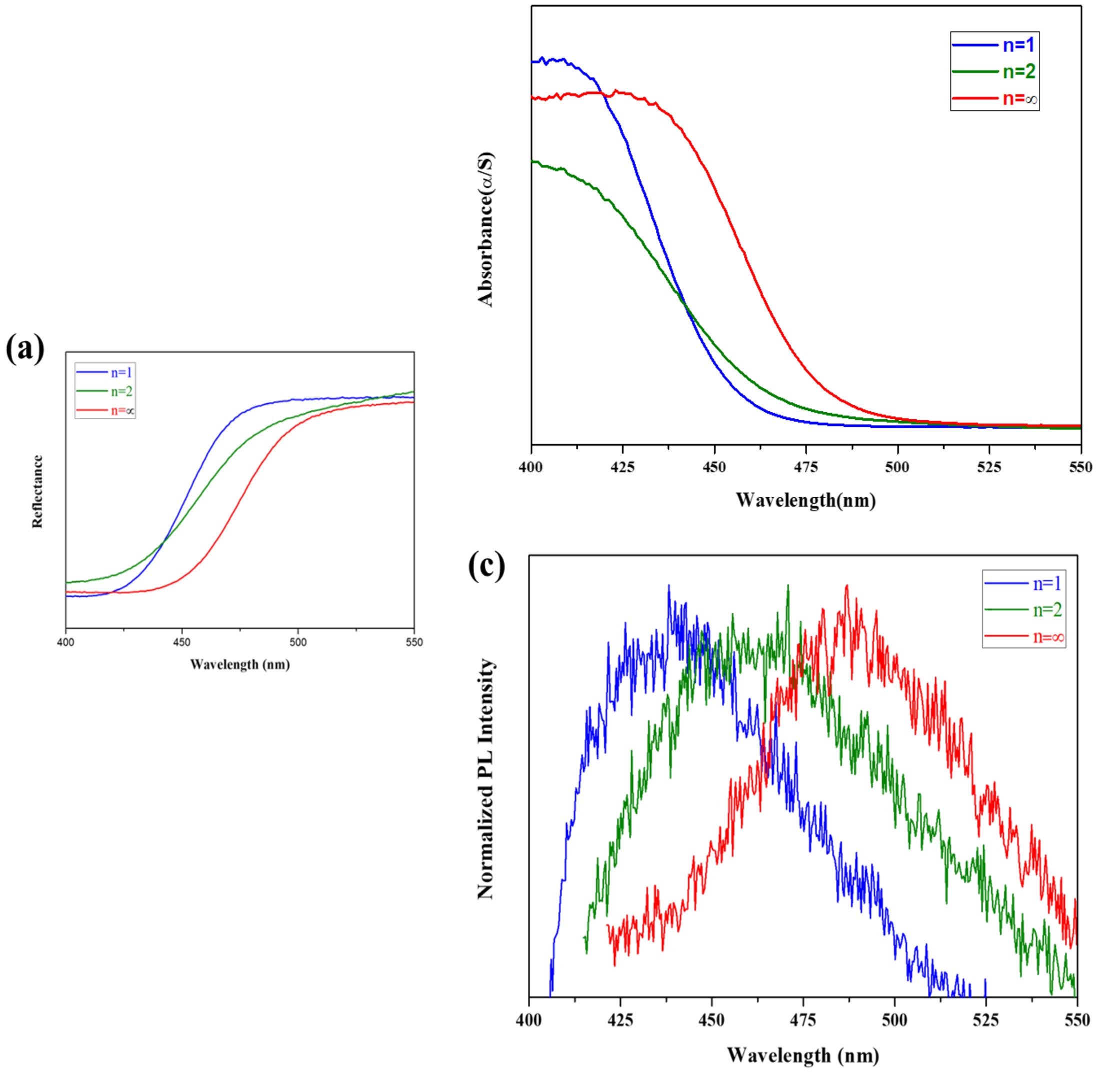

Fig. 3.12 Optical properties of the $(CH_3(CH_2)_3NH_3)_2(CH_3NH_3)_{n-1}Ge_nBr_{3n+1}$ perovskite compounds (for n = 1, 2, ∞). (a) Uv-vis-NIR diffuse reflectance spectra recorded at room temperature. (b) Optical absorption obtained from diffuse reflectance measurement (a) converted using the Kubelka-Munk function ($\alpha/S = (1-R)^2/2R$). [7, 12, 13] (c) Time-resolved photoluminescence excited by 130-fs-long laser pulses (λ_{exc}=350nm)

Fig. 3.12 displays the reflectance, absorption and time-resolved photoluminescence of the $(CH_3(CH_2)_3NH_3)_2(CH_3NH_3)_{n-1}Ge_nBr_{3n+1}$ perovskite compounds (for n = 1, 2, ∞) with respect to the wavelength at room temperature. Among them, the absorbance spectrum shown in Fig. 3.12 (b) was converted from reflectance data through the Kubelka-Munk function ($\alpha/S = (1-R)^2/2R$)

As can be seen, the three compounds show relatively strong absorptions with the respective onset wavelengths of ∽415nm for $(CH_3(CH_2)_3NH_3)_2GeBr_4$ (n = 1), ∽ 420nm for $(CH_3(CH_2)_3NH_3)_2(CH_3NH_3)Ge_2Br_7$ (n = 2) and ∽ 435nm for $(CH_3NH_3)GeBr_3$ (n = ∞), which displays an increasing tendency as the n value increases. The time-resolved photoluminescence is excited by a pump wavelength around 350nm. As the perovskite layers become thicker, the photoluminescence spectra gradually red-shift, with the center peaked located around 438nm, 460nm and 487nm corresponding to the n = 1, n = 2 and n = ∞ compounds, respectively. Therefore, both the absorption and photoluminescence show the same trend in the wavelength variation following the change of n values

From the spectrum form of Planck equation $E = hc/\lambda$, we know that the wavelength is tightly connected with the incident energy. In order to further investigate the optical bandgaps of the layered germanium perovskite series, the result of UV-vis reflectance spectroscopy was converted into Tauc plot [155]. The Tauc model allows us to derive the band gap energy Eg from $E(\varepsilon)^n$ as a function of the incident energy E. [156] The Tauc optical band gap related to the perovskite crystals is determined through an extrapolation of the linear trend observed in the spectral dependence of $(\alpha h\nu)^{1/n}$ over a limited range of photon energies hν, which could be obtained by Tauc's equation:

$$(\alpha h\nu)^{1/n} = A(h\nu - E_g) \tag{3.1}$$

Where, A is a constant, hν is photon energy, Eg is the energy gap, and the value of the exponent n denotes the nature of the transition: a) n = 1/2 for allowed direct transitions; b) r = 3/2 for direct forbidden transitions; c) n = 2 for allowed indirect transition; d) r = 3 for indirect forbidden transitions.[157]

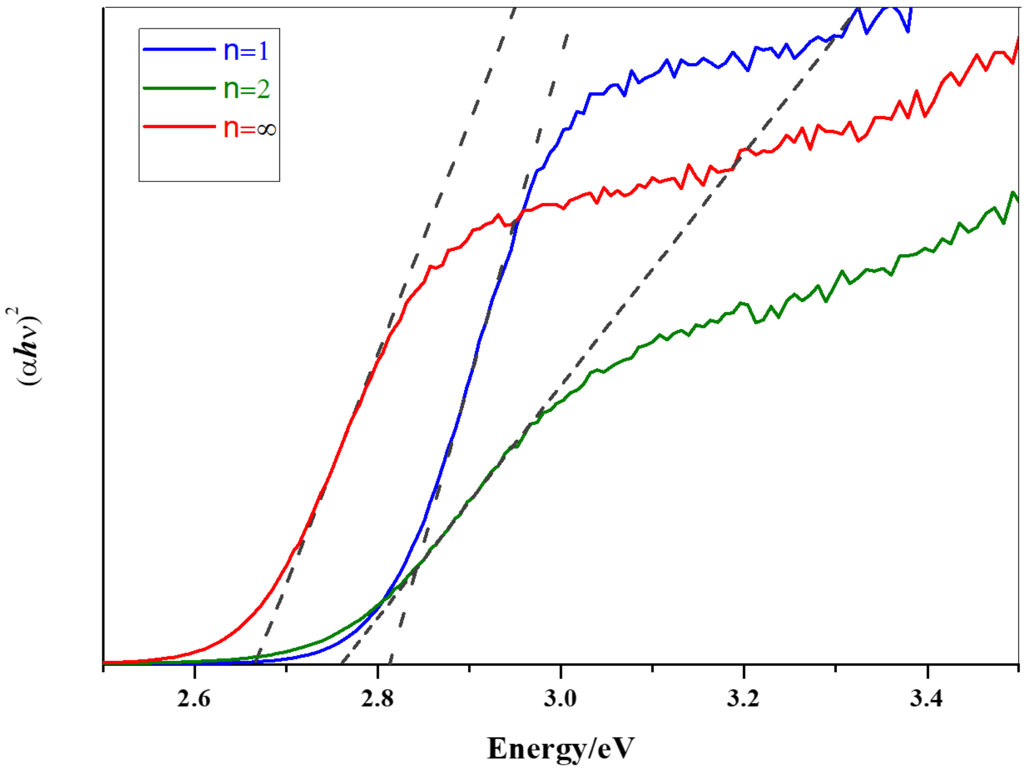

Fig. 3.13 Tauc plots of the $(CH_3(CH_2)_3NH_3)_2(CH_3NH_3)_{n-1}Ge_nBr_{3n+1}$ perovskite compounds (for n = 1, 2, ∞). The grey dash lines are the tangent lines of the straight line sections of the curves.

Here in this work, we first assumed that the two-dimensional $(CH_3(CH_2)_3NH_3)_2(CH_3NH_3)_{n-1}Ge_nBr_{3n+1}$ perovskites are direct bandgap semiconductors. The $(\alpha h\upsilon)^2$-E curves are illustrated in Fig. 3.13. Tangent lines are performed for the picked straight line sections, which are the grey dash lines in the figure. As can be seen from Fig. 3.13, opposite to the increase of n values (n= 1, 2, ∞), there exits an obvious decreasing trend in the bandgaps of the two-dimensional $(CH_3(CH_2)_3NH_3)_2(CH_3NH_3)_{n-1}Ge_nBr_{3n+1}$ perovskites, which is in accordance with the change in crystal colors, from nearly achromatic to pale yellow and finally to bright yellow (Fig. 3.6). And this phenomenon is due to quantum confinement effects from the dimensional reduction of the perovskite chromophore. [144][158][159][160] Two-dimensional perovskites, as have been discussed before, could be regarded as natural quantum wells with the semiconducting inorganic layers acting as the “wells” and the insulating organic layers acting as the "barriers". That would confine the excitons within the inorganic layers and lead to high exciton binding energy.[161][162]Note that the purpose of depicting Tauc plot here is not for quantification, but for the reveal of the variation trend of the bandgaps with the increasing of the perovskite layers. But what is still distinct is that, the layered $(CH_3(CH_2)_3NH_3)_2(CH_3NH_3)_{n-1}Ge_nBr_{3n+1}$ perovskite compounds are not suitable to be applied for single-junction solar cells, for which the proper bandgaps should be around 1.4eV. Nevertheless, there are possibilities to combine them with silicon as absorbers for tandem solar cells, as $CH_3NH_3PbBr_3$ with Eg= 2.26eV has been investigated and proved before. [146][163]

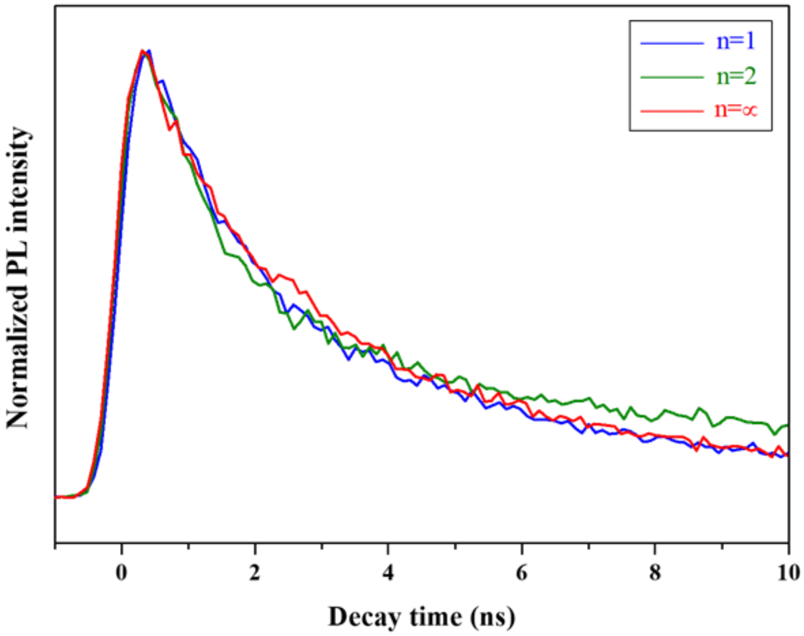

Fig. 3.14 Photoluminescence decay time of the $(CH_3(CH_2)_3NH_3)_2(CH_3NH_3)_{n-1}Ge_nBr_{3n+1}$ perovskite compounds (for n = 1, 2, ∞) at room temperature

Accompanying the time-resolved photoluminescence, the corresponding carrier recombination lifetime was detected and collected by a time-correlated single photon counting (TCSPC) setup. Then the raw data were fitted by exponential delay curve,. The curves were listed in Fig. 3.14. The three organo-germanium bromide perovskite materials have similar decay time, all around 3ns, which is too short to produce high-performance photovoltaic devices if compared with the conventional organo-lead perovskites. But as we have mentioned above, they are still worth exploiting in solar absorber region.[164][165]

3.3 Conclusion

In this chapter, we mainly concentrated on the fabrication and characterization of layered $(CH_3(CH_2)_3NH_3)_2(CH_3NH_3)_{n-1}Ge_nBr_{3n+1}$ series (n=1, 2, ∞). For the first time, we successfully obtained pure n=1 $(CH_3(CH_2)_3NH_3)_2GeBr_4$ perovskite single crystals with proved reproducibility. The synthesis method of cooling crystallization is not complicated but subtle. The product could be influenced by many factors, among which, the amount of n-butylammine is the key point and still needs further investigation.

Via powder X-ray diffraction, the purity of the product was confirmed. Combining simulation with the X-ray diffraction pattern, the crystal structures of three-dimensional $(CH_3NH_3)_3GeBr_3$ and two-dimensional $(CH_3(CH_2)_3NH_3)_2GeBr_4$ perovskites were constructed, together with their crystal data, such as crystal system, space group, unit cell lengths, unit cell angles and so on. Via the three-dimensional crystal structure graphs, we can better analyze and understand the photoelectrical behavior of the layered organo-metal halide perovskite materials.

The reflectance and time-resolved photoluminescence spectroscopy analysis demonstrates a tendency that the optical bandgaps (E_g) in the $(CH_3(CH_2)_3NH_3)_2(CH_3NH_3)_{n-1}Ge_nBr_{3n+1}$ series decrease with increased thickness of the inorganic layers, which could be attributed to the quantum confinement effects.

From the estimated bandgaps (probably larger than 2eV) and the fitted decay time, we can find that even though the $(CH_3(CH_2)_3NH_3)_2(CH_3NH_3)_{n-1}Ge_nBr_{3n+1}$ series are not suitable for solar cells, they are still promising and attracting materials in the solar absorber field,

Chapter4 Fabrication and characterization of two-dimensional $(CH_3(CH_2)_3NH_3)_2GeI_4$ perovskite

As a member of the same halogen group to bromide (Br), iodide (I)- based perovskite materials have always been the top academic research direction as well. In this chapter, we prepared layered two-dimensional $(CH_3(CH_2)_3NH_3)_2GeI_4$ perovskite single crystals and investigated its crystal structure and photoelectrical properties by means of powder X-ray diffraction, UV-vis reflectance and time-resolved photoluminescence. Besides, we also compared this two-dimensional germanium iodide perovskite with its three-dimensional analogue — $(CH_3NH_3)_3GeI_3$.

4.1 Experimental section

4.1.1 Starting materials

Hypophosphorous acid (H_3PO_2), hydroiodic acid (HI), germanium dioxide (GeO_2) and n-butylamine ($CH_3(CH_2)_3NH_2$) were all purchased from Sigma-Aldrich.

4.1.2 Synthesis

The whole synthesis process was carried out under high purity nitrogen.

$\boldsymbol{(BA)_2GeI_4}$ **(n = 1)**. A two-neck flask was charged with a mixture of 57% w/w aqueous HI (20.0mL, 150mmol) and 50% w/w aqueous H_3PO_2 (10.0mL, 91mmol). GeO_2 powder (1046mg, 10mmol) was dissolved in the mixture by heating the flask to 140°C in an oil bath, under constant magnetic stirring for about 20min, which formed a bright yellow solution. In a separate flask, $n-CH_3(CH_2)_3NH_2$ (986μL, 10mmol) was neutralized with 57% w/w aqueous HI (5mL, 37.5mmol) in an ice bath, resulting a bright yellow solution. The $n-CH_3(CH_2)_3NH_3I$ solution was then added dropwise into the two-neck flask. After being heated continuously at 160°C for about 10min, the stirring was discontinued, and the solution was left to cool down to room temperature. Upon cooling, large amount of red needle-like crystals were precipitated from the mother liquor. After being kept in the solution overnight, the crystals were collected by suction filtration and dried under reduced pressure.

4.1.3 Characterization

Powder X-ray diffraction (XRD)

Powder X-ray diffraction measurement was performed at room temperature using a Bruker D8-Discover diffractometer (Bragg-Brentano geometry) for crystals with parallel beam geometry and Cu Ka wavelength (λ=1.5418Å), operated at 40 kV and 40 mA using a step size of 0.05° and a time per step of 1 s within the Bragg angle from 4°

to 50°. The powder sample was placed on a Bruker silicon sample holder.

Optical diffuse reflectance spectroscopy

The reflectance measurement was performed at room temperature using a Cary 5000 UV-Vis-NIR spectrophotometer with double out-of-plane Littrow monochromator. The spectra was recorded by electrothermally controlled lead sulfide photocell (NIR detector) incorporating PbSmart technology the optimum low noise and ultimate linearity performance. A Hg lamp module is applied for automatic wavelength accuracy validation. The measurement started at 200nm and stopped at 900nm.

Time-resolved photoluminescence spectroscopy

The sample was prepared on transparent glass substrates where the crystals were attached on and then inserted into a square sample holder which was vacuumized later. In time-resolved photoluminescence experiments, samples were excited with a regenerative amplified laser (Coherent Libra) delivering 130-fs-long pulses at a repetition rate of 1 KHz. Photoluminescence was dispersed with a grating spectrometer (Princeton Instruments Acton SpectraPro 2300i equipped with a 50 gr/mm grating blazed at 600 nm), dispersed and detected by a streak camera (Hamamatsu).

4.2 Results and discussion

4.2.1 Synthesis

The target product, $(CH_3(CH_2)_3NH_3)_2GeI_4$, belonging to the layered two-dimensional $(CH_3(CH_2)_3NH_3)_2(CH_3NH_3)_{n-1}Ge_nI_{3n+1}$ series with n=1, was synthesized from a stoichiometric reaction between GeI_2 and n- $CH_3(CH_2)_3NH_3I$. Upon continuous heating at 140℃ for about 10min after the addition of neutralized n-butylammonium (n-CH3(CH2)3NH3), both of the heating and magnetic stirring were stopped. After a while, before cooling to ambient condition, the solution started to precipitate out bright red solids, which can be seen from Fig. 4.1(a). As the precipitation is sensitive to ethyl alcohol and isopropanol, suction filtration was used here without washing step. Fig.

4.1(b) clearly displays the tiny and subtle feature of the crystals with vivid red color and needle-like appearance.

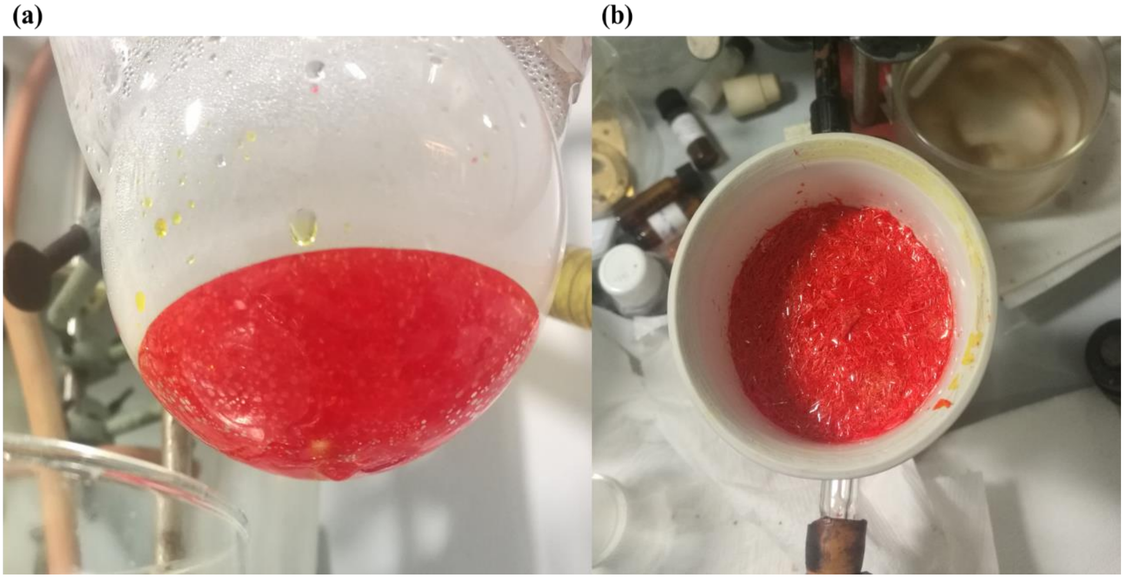

Fig. 4.1 Photographs of the $(CH_3(CH_2)_3NH_3)_2GeI_4$ perovskite crystals, (a) precipitation in the mother liquor after cooling to room temperature; (b) precipitation during the suction filtration procedure

4.2.2 X-ray diffraction analysis and crystal structure description

The simulation and experimental Powder X-ray diffraction patterns of $(CH_3(CH_2)_3NH_3)_2GeI_4$ are presented in Fig. 4.2, with diffraction peaks marked with corresponding Miller indices. The positional data of the atoms for simulation are from DB Mitzi [166]. The main peaks of $(CH_3(CH_2)_3NH_3)_2GeI_4$ (n = 1) are at 2θ = 6.25°, 25.3° and 32.2°, respectively corresponding to the (002), (008) and (0010) crystal planes, demonstrating high orientation. Comparing the peak positions of $(CH_3(CH_2)_3NH_3)_2GeI_4$ with that of $(CH_3(CH_2)_3NH_3)_2GeBr_4$ (the diffraction peaks of (002), (008) and (0010) crystal planes respectively appeared at 2θ = 6.45°, 25.4° and 31.9°), we can find small left shift towards the low angle in the iodide perovskite, which is due to the increased lattice parameters caused by the larger atom diameter of iodide than bromide.

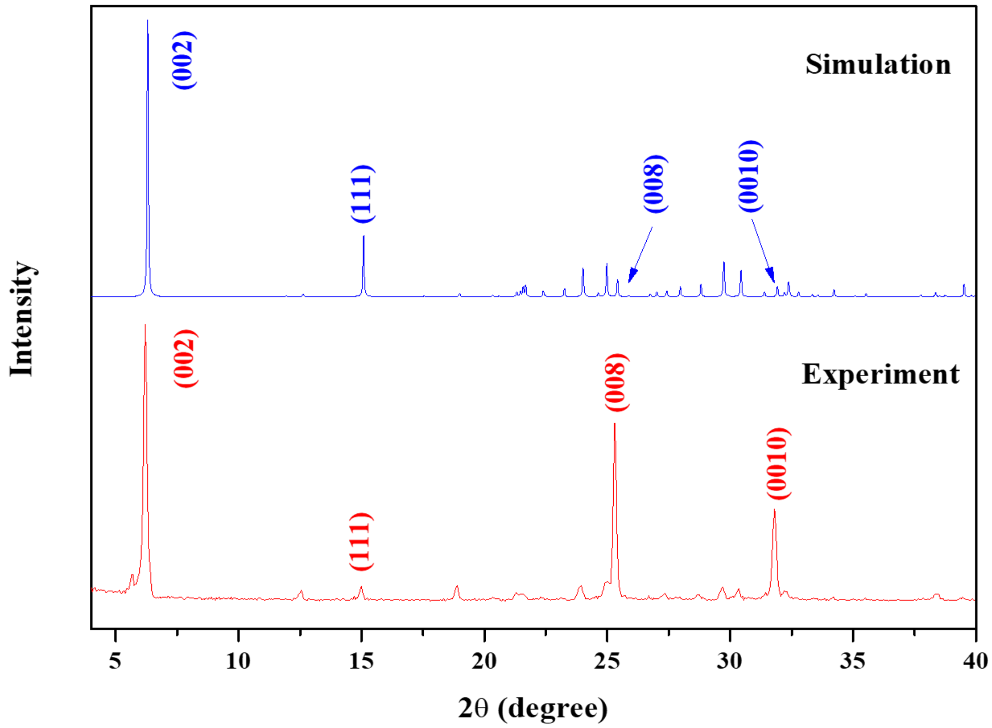

Fig. 4.2 Experimental and simulation X-ray diffraction patterns of the layered two-dimensional $(CH_3(CH_2)_3NH_3)_2GeI_4$

With the crystallographic data from Mitzi (Table 8) [166], we constructed the three-dimensional crystal structure of $(CH_3(CH_2)_3NH_3)_2GeI_4$ by VESTA (Fig. 4.3). The layered $(CH_3(CH_2)_3NH_3)_2GeI_4$ compound adopts a orthorhombic distortion structure crystallizing in the polar Rcmn space group. In the $[GeI_6]^{4-}$ octahedra, the lengths of the six Ge-I bonds vary from 2.837Å to 3.217Å, and the Ge-I-Ge bond angles deviate severely from 180 °, referring to 166.27 ° (along the a-b plane). With the crystallographic data of three-dimensional $CH_3NH_3GeI_3$ from CC Stoumpos [167], we also build the crystal structure again and calculate the Ge-I-Ge bond angle to be 167.6579° by VESTA, which implies a less severe distortion of the $[GeI_6]^{4-}$ octahedra.

Table 8 Crystal data for layered two-dimensional $(CH_3(CH_2)_3NH_3)_2GeI_4$

Formula	**$(CH_3(CH_2)_3NH_3)_2GeI_4$**
Formula weight	728.499
Crystal system	Orthorhombic
Space group	Pcmn
Unit cell length (Å)	a=8,7220
	b=8.2716
	c=28.014
Unit cell angles	$\alpha=\beta=\gamma=90°$
Volume (Å^3)	2021.1
Z	4
Density(calc), g/cm^3	2.394

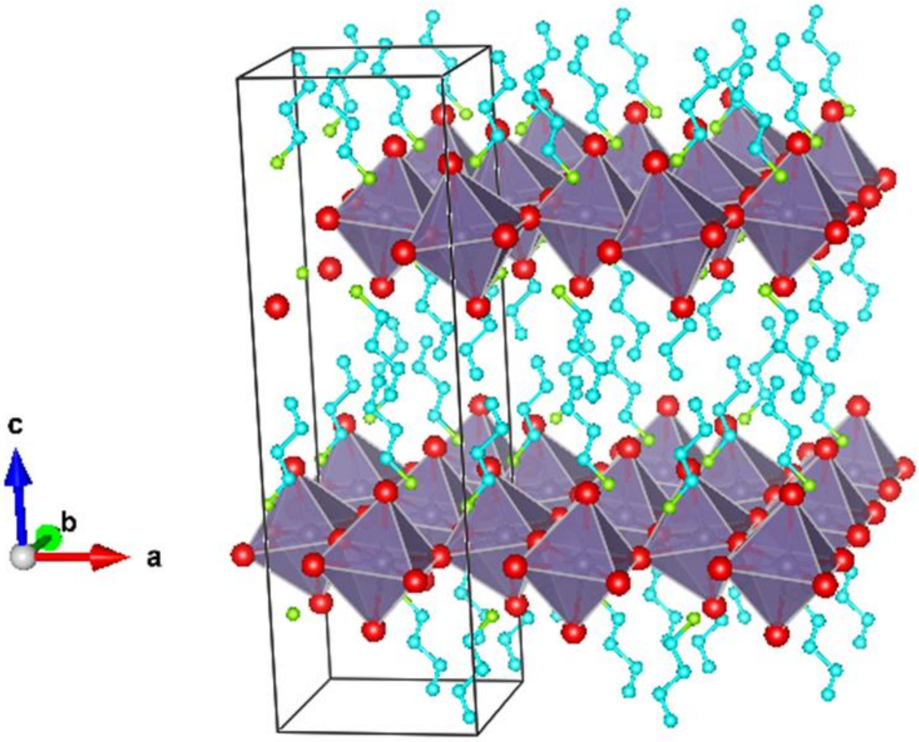

Fig. 4.3 Crystal data for layered two-dimensional $(CH_3(CH_2)_3NH_3)_2GeI_4$. Purple (in the center of the $[GeI_6]^{4-}$ Octahedra), red, blue and green spheres represent germanium (Ge), iodide (I), nitrogen (N) and carbon (C), respectively.

4.2.3 Reflectance and photoluminescence

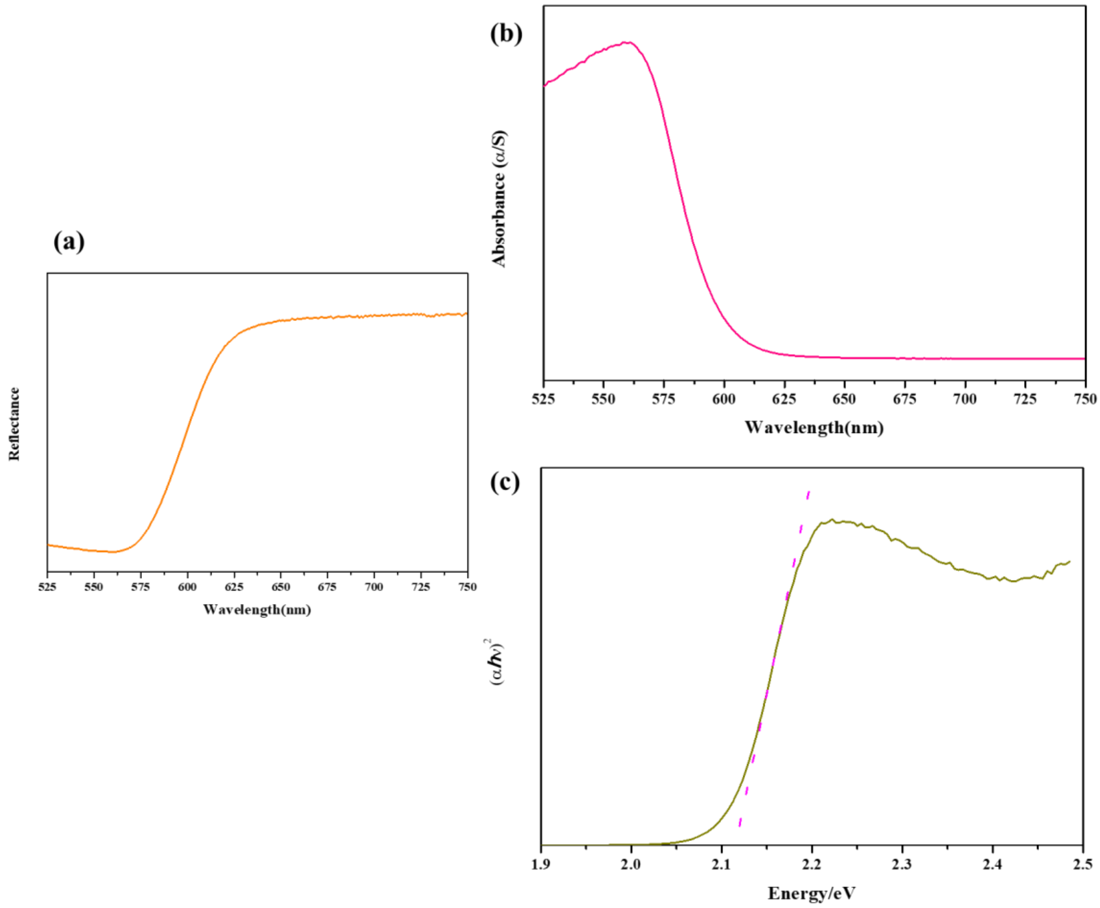

Fig. 4.4 (a) Uv-vis-NIR diffuse reflectance spectra of layered $(CH_3(CH_2)_3NH_3)_2GeI_4$ recorded at room temperature. (b) Optical absorption of layered $(CH_3(CH_2)_3NH_3)_2GeI_4$ obtained from diffuse reflectance measurement (a) converted using the Kubelka-Munk function ($\alpha/S = (1-R)^2/2R$). (c) Tauc plot of layered $(CH_3(CH_2)_3NH_3)_2GeI_4$

To further investigate the photoelectronic properties, UV-vis-NIR diffuse reflectance was applied to measure $(CH_3(CH_2)_3NH_3)_2GeI_4$. Through Kubelka-Munk equation, the reflectance data were converted to absorption. The Absorbance-wavelength curve is plotted in Fig. 4.4(b). Moreover, by means of the Tauc model, we obtained the Tauc plot of $(CH_3(CH_2)_3NH_3)_2GeI_4$ for the estimation of the bandgap (E_g) as well (Fig. 4.4 (c)).

From Fig. 4.4 (b) we can find an excellent absorbing performance with an onset at about

560nm. In comparison to the Tauc plot of germanium bromide perovskites in chapter 3, $(CH_3(CH_2)_3NH_3)_2GeI_4$ presents a comparatively lower band gap, which is however still too high to be applied as solar cells.

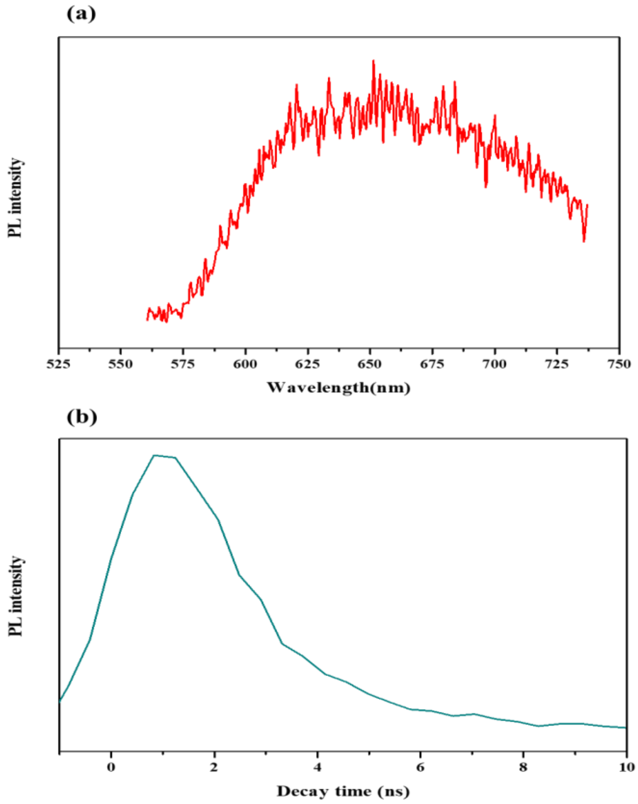

Fig. 4.5 (a) Time-resolved photoluminescence spectrum of layered $(CH_3(CH_2)_3NH_3)_2GeI_4$ (n=1) at room temperature. (b) photoluminescence decay profile of $(CH_3(CH_2)_3NH_3)_2GeI_4$ compound at room temperature

The time-resolved photoluminescence spectrum of layered $(CH_3(CH_2)_3NH_3)_2GeI_4$ (n=1) at room temperature is presented in Fig. 4.5 (a), followed by the decay time graph in Fig. 4.5 (b). Actually, the $(CH_3(CH_2)_3NH_3)_2GeI_4$ compound displays a comparatively gentle photoluminescence spectrum with a large peak width around 150nm as well as a significantly small peak intensity with a peak center around 650nm, while for the $(CH_3(CH_2)_3NH_3)_2(CH_3NH_3)_{n-1}Ge_nBr_{3n+1}$ analogues we discussed in chapter 3, narrower peak widths (around 100nm) and larger peak intensity were all obtained from n=1, n=2 and n= ∞, with blue shifted peak centers. The blue-shift phenomenon is resulted from the stronger covalent interaction of iodide than that of bromide, as the electronegativity decreases with the increase of atomic number in the same main group.

As to the decay time, we fitted the raw data by a biexponential delay curve, given a long-lifetime of about 2.5ns, extremely short given that the conventional lead halide perovskites have reached lifetimes of hundreds of nanoseconds, some even exceeding microsecond.[168][169][170][171]

Generally speaking, the photoluminescence behavior sharply decreases in the order M=Pb(II)> Sn(II)> Ge(II), of which the most probable incentive is a smaller exciton binding energy for the lighter group IVB element compounds. [166] In addition, defects that may exit in the compounds we synthesized and a great propensity for oxidation could lead to a wider peak, lower photoluminescence intensity and short decay time as well. Here in our research, the photoelectronic properties are supposed to be enhanced by improving the chemical synthesis in order to obtain single crystals with larger size and higher quality, as the small size and needle-like morphology of the crystals could be defects and traps to limit carrier diffusion.

4.3 Conclusion

In this chapter, we mainly concentrated on the fabrication and characterization of layered $(CH_3(CH_2)_3NH_3)_2(CH_3NH_3)_{n-1}Ge_nI_{3n+1}$ perovskite with n=1. With the same synthesis method of cooling crystallization to $(CH_3(CH_2)_3NH_3)_2(CH_3NH_3)_{n-1}Ge_nBr_{3n+1}$ series but different experiment parameters, we successfully obtained red needle-like $(CH_3(CH_2)_3NH_3)_2GeI_4$ single crystals with high purity.

Combining former experiment and calculation data with our experiment result, we constructed the three-dimensional crystal structure by VESTA, obtained related crystallographic parameters and discussed about the characteristics of $(CH_3(CH_2)_3NH_3)_2GeI_4$.

Through the reflectance and time-resolved photoluminescence spectroscopy analysis, the approximate bandgap range was estimated to be smaller than that of layered $(CH_3(CH_2)_3NH_3)_2(CH_3NH_3)_{n-1}Ge_nBr_{3n+1}$ compounds, followed by wider photoluminescence peak width and smaller intensity.

Even though the performance of the decay time was not satisfying either, we still believe in great improvement in the photoelectronic properties of the layered germanium perovskite via optimizing and refining the parameters of the fabrication.

Chapter 5 Summary and Outlook

Although it has been only ten years since perovskite materials was considered to be a potential candidate for solar cells and aroused wide and intense attention and investigation then, with the incipient power conversion efficiency (PCE) of 3.9% in 2009, perovskite solar cells have soared recently, reaching a power conversion efficiency over 23%. And due to the excellent photoelectronic properties, such as tunable bandgaps, high panchromatic absorption and charge carrier diffusion length, organometal halide perovskites have made prominent progress. In addition to solar cells, they could be applied in a variety of regions, ranging from lasing, light emitting devices, sensing, photodetectors as well as X-ray and particle-detection. As the representing perovskite material, methylammonium lead halide perovskite compound has achieved high power conversion efficiency, enabling exploration in new lead- free region. People have been trying to replace lead which is toxic with environment-friendly elements like tin (Sn) and germanium (Ge).

In our work represented in the thesis, we mainly concentrated on the layered two-dimensional $(CH_3(CH_2)_3NH_3)_2(CH_3NH_3)_{n-1}Ge_nX_{3n+1}$ (X=Br, I) perovskites. For the first time, pure layered $(CH_3(CH_2)_3NH_3)_2GeBr_4$ (n=1) was fabricated successfully, which could be certified by the comparison of powder X-ray diffraction pattern between the experimental and calculated result. Furthermore, we constructed the unit cell of $(CH_3(CH_2)_3NH_3)_2GeBr_4$ and the three-dimensional $CH_3NH_3GeBr_3$, along with their crystallographic parameters. From the crystal data, we know that the layered $(CH_3(CH_2)_3NH_3)_2GeBr_4$ adopts a monoclinic distortion structure crystallizing in the polar R21/c space group, showing lower symmetry than that of $CH_3NH_3GeBr_3$, who crystallizes in the R3m space group of a trigonal crystal system. For the synthesis of n=2 compound, the X-ray diffraction result showed that the crystals were composed of a majority of $(CH_3(CH_2)_3NH_3)_2(CH_3NH_3)Ge_2X_7$ and a small fraction of n=3 analogue. But for the n=3 experiment, intense diffraction peaks of $CH_3NH_3GeBr_3$ were detected, proving the overwhelming proportion of n=3 compound. If comparing the diffraction peaks of the n=1, n=2 and n=3 analogues, we can find a tendency of left shift to lower angles as the two-dimensional perovskite layers grow thicker by introducing new inorganic layers into the crystal structure which is resulted from the expansion of unit cells by adding one single perovskite layer at one time as the value of n increases.

The reflectance and time-resolved photoluminescence spectroscopy analysis demonstrates a tendency that the optical bandgaps (Eg) in the $(CH_3(CH_2)_3NH_3)2(CH3NH3)_{n-1}Ge_nBr_{3n+1}$ series decrease with increased thickness of the inorganic layers, which could be attributed to the quantum confinement effects.

From the estimated bandgaps (probably larger than 2eV) and the fitted decay time, we can find that even though the $(CH_3(CH_2)_3NH_3)_2(CH_3NH_3)_{n-1}Ge_nBr_{3n+1}$ series are not suitable for solar cells, they are still promising and attracting materials in the solar absorber field.

In addition to bromide perovskite, we also synthesized layered two-dimensional $(CH_3(CH_2)_3NH_3)_2GeI_4$ perovskite respecting to n=1. The compound was synthesized by the same cooling crystallization method with different experimental parameters. Unlike the $(CH_3(CH_2)_3NH_3)_2(CH3NH3)_{n-1}Ge_nBr_{3n+1}$ series, who were precipitated in yellow with a lamellar morphology, $(CH_3(CH_2)_3NH_3)_2GeI_4$ crystallized in a needle-like morphology, displaying bright red color.

Through the reflectance and time-resolved photoluminescence spectroscopy analysis, the approximate bandgap range was estimated to be smaller than that of layered $(CH_3(CH_2)_3NH_3)_2(CH_3NH_3)_{n-1}Ge_nBr_{3n+1}$ compounds. Also the photoluminescence spectrum exhibited a significantly smaller peak intensity and a much larger peak width, which could be attributed to the oxidation of Ge (II) in the inorganic layers and the defects inside the crystal or at the boundaries of the crystal particles. Even though neither of the layered two-dimensional $(CH_3(CH_2)_3NH_3)_2(CH_3NH_3)_{n-1}Ge_nBr_{3n+1}$ series nor the $(CH_3(CH_2)_3NH_3)_2GeI_4$ demonstrate good photoelectric performance, still, we look forward to greatly improved their properties by refining the parameters of the fabrication to increase the size of the crystals, optimize the morphologies, and decrease the defects inside

All in all, we have succeeded in making the layered two-dimensional $(CH_3(CH_2)_3NH_3)_2GeBr_4$ with high purity and constructing corresponding crystal structure, providing a new way for the development of two-dimensional germanium-based perovskites.

Reference

[1]. Y.B. Bai, Q.Y. Wang, R.T. Lv, H.W. Zhu, F.Y Kang. Progress on perovskite-based solar cells. Chinese Science Bulletin. 2016, 61(4-5), 489-500.

[2]. G.D. Niu, X.D. Guo, L.D. Wang. Review of Recent Progress in Chemical Stability of Perovskite Solar Cells. Journal of Materials Chemistry A. 2015.

[3]. Newcomer Juices Up the Race to Harness Sunlight. Science, 2013, 342, 1438-1439.

[4]. C.R. Kagan, D.B. Mitzi, C.D. Dimitrakopoulos. Science, 1999, 286-945.

[5]. J.H. Burroughes, D.D.C Bradley, A.R. Brown, R.N. Marks, K. Mackay, R.H. Friend, P.L. Burns, A.B. Holmes. Nature, 1990, 347-539.

[6]. A. Kojima, K. Teshima, Y. Shirai and T. Miyasaka, J. Am. Chem. Organometal Halide Perovskites as Visible-Light Sensitizers for Photovoltaic Cells. Soc., 2009, 131, 6050-6051.

[7]. N.G. Park. Organometal Perovskite Light Absorbers Toward a 20% Efficiency Low-Cost Solid-State Mesoscopic Solar Cell. J. Phys. Chem. Lett. 2013, 4, 2423−2429.

[8]. J.H. Im, C.R Lee, J.W. Lee, S.W. Park, N.G. Park. 6.5% efficient perovskite quantum-dot-sensitized solar cell. Nanoscale. 2011, 3, 4088–4093.

[9]. H.S. Kim, C.R. Lee, J.H. Im, K.B. Lee, T. Moehl, A. Marchioro, S.J. Moon, R. Humphry-Baker, J.H. Yum, J.E. Moser, M. Grätzel, N.G. Park. Lead iodide perovskite sensitized all-solid-state submicron thin film mesoscopic solar cell with efficiency exceeding 9%. Scientific Reports2. 2012, 591.

[10]. M.M. Lee, J. Teuscher, T. Miyasaka, T.N. Murakami and H.J. Efficient hybrid solar cells based on meso-superstructured organometal halide perovskites. Snaith, Science. 2012, 338, 643.

[11]. J. Burschka, N. Pellet, S.J. Moon, R. Humphry-Baker, P. Gao, M.K. Nazeeruddin, M. Grätzel. Sequential deposition as a route to high-performance perovskite-sensitized solar cells. Nature, 2013, 499-316.

[12]. M Liu, MB Johnston, HJ Snaith. Efficient planar heterojunction perovskite

solar cells by vapour deposition. Nature, 2013, 501: 395–398.

[13]. K. Wojciechowski, M. Saliba, T. Leijtens, A. Abate, H.J. Snaith. Sub-150 C processed meso-superstructured perovskite solar cells with enhanced efficiency. Energy & Environmental Science. 2014, 7 (3), 1142-1147.

[14]. A. Mei, X. Li, L.F. Liu, Z.L. Ku, T.F. Liu, Y.G. Rong, M. Xu, M. Hu, J.Z. Chen, Y. Yang, M. Grätzel, H.W. Han. A hole-conductor–free, fully printable mesoscopic perovskite solar cell with high stability. Science, 2014, 345, 295-298.

[15]. Z.H. W, H.N. Chen, K.Y. Yan, S.H. Yang. Inkjet Printing and Instant Chemical Transformation of a CH3NH3PbI3/Nanocarbon Electrode and Interface for Planar Perovskite Solar Cells. Chemie International Edition, 2014, 53, 13239

[16]. D. Liu, T.L. Kelly. Perovskite solar cells with a planar heterojunction structure prepared using room-temperature solution processing techniques. Nat. Photonics. 2014, 8-133.

[17]. DY Luo, WQ Yang, ZP Wang, A Sadhanala, Q Hu, R Su, R Shivanna, GF Trindade, JF Watts, ZJ Xu, TH Liu, K Chen, FJ Ye, P Wu, LC Zhao, J Wu, YG Tu, YF Zhang, XY Yang, W Zhang, RH Friend, QH Gong, HJ Snaith, R Zhu. Enhanced photovoltage for inverted planar heterojunction perovskite solar cells. Science. 2018, 360 (6396): 1442-1446

[18]. Y Zhang, ZM Zhou, FX Ji, ZP Li, GL Cui, P Gao, M Oveisi, MK Nazeeruddin, SP Pang. Trash into Treasure: δ-$FAPbI_3$ Polymorph Stabilized $MAPbI_3$ Perovskite with Power Conversion Efficiency beyond 21%. Adv. Mater. 2018, 30(22), 1707143

[19]. https://www.nrel.gov/pv/assets/pdfs/pv-efficiencies-07-17-2018.pdf

[20]. ZJ Shi, J Guo, YH Chen, Q Li, YF Pan, HJ Zhang, YD Xia, W Huang. Lead-free organic-inorganic hybrid perovskites for photovoltaic applications: recent advances and perspectives. Adv. Mater, 2017, 9(16), 1605005.

[21]. P. Patnaik, Handbook of inorganic chemicals; McGraw-Hill, New York 2003

[22]. R. Hamaguchi, M. Yoshizawa-Fujita, T. Miyasaka, H. Kunugita, K. Ema, Y. Takeoka, M. Rikukawa. Formamidine and cesium-based quasi-two-dimensional perovskite as photovoltaic absorbers. Chem. Commun., 2017,53, 4366-4369.

[23]. H. Zhou, Q. Chen, G. Li, S. Luo, T. Song, H.S. Duan, Z, Hong, J. You, Y. Liu, Y. Yang. Interface engineering of highly efficient perovskite solar cells. Science. 2014, 345-542.

[24]. W.J. Yin, J.H. Yang, J. Kang, Y. Yan, S.H. Wei. Halide perovskite materials for solar cells: a theoretical review. J. Mater. Chem. A. 2015,3, 8926-8942.

[25]. H. D. Kim, H. Ohkita, H. Benten and S. Ito. Photovoltaic performance of perovskite solar cells with different grain sizes. Adv. Mater., 2015, 28, 917–922.

[26]. M. Saliba, T. Matsui, K. Domanski, J.-Y. Seo, A. Ummadisingu, S. M. Zakeeruddin, J.-P. Correa-Baena, W. R. Tress, A. Abate, A. Hagfeldt and M. Grätzel, Incorporation of rubidium cations into perovskite solar cells improves photovoltaic performance. Science. 2016, 354, 206–209.

[27]. K. Tanaka, T. Takahashi, T. Ban, T. Kondo, K. Uchida, N. Miura. Comparative study on the excitons in lead-halide-based perovskite-type crystals $CH_3NH_3PbBr_3$ $CH_3NH_3PbI_3$. Solid State Commun., 2003, 127-619.

[28]. C.C. Stoumpos, M.G. Kanatzidis. The renaissance of halide perovskites and their evolution as emerging semiconductors. Accounts of chemical research, 2015, 48(10): 2791-2802.

[29]. J.W. Lee, D.J. Seol, A.N. Cho, et al. High-efficiency perovskite solar cells based on the black polymorph of HC(NH2)2PbI3. Adv Mater, 2014, 26: 4991–4998.

[30]. S. Hesse, J. Zimmermann, H. von Seggern, H. Ehrenberg, H. Fuess, C. Fasel, R. Riedel. CsEuBr3: Crystal structure and its role in the photostimulation of CsBr:Eu2+. J. Appl. Phys. 2006, 100, 083506.

[31]. U. Shirwadkar, E. V. D. van Loef, R. Hawrami, S. Mukhopadhyay, J. Glodo, K.S. Shah. New promising scintillators for gamma-ray spectroscopy: Cs(Ba,Sr)(Br,I). 3. IEEE NSS/MIC Conference 2011, 1583.1585.

[32]. F. Jing. Mechanical properties of hybrid organic-inorganic CH3NH3BX3(B=Sn,Pb; X=Br, I) perovskites for solar cell absorbers. APL Mater. 2014, 2: 081801.

[33]. S.A. Kulkarni, T. Baikie, P.P. Boix, et al. Band-gap tuning of lead halide perovskites using a sequential deposition process. J Mater Chem A. 2014, 2: 9221–9225.

[34]. L.Y. Huang, W.R.L. Lambrecht. Electronic band structure, phonons, and exciton binding energies of halide perovskites CsSnCl3, CsSnBr3, and CsSnI3. Phys Rev B. 2013, 88: 165203.

[35]. F. Brivio, A.B. Walker, A. Walsh. Structural and electronic properties of hybrid perovskites for high-efficiency thin-film photovoltaics from first-principles. APL Mater. 2013, 1, 042111.

[36]. G. Niu, X. Guo, L. Wang, Review of recent progress in chemical stability of perovskite solar cells. J. Mater. Chem. A. 2015, 3, 8970.

[37]. C.C. Stoumpos, C.D. Malliakas, M.G. Kanatzidis, Semiconducting tin and lead iodide perovskites with organic cations: phase transitions, high mobilities, and near-infrared photoluminescent properties. Inorg. Chem. 2013, 52 9019—9038.

[38]. A. Poglitsch, D. Weber. Dynamic disorder in methylammoniumtrihalogenoplumbates (II) observed by millimeter-wave spectroscopy. J. Chem. Phys. 1987, 87 6373—6378.

[39]. Q. Chen, N. De Marco, Y.M. Yang, T.B. Song, C.C. Chen, H.X. Zhao, Z.R. Hong, H.P. Zhou, Y. Yang. Under the spotlight: The organic–inorganic hybrid halide perovskite for optoelectronic applications. Nanotoday. 2015, 10 (3): 355-396.

[40]. G. E. Eperon, T. Leijtens, K. A. Bush, R. Prasanna, T. Green, J. T. Wang, D. P. McMeekin, G. Volonakis, R. L. Milot, R. May, A. Palmstrom, D. J. Slotcavage, R. A. Belisle, J. B. Patel, E. S. Parrott, R. J. Sutton, W. Ma, F. Moghadam, B. Conings, A. Babayigit, H. G. Boyen, S. Bent, F. Giustino, L. M. Herz, M. B. Johnston, M. D. McGehee and H. J. Snaith, Perovskite-perovskite tandem photovoltaics with optimized band gaps. Science, 2016, 354, 861-865.

[41]. T. Jesper Jacobsson, J.-P. Correa-Baena, M. Pazoki, M. Saliba, K. Schenk, M. Gratzel and A. Hagfeldt. Exploration of the compositional space for mixed lead halogen perovskites for high efficiency solar cells. Energy & Environmental

Science. 2016, 9, 1706-1724.

[42]. N. J. Jeon, J. H. Noh, W. S. Yang, Y. C. Kim, S. Ryu, J. Seo and S. I. Seok. Compositional engineering of perovskite materials for high-performance solar cells. Nature. 2015, 517, 476-480.

[43]. H. Zhang, J. Shi, X. Xu, L. Zhu, Y. Luo, D. Li and Q. Meng, Mg-doped TiO 2 boosts the efficiency of planar perovskite solar cells to exceed 19%. J. Mater. Chem. A, 2016, 4, 15383-15389.

[44]. H. Kim, K.-G. Lim and T.-W. Lee. Planar heterojunction organometal halide perovskite solar cells: roles of interfacial layers. Energy & Environmental Science. 2016, 9, 12-30.

[45]. C.-Z. Li, H.-L. Yip and A. K. Y. Jen. Functional fullerenes for organic photovoltaics. Journal of Materials Chemistry. 2012, 22, 4161-4177.

[46]. H.-L. Yip and A. K. Y. Jen. Recent advances in solution-processed interfacial materials for efficient and stable polymer solar cells. Energy & Environmental Science. 2012, 5, 5994-6011.

[47]. C.-C. Chueh, C.-Z. Li and A. K. Y. Jen. Recent progress and perspective in solution-processed Interfacial materials for efficient and stable polymer and organometal perovskite solar cells. Energy & Environmental Science. 2015, 8, 1160-1189.

[48]. C. D. Bailie and M. D. McGehee. High-efficiency tandem perovskite solar cells. Mrs Bulletin. 2015, 40, 681-686.

[49]. T. Liu, K. Chen, Q. Hu, R. Zhu and Q. Gong. Inverted perovskite solar cells: progresses and perspectives. Advanced Energy Materials. 2016, 6.

[50]. L. Meng, J. You, T.-F. Guo and Y. Yang. Recent advances in the inverted planar structure of perovskite solar cells. Accounts of Chemical Research. 2015, 49, 155-165.

[51]. A. Kojima, K. Teshima, Y. Shirai, T. Miyasaka. Organometal halide perovskites as visible-light sensitizers for photovoltaic cells. J. Am. Chem. Soc. 2009,131,6050—6051.

[52]. Grätzel, M, N. G. Park. Organometal halide perovskite photovoltaics: a diamond in the rough. Nano. 2014, 9(5): 1440002.

[53]. J. Burschka, N. Pellet, S.J. Moon, R.H. Baker, P. Gao, M.K. Nazeeruddin, M. Grätzel. Sequential deposition as a route to high-performance perovskite-sensitized solar cells. Nature. 2013, 499, 316.

[54]. J.-H. Im, I.-H. Jang, N. Pellet, M. Grätzel, N.-G. Park, Growth of CH3NH3PbI3 Cuboids with Controlled Size for High-Efficiency Perovskite Solar Cells. Nat. Nanotechnol. 2014, 9, 927.

[55]. M.M. Lee, J. Teuscher, T. Miyasaka, T.N. Murakami, H.J. Snaith. Efficient Hybrid Solar Cells Based on Meso-Superstructured Organometal Halide Perovskites. Science. 2012, 338, 643—647.

[56]. A. Mei, X. Li, L. Liu, Z. Ku, T. Liu, Y. Rong, M. Xu, M. Hu, J. Chen, Y. Yang, M. Grätzel, H. Han. A hole-conductor–free, fully printable mesoscopic perovskite solar cell with high stability. Science. 2014, 345, 295—298.

[57]. S.H. Hwang, J. Roh, J. Lee, J. Ryu, J. Yun, J. Jang. Size-controlled SiO 2 nanoparticles as scaffold layers in thin-film perovskite solar cells. J. Mater. Chem. A. 2014, 2, 16429—16433.

[58]. S. Yang, W. Fu, Z. Zhang, H. Chen, C.Z. Li. Recent advances in perovskite solar cells: efficiency, stability and lead-free perovskite. J. Mater. Chem. A, 2017,5, 11462-11482.

[59]. M. Liu, M. B. Johnston and H. J. Snaith. Efficient planar heterojunction perovskite solar cells by vapour deposition. Nature. 2013, 501, 395-398.

[60]. J. Y. Jeng, Y. F. Chiang, M. H. Lee, S. R. Peng, T. F. Guo, P. Chen and T. C. Wen. CH3NH3PbI3 Perovskite/Fullerene Planar-Heterojunction Hybrid Solar Cells. Advanced Materials. 2013, 25, 3727- 3732.

[61]. D. Luo, W. Yang, Z. Wang, A. Sadhanala, Q. Hu, R. Su, R. Shivanna, G.F. Trindade, J.F. Watts, Z. Xu, T. Liu, K. Chen, F. Ye, P. Wu, L. Zhao, J. Wu, Y. Tu, Y. Zhang, X. Yang, W. Zhang, R.H. Friend, Q. Gong, H.J. Snaith, R. Zhu. Enhanced photovoltage for inverted planar heterojunction perovskite solar cells. Science. 2018, 360 (6396): 1442-1446.

[62]. C. Huo, B. Cai, Z. Yuan, B. Ma, H. Zeng. Two-Dimensional Metal Halide Perovskites: Theory, Synthesis, and Optoelectronics. Small Methods. 2017, 1 (3): 1600018.

[63]. R.L. Milot, R.J. Sutton, G.E. Eperon, A.A. Haghighirad, J.M. Hardigree, L. Miranda, H.J. Snaith, M.B. Johnson, L.M. Herz. Nano Lett.. Charge-Carrier Dynamics in 2D Hybrid Metal–Halide Perovskites. 2016, 16 (11): 7001-7007.

[64]. T. Kataoka, T. Kondo, R. Ito, S. Sasaki, K. Uchida, N. Miura. Magneto-Optical Study on Excitonic Spectra in (C6H13NH3)2PbI4. Phys. Rev. B: Condens. Matter Mater. Phys. 1993, 47, 2010−2018.

[65]. E. A. Muljarov, S. G. Tikhodeev, N. A. Gippius, T Ishihara. Excitons in Self-Organized Semiconductor-Insulator Superlattices – Pb-IBased Perovskite Compounds. Phys. Rev. B: Condens. Matter Mater. Phys. 1995, 51, 14370−14378.

[66]. C.C. Stoumpos, D.H. Cao, D.J. Clark, J. Young, J.M. Rondinelli, J.I. Jang, J.T. Hupp, M.G. Kanatzidis. Ruddlesden–Popper hybrid lead iodide perovskite 2D homologous semiconductors. Chem. Mater. 2016, 28 (8): 2852-2867.

[67]. T. Ishihara, J. Takahashi, T. Goto. Exciton-State in Two- Dimensional Perovskite Semiconductor (C10H21NH3)2PbI4. Solid State Commun. 1989, 69, 933−936.

[68]. Y. Chen, Y. Sun, J. Peng, J. Tang, K. Zheng, Z. Liang. 2D Ruddlesden–Popper perovskites for optoelectronics. Advanced Materials. 2017, 30 (2): 1703487.

[69]. I.C. Smith, E.T. Hoke, D. Solis-Ibarra, M.D. McGehee, H.I. Karunadasa. A layered hybrid perovskite solar-cell absorber with enhanced moisture stability. Angew. Chem.. Int. Ed. 2014, 53, 11232.

[70]. D. Liang, Y. Peng, Y. Fu, M. J. Shearer, J. Zhang, J. Zhai, Y. Zhang, R. J. Hamers, T. L. Andrew, S. Jin. Color-pure violet-light-emitting diodes based on layered lead halide perovskite nanoplates. ACS Nano. 2016, 10, 6897.

[71]. D.H. Cao, C.C. Stoumpos, T. Yokoyama, J.L. Logsdon, T.-B. Song, O.K. Farha, M.R. Wasielewski, J.T. Hupp, M.G. Kanatzidis. Thin Films and Solar Cells Based on Semiconducting Two-Dimensional Ruddlesden–Popper

(CH3(CH2)3NH3)2(CH3NH3)n−1SnnI3n+1 Perovskites. ACS Energy Lett. 2017, 2, 982.

[72]. E.A. Axtell, J.H. Liao, Z. Pikramenou, M.G. Kanatzidis. Dimensional reduction in II-VI materials: A2Cd3Q4 (A = K, Q = S, Se, Te; A = Rb, Q = S, Se), novel ternary low-dimensional cadmium chalcogenides produced by incorporation of A2Q in CdQ. Chem.Eur. J. 1996, 2, 656.

[73]. E.A. Axtell, Y. Park, K. Chondroudis, M.G. Kanatzidis. Incorporation of A2Q into HgQ and Dimensional Reduction to A2Hg3Q4 and A2Hg6Q7 (A = K, Rb, Cs; Q = S, Se). Access of Li Ions in A2Hg6Q7 through Topotactic Ion-Exchange. J. Am. Chem. Soc. 1998, 120, 124.

[74]. J. Androulakis, Peter, S. C.; Li, H.; Malliakas, C. D.; Peters, J. A.; Liu, Z. F.; Wessels, B. W.; Song, J. H.; Jin, H.; Freeman, A. J.; Kanatzidis. Dimensional reduction: a design tool for new radiation detection materials. M. G. Adv. Mater. 2011, 23, 4163.

[75]. S. Yang, W. Fu, Z. Zhang, H. Chen, C.Z. Li. Recent advances in perovskite solar cells: efficiency, stability and lead-free perovskite. J. Mater. Chem. A. 2017, 5, 11462-11482.

[76]. L. Serrano-Lujan, N. Espinosa, T. T. Larsen-Olsen, J. Abad, A. Urbina and F. C. Krebs. Tin-and lead-based perovskite solar cells under scrutiny: an environmental perspective. Adv. Energy Mater., 2015, 5, 1501119.

[77]. A. Babayigit, D. Duy Thanh, A. Ethirajan, J. Manca, M. Muller, H.-G. Boyen and B. Conings. Assessing the toxicity of Pb- and Sn-based perovskite solar cells in model organism Danio rerio. Sci. Rep.. 2016, 6, 18721.

[78]. A. Babayigit, A. Ethirajan, M. Muller and B. Conings. Toxicity of organometal halide perovskite solar cells. Nat. Mater. 2016, 15, 247–251.

[79]. I. Borriello, G. Cantele and D. Ninno. Ab initio investigation of hybrid organic-inorganic perovskites based on tin halides. Phys. Rev. B: Condens. Matter Mater. Phys., 2008, 77, 235214.

[80]. F. Brivio, A. B. Walker and A. Walsh. Structural and electronic properties of hybrid perovskites for high-efficiency thin-film photovoltaics from first-principles.

APL Mater., 2013, 1, 042111.

[81]. D. Cortecchia, H.A. Dewi, J. Yin, A. Bruno, S. Chen, T. Baikie, P.P. Boix, M. Gratzel, S. Mhaisalkar, C. Soci, N. Mathews. Lead-Free MA2CuClxBr4-x hybrid perovskites. Inorg. Chem. 2016, 55: 1044–1052.

[82]. X.P. Cui, K.J. Jiang, J.H. Huang, Q.Q. Zhang, M.J. Su, L.M. Yang, Y.L. Song, X.Q. Zhou. Cupric bromide hybrid perovskite heterojunction solar cells. Synth. Met. 2015, 209: 247–250.

[83]. M. Zhang, M. Liu, P. Chen, M. Hao, J. Yun, L. Wang. Recent advances in low-toxic lead-free metal halide perovskite materials for solar cell application. Asia-Pacific Journal of Chemical Engineering. 2016, 11 (3): 392-398.

[84]. M. Liu, J.H. Yun, P. Chen, M. Hao, L. Wang. Addressing Toxicity of Lead: Progress and Applications of Low-Toxic Metal Halide Perovskites and Their Derivatives. Advanced Energy Materials. 2017, 7 (15): 1602512.

[85]. R.D. Shannon. Revised effective ionic radii and systematic studies of interatomic distances in halides and chalcogenides. Acta Crystallogr A. 1976, 32:751.

[86]. G. A. Fisher, N. C. Norman. The structures of the group 15 element (III) halides and halogenoanions. Adv. Inorg. Chem. 1994, 41, 233.

[87]. A.J. Lehner, D.H. Fabini, H.A. Evans, C.A. He´bert, S.R. Smock, J. Hu, H. Wang, J.W. Zwanziger, M.L. Chabinyc, R. Seshadri. Crystal and Electronic Structures of Complex Bismuth Iodides A3Bi2I9 (A = K, Rb, Cs) Related to Perovskite: Aiding the Rational Design of Photovoltaics. Chem Mater. 2015, 27:7137.

[88]. S.F. Hoefler, G. Trimmel, T. Rath. Progress on lead-free metal halide perovskites for photovoltaic applications: a review. Monatsh Chem. 2017, 148: 795-826.

[89]. K. Eckhardt, V. Bon, J. Getzschmann, J. Grothe, F. M. Wisser, S. Kaskel. Crystallographic insights into (CH 3 NH 3) 3 (Bi 2 I 9): a new lead-free hybrid organic–inorganic material as a potential absorber for photovoltaics. Chem.

Commun. 2016, 52, 3058.

[90]. M. Liu, J.-H. Yun, M. Cai, Y. Jiao, P. V. Bernhardt, M. Zhang, Q. Wang, A. Du, H. Wang, G. Liu, L. Wang. Organic–inorganic bismuth (III)-based material: A lead-free, air-stable and solution-processable light-absorber beyond organolead perovskites. Nano Res. 2016, 9, 692.

[91]. B.-W. Park, B. Philippe, X. Zhang, H. Rensmo, G. Boschloo, E. M. J. Johansson. Bismuth Based Hybrid Perovskites A3Bi2I9 (A: Methylammonium or Cesium) for Solar Cell Application. Adv. Mater. 2015, 27, 6806.

[92]. R.L.Z. Hoye, R.E. Brandt, A. Osherov, V. Stevanovic´, S.D. Stranks, M.W.B. Wilson, H. Kim, A.J. Akey, J.D. Perkins, R.C. Kurchin, J.R. Poindexter, E.N. Wang, M.G. Bawendi, V. Bulovic´, T. Buonassisi. Methylammonium bismuth iodide as a lead-free, stable hybrid organic–inorganic solar absorber. Chem Eur J. 2016, 22:2605.

[93]. X. Zhang, G. Wu, Z. Gu, B. Guo, W. Liu, S. Yang, T. Ye, C. Chen, W. Tu, H. Chen. Active-layer evolution and efficiency improvement of (CH3NH33Bi2I9-based solar cell on TiO2-deposited ITO substrate. Nano Res. 2016, 9(10): 2921-2930.

[94]. Q. Chen, N. De Marco, Y. Yang, T.B. Song, C.C. Chen, H. Zhao, Z. Hong, H. Zhou, Y. Yang. Under the spotlight: The organic–inorganic hybrid halide perovskite for optoelectronic applications. Nano Today. 2015, 10:355.

[95]. Stoumpos C.C., Malliakas C.D., Kanatzidis M.G. Semiconducting Tin and Lead Iodide Perovskites with Organic Cations: Phase Transitions, High Mobilities, and Near-Infrared Photoluminescent Properties. Inorg. Chem. 2013 52:9019.

[96]. D.G. Billing, A. Lemmerer. Inorganic–organic hybrid materials incorporating primary cyclic ammonium cations: The lead iodide series. Crystengcomm. 2007 9:236.

[97]. F. Hao, C. C. Stoumpos, D. H. Cao, R. P. H. Chang and M. G. Kanatzidis. Lead-free solid-state organic–inorganic halide perovskite solar cells. Nat. Photonics, 2014, 8, 489–494.

[98]. N.K. Noel, S.D. Stranks, A. Abate, C. Wehrenfennig, S. Guarnera, A.A.

Haghighirad, A. Sadhanala, G.E. Eperon, S.K. Pathak, M.B. Johnston, A. Petrozza, L.M. Herz, H.J. Snaith. Lead-free organic–inorganic tin halide perovskites for photovoltaic applications. Energy Environ Sci. 2014, 7:3061.

[99]. F. Hao, C. C. Stoumpos, P. Guo, N. Zhou, T. J. Marks, R. P. Chang, M. G. Kanatzidis. Solvent-Mediated Crystallization of CH3NH3SnI3 Films for Heterojunction Depleted Perovskite Solar Cells. J. Am. Chem. Soc. 2015, 137, 11445.

[100]. M. Zhang, M. Liu, J.-H. Yun, M. Noori, X. Zhou, N. A. Cooling, Q. Wang, H. Yu, P. C. Dastoor, L. Wang. Low-temperature processed solar cells with formamidinium tin halide perovskite/fullerene heterojunctions. Nano Res. 2016, 9, 1570.

[101]. F. Zuo, S. T. Williams, P.-W. Liang, C.-C. Chueh, C.-Y. Liao and A. K. Y. Jen. Binary-Metal Perovskites Toward High-Performance Planar-Heterojunction Hybrid Solar Cells. Advanced Materials. 2014, 26, 6454-6460.

[102]. J. Im, C. C. Stoumpos, H. Jin, A. J. Freeman and M. G. Kanatzidis. Antagonism between Spin–Orbit Coupling and Steric Effects Causes Anomalous Band Gap Evolution in the Perovskite Photovoltaic Materials CH3NH3Sn1–x Pb x I3. The Journal of Physical Chemistry Letters. 2015, 6, 3503-3509.

[103]. J. Feng, B. Xiao. Effective Masses and Electronic and Optical Properties of Nontoxic MASnX3 (X = Cl, Br, and I) Perovskite Structures as Solar Cell Absorber: A Theoretical Study Using HSE06. J. Phys. Chem. C. 2014, 118:19655.

[104]. M.C. Jung, S.R. Raga, Y. Qi. Properties and solar cell applications of Pb-free perovskite films formed by vapor deposition. RSC Adv. 2016, 6:2819.

[105]. Y. Yu, D. Zhao, C.R. Grice, W. Meng, C. Wang, W. Liao, A.J. Cimaroli, H. Zhang, K. Zhu, Y Yan. Thermally evaporated methylammonium tin triiodide thin films for lead-free perovskite solar cell fabrication. RSC Adv. 2016, 6:90248.

[106]. T. Yokoyama, D.H. Cao, C.C. Stoumpos, T.B. Song, Y. Sato, S. Aramaki, M.G. Kanatzidis. Overcoming Short-Circuit in Lead-Free CH3NH3SnI3 Perovskite Solar Cells via Kinetically Controlled Gas–Solid Reaction Film Fabrication

Process. J. Phys. Chem. Lett. 2016, 7:776.

[107]. T.M. Koh, T. Krishnamoorthy, N. Yantara, C. Shi, W.L. Leong, P.P. Boix, A.C. Grimsdale, S.G. Mhaisalkar, N. Mathews. Formamidinium tin-based perovskite with low E g for photovoltaic applications. J Mater Chem A. 2015, 3:14996.

[108]. S.J. Lee, S.S. Shin, Y.C. Kim, D. Kim, T.K. Ahn, J.H. Noh, J. Seo, S.I. Seok J. Fabrication of Efficient Formamidinium Tin Iodide Perovskite Solar Cells through SnF2–Pyrazine Complex. Am. Chem. Soc. 2016 138:3974.

[109]. W. Liao D, Zhao., Y. Yu, C.R. Grice, C. Wang, A.J. Cimaroli, P. Schulz, W. Meng, K. Zhu, R.-G. Xiong, Y. Yan. Lead-Free Inverted Planar Formamidinium Tin Triiodide Perovskite Solar Cells Achieving Power Conversion Efficiencies up to 6.22%. Adv Mater 2016, 28:9333.

[110]. P.P. Sun, Q.S. Li, L.N. Yang, Z.S. Li. Theoretical insights into a potential lead-free hybrid perovskite: substituting Pb 2+ with Ge 2+. Nanoscale. 2016, 8:1503.

[111]. X. Lu, Z. Zhao, K. Li, Z. Han, S. Wei, C. Guo, S. Zhou, Z. Wu, W. Guo, C. L. Wu. First-principles insight into the photoelectronic properties of Ge-based perovskites. RSC Advances. 2016, 6(90), 86976–86981.

[112]. C.C. Stoumpos, L. Frazer, D.J. Clark, Y.S. Kim, S.H. Rhim, A.J. Freeman, J.B. Ketterson, J.I. Jang, M.G. Kanatzidis. Hybrid Germanium Iodide Perovskite Semiconductors: Active Lone Pairs, Structural Distortions, Direct and Indirect Energy Gaps, and Strong Nonlinear Optical Properties. J. Am. Chem. Soc. 2015, 137:6804.

[113]. T. Krishnamoorthy, H. Ding, C. Yan, W.L. Leong, T. Baikie, Z. Zhang, M. Sherburne, S. Li, M. Asta, N. Mathews, S.G. Mhaisalkar. Lead-free germanium iodide perovskite materials for photovoltaic applications. J. Mater. Chem. A. 2015, 3:23829.

[114]. P. Cheng, T. Wu, J. Zhang, Y. Li, J. Liu, L. Jiang, X. Mao, R. Lu, W. Deng, K. Han. (C6H5C2H4NH3)2GeI4: A Layered Two-Dimensional Perovskite with Potential for Photovoltaic Applications. J. Phys. Chem. Lett. 2017, 8(18): 4402-4406.

[115]. J. Qian, B. Xu, W. Tian. A comprehensive theoretical study of halide

perovskites ABX3. Org Electron.Org Electron. 2016, 37:61.

[116]. C. Huang, X.C. Yan, G. Cui, Z. S. Liu, Pang, H. Xu. Novel germanium-containing perovskite material and solar cell comprising same. CN Pat. 2014, 7, CN 103943368.

[117]. J.H. Im, H.S. Kim, N.G. Park. Morphology-photovoltaic property correlation in perovskite solar cells: One-step versus two-step deposition of CH3NH3PbI3. APL Materials. 2014, 2: 081510.

[118]. Z. Song, S.C. Watthage, A.B. Phillips, B.L. Tompkins, R.J. Ellingson, M.J. Heben. Impact of processing temperature and composition on the formation of methylammonium lead iodide perovskites. Chem. Mater. 2015, 27 (13): 4612-4619.

[119]. G.E. Eperon, V.M. Burlakov, P. Docampo, A. Goriely, H.J. Snaith. Morphological control for high performance, solution-processed planar heterojunction perovskite solar cells. Adv. Funct. Mater., 2014, 24 (1):151-157.

[120]. Q. Wang, Y. Shao, Q. Dong, Z. Xiao, Y. Yuan, J. Huang. Large fill-factor bilayer iodine perovskite solar cells fabricated by a low-temperature solution-process. Energy Environ. Sci., 2014, 7 (7):2359–2365.

[121]. Q. Chen, N.D. Marco, Y.M. Yang, T.B. Song, C.C. Chen, H.X. Zhao, Z.R. Hong, H.P. Zhou, Y. Yang. Large fill-factor bilayer iodine perovskite solar cells fabricated by a low-temperature solution-process. Nano Today, 2015, 10 (3): 355-396.

[122]. H.S. Jung, N.G. Park. Perovskite solar cells: from materials to devices. Small, 2015, 11 (1): 10-25.

[123]. M.Z. Liu, M.B. Johnston, H.J. Snaith. Efficient planar heterojunction perovskite solar cells by vapour deposition. Nature, 2013, 501: 395-398.

[124]. Q. Chen, H. Zhou, Z. Hong, S. Luo, H.S. Duan, H.H. Wang, Y.S. Liu, G. Li, Y. Yang. Planar heterojunction perovskite solar cells via vapor-assisted solution process. J. Am. Chem. Soc., 2014, 136 (2), pp 622–625.

[125]. J. J. Zhao, P. Wang, Z. H. Liu, L.Y. Wei, Z. Yang, H. R. Chen, X. Q. Fang, X. L. Liua, Y. H. Mai. Controlled reaction for improved CH 3 NH 3 PbI 3 transition

in perovskite solar cells. Dalton Trans. 2015,44, 17841-17849.

[126]. L Hu, J Peng, W Wang, Z Xia, J Yuan, J Lu, X Huang, W Ma, HSong, Y Cheng, J Tang. Sequential Deposition of CH3NH3PbI3 on Planar NiO Film for Efficient Planar Perovskite Solar Cells. ACS Photonics, 2014, 1 (7), pp 547–553.

[127]. D. Shi, V. Adinolfi, R. Comin, M. Yuan, E. Alarousu, A. Buin, Y. Chen, S. Hoogland, A. Rothenberger, K. Katsiev, Y. Losovyj, X. Zhang, P.A. Dowben, O.F. Mohammed, E.H. Sargent, O.M. Bakr. Low trap-state density and long carrier diffusion in organolead trihalide perovskite single crystals. Science, 2015, 347 (6221): 519-522.

[128]. M.I. Saidaminov, A.L. Abdelhady, B. Murali, E. Alarousu, V.M. Burlakov, W. Peng, I. Dursun, L.F. Wang, Y. He, G. Maculan, A. Goriely, T. Wu, O.F. Mohammed, O.M. Bakr. High-quality bulk hybrid perovskite single crystals within minutes by inverse temperature crystallization. Nature Communications, 2015, 6: 7586.

[129]. O. A. Nguepkap, Yamba. Cooling Crystallization, PID and MPC Control. 2008.

[130]. Process Engineering Laboratory II Crystallization. ETHZ.

[131]. Richard Tilley. “Crystals and crystal structures”, Chapter 6 “Diffraction and crystal structures”, John Wiley & Sons Ltd, 2006.

[132]. Stacey Carrier. “Considerations for Diffuse Reflection Spectroscopy”. American Laboratory, 2016

[133]. H.G. Brittain. Spectroscopy of pharmaceutical solids. 2006.

[134]. http://www.cappa.ie/advanced-research/techniques/time-resolved-photoluminescence/

[135]. W.K. Metzger, R.K. Ahrenkiel, P. Dippo, J. Geisz, M.W. Wanlass, S. Kurtz. Time-Resolved Photoluminescence and Photovoltaics. 2004 DOE Solar Energy Technologies Program Review Meeting.

[136]. https://www.picoquant.com/applications/category/materials-science/time-resolved-photoluminescence#description

[137]. P.F. Moulton. Spectroscopic and laser characteristics of Ti: Al2O3. Journal of the Optical Society of America B. 1986, 3 (1): 125–133.

[138]. http://web.vu.lt/ff/m.vengris/images/TR_spectroscopy02.pdf

[139]. A. Nevin, A. Cesaratto, S. Bellei, C. D'Andrea, L. Toniolo, G. Valentini, D. Comelli. Time-resolved photoluminescence spectroscopy and imaging: new approaches to the analysis of cultural heritage and its degradation. Sensors. 2014, 14(4), 6338-6355.

[140]. M. Aresti, M. Saba, F. Quochi, A. Mura, G. Bongiovanni. Ultrafast Optical Spectroscopy Techniques applied to colloidal nanocrystals. Part of the NATO Science for Peace and Security Series B: Physics and Biophysics book series (NAPSB). 2017, 2, 17.

[141]. C.C. Stoumpos, L. Frazer, D.J. Clark, Y.S. Kim, S.H. Rhim, A.J. Freeman, J.B. Ketterson, J.I. Jang, M.G. Kanatzidis. Hybrid Germanium Iodide Perovskite Semiconductors: Active Lone Pairs, Structural Distortions, Direct and Indirect Energy Gaps, and Strong Nonlinear Optical Properties. J. Am. Chem. Soc. 2015, 137-6804.

[142]. D.B. Mitzi. Synthesis, Crystal Structure, and Optical and Thermal Properties of (C4H9NH3)2MI4 (M = Ge, Sn, Pb). Chem. Mater.. 1996, 8 (3), pp 791–800.

[143]. C.C. Stoumpos, D.H. Cao, D.J. Clark, J. Young, M. James M. Rondinelli, I. Joon. Jang, T. Joseph, Hupp, and G. Mercouri, Kanatzidis. Ruddlesden–Popper hybrid lead iodide perovskite 2D homologous semiconductors. Chem. Mater., 2016, 28 (8), pp 2852–2867.

[144]. D.Y.H. Cao, C.C. Stoumpos, O.K. Farha, J.T. Hupp, and M.G. Kanatzidis. 2D Homologous Perovskites as Light-Absorbing Materials for Solar Cell Applications. J. Am. Chem. Soc., 2015, 137 (24), pp 7843–7850.

[145]. I. C. Smith, E. T. Hoke, D. Solis-Ibarra, M. D. McGehee, H. I. A Karunadasa. Layered Hybrid Perovskite Solar-Cell Absorber with Enhanced Moisture Stability. Angew. Chem., Int. Ed. 2014, 53, 11232− 11235.

[146]. J. Calabrese, N. L. Jones, R. L. Harlow, N. Herron, D. L. Thorn, Y. Wang. Preparation and Characterization of Layered Lead Halide Compounds. J. Am. Chem. Soc. 1991, 113, 2328−2330.

[147]. J. M. Longo, P. M. J. Raccah, Solid State Chem. 1973, 6, 526.

[148]. T. Krishnamoorthy, H. Ding, C. Yan, W.L. Leong et. Lead-free germanium iodide perovskite materials for photovoltaic applications. J. Mater. Chem. A, 2015,3, 23829-23832.

[149]. P.F. Cheng, T. Wu, JX. Liu, W.Q. Deng, and K.L. Han. Lead-Free, Two-Dimensional Mixed Germanium and Tin Perovskites. J. Phys. Chem. Lett., 2018, 9 (10), pp 2518–2522.

[150]. P.F. Cheng, T. Wu, J.W. Zhang, Y.J. Li, JX Liu, L. Jiang, X. Mao, R.F. Lu, W.Q. Deng, and K.L. Han. (C6H5C2H4NH3)2GeI4: A Layered Two-Dimensional Perovskite with Potential for Photovoltaic Applications. J. Phys. Chem. Lett., 2017, 8 (18), pp 4402–4406.

[151]. L. Dou, A.B. Wong, Y. Yu, M. Lai, N. Kornienko. Atomically thin two-dimensional organic-inorganic hybrid perovskites. Science. 25 Sep 2015: Vol. 349, Issue 6255, pp. 1518-1521.

[152]. M.D. Smith, A. Jaffe, E.R. Dohner, A.M. Lindengberg, H.I Karunadasa. Structural origins of broadband emission from layered Pb–Br hybrid perovskites. Chem. Sci., 2017, 8, 4497-4504.

[153]. K. Chondroudis, T. J. McCarthy, M. G. Kanatzidis. Chemistry in Molten Alkali Metal Polyselenophosphate Fluxes. Influence of Flux Composition on Dimensionality. Layers and Chains in APbPSe4, A4Pb(PSe4)2 (A = Rb, Cs), and K4Eu(PSe4)2. Inorg. Chem. 1996, 35, 840−844.

[154]. T.J. McCarthy, M.G. Kanatzidis. Synthesis in Molten Alkali Metal Polyselenophosphate Fluxes: A New Family of Transition Metal Selenophosphate Compounds, A2MP2Se26 (A = K, Rb, Cs;M= Mn, Fe) and A2M’2P2Se6 (A = K, Cs;M’ = Cu, Ag). Inorg. Chem. 1995, 34, 1257− 1267.

[155]. J. Tauc. Optical properties and electronic structure of amorphous Ge and Si. Materials Research Bulletin. 1968, 3: 37–46.

[156]. H.R. Liu, A. Raza, A. Aili, J.Y. Lu, A. AlGhaferi & T.J. Zhang. Sunlight-Sensitive Anti-Fouling Nanostructured TiO2 coated Cu Meshes for Ultrafast Oily Water Treatment. Scientific Reports. 2016, 6, 25414.

[157]. E. A. Davis, N. F. Mott. Conduction in non-crystalline systems V. Conductivity,

optical absorption and photoconductivity in amorphous semiconductors. Philosophical Magazine A. 1970, 22 (179): 903–922.

[158]. E.A. Axtell, J.H. Liao, Z. Pikramenou, M. G. Kanatzidis. Dimensional reduction in II-VI materials: A2Cd3Q4 (A = K, Q = S, Se, Te; A = Rb, Q = S, Se), novel ternary low-dimensional cadmium chalcogenides produced by incorporation of A2Q in CdQ. Chem. Eur. J. 1996, 2, 656.

[159]. E. A. Axtell, Y.; Park, K. Chondroudis, M. G. Kanatzidis. Incorporation of A2Q into HgQ and Dimensional Reduction to A2Hg3Q4 and A2Hg6Q7 (A = K, Rb, Cs; Q = S, Se). Access of Li Ions in A2Hg6Q7 through Topotactic Ion-Exchange. J. Am. Chem. Soc. 1998, 120, 124.

[160]. J. Androulakis, S. C. Peter, H. Li, C. D. Malliakas, J. A. Peters, Z. F. Liu, B. W. Wessels, J. H. Song, H. Jin, A. J. Freeman, M. G. Kanatzidis. Dimensional Reduction: A Design Tool for New Radiation Detection Materials. Adv. Mater. 2011, 23, 4163.

[161]. M.C. Jung, S.R. Raga, Y. Qi. Properties and solar cell applications of Pb-free perovskite films formed by vapor deposition. RSC Adv. 2016, 6:2819.

[162]. Y. Yu, D. Zhao, C.R. Grice, W. Meng, C. Wang, W. Liao, A.J. Cimaroli, H. Zhang, K. Zhu, Y. Yan. Thermally evaporated methylammonium tin triiodide thin films for lead-free perovskite solar cell fabrication. RSC Adv. 2016, 6:90248.

[163]. R. Sheng, A.W.Y. Ho-Baillie, S.J. Huang, M. Keevers, XJ Hao, L.C. Jiang, Y.B. Cheng, and M. A. Green. Four-Terminal Tandem Solar Cells Using CH3NH3PbBr3 by Spectrum Splitting. J. Phys. Chem. Lett., 2015, 6 (19), pp 3931–3934.

[164]. R. L. Hoye, R. E. Brandt, A. Osherov, V. Stevanovic, S. D. Stranks, M.W. Wilson, H. Kim, A. J. Akey, J. D. Perkins, R. C. Kurchin, et al. Methylammonium Bismuth Iodide as a Lead-Free, Stable Hybrid Organic-Inorganic Solar Absorber. Chem. - Eur. J. 2016, 22, 2605−2610.

[165]. R. E. Brandt, R. C. Kurchin, R. L. Hoye, J. R. Poindexter, M. W. Wilson, S. Sulekar, F. Lenahan, P. X. Yen, V. Stevanovic, J. C. Nino, et al. Investigation of

Bismuth Triiodide (BiI3) for Photovoltaic Applications. J. Phys. Chem. Lett. 2015, 6, 4297−4302.

[166]. D.B. Mitzi. Synthesis, Crystal Structure, and Optical and Thermal Properties of (C4H9NH3)2MI4 (M = Ge, Sn, Pb). Chem. Mater., 1996, 8 (3), pp 791–800.

[167]. C. C. Stoumpos, L. Frazer, D.J. Clark, Y.S. Kim, S. H. Rhim, A. J. Freeman, J. B. Ketterson, J.I. Jang, and M.G. Kanatzidis. Hybrid Germanium Iodide Perovskite Semiconductors: Active Lone Pairs, Structural Distortions, Direct and Indirect Energy Gaps, and Strong Nonlinear Optical Properties *J. Am. Chem. Soc.*, **2015**, *137* (21), pp 6804–6819

[168]. C.Q. Ma, D. Shen, T.W. Ng, M.F. Lo, C.S. Lee. 2D Perovskites with Short Interlayer Distance for High-Performance Solar Cell Application. Advanced Materials. 2018, 1800710.

[169]. M.Y. Liu, Z.M. Chen, Q. Xue, S.H. Cheung, S.K. So, H.L. Yip, Y. Cao. High performance low-bandgap perovskite solar cells based on a high-quality mixed Sn–Pb perovskite film prepared by vacuum-assisted thermal annealing. Journal of Materials Chemistry A. 2018 Issue 34.

[170]. D. Ju, Y.Y. Dang, Z.L. Zhu, H.B. Liu, C.C. Chueh, X.S. Li, L. Wang, X.B. H, A.K.Y. Jen, X.T. Tao. Tunable Band Gap and Long Carrier Recombination Lifetime of Stable Mixed CH3NH3PbxSn1–xBr3 Single Crystals. Chem. Mater., 2018, 30 (5), pp 1556–1565.

[171]. D.W. Zhao, Y. Yu, C.L. Wang, W.Q. Liao, N. Shrestha, Corey R. Grice, A. J. Cimaroli, L. Guan, R.J. Ellingson, K. Zhu, X.Z Zhao, R.G. Xiong, Y.f. Yan. Low-bandgap mixed tin–lead iodide perovskite absorbers with long carrier lifetimes for all-perovskite tandem solar cells. Nature Energy2, 2017, 17018.